UiT
THE ARCTIC
UNIVERSITY
OF NORWAY

Faculty of Science and Technology
Department of Physics and Technology

Remote Sensing of Coastal Waters

—

Sandra Susann Solheim Nesse

EOM-3901 Master's Thesis in Energy, Climate and Environment, 30 SP

March 2019

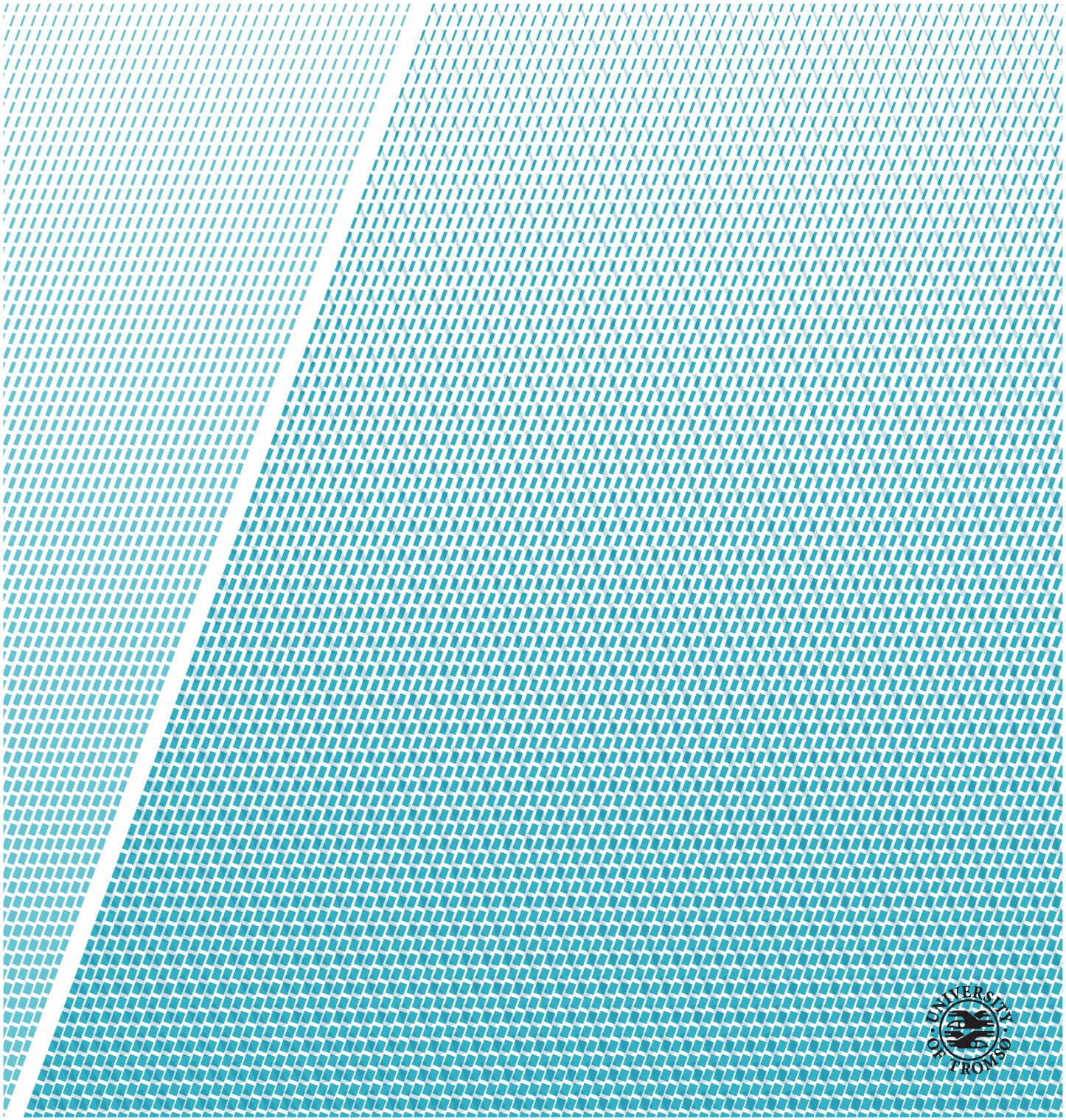

This thesis document was typeset using the *UiT Thesis LaTeX Template*.
© 2019 – http://github.com/egraff/uit-thesis

Acknowledgements

First and foremost, I would like to thank my supervisor, professor Torbjørn Eltoft for the guidance throughout this thesis. I would also like to thank Associate PhD fellow Katalin Blix, PhD fellow Stine Hansen and Engineer Vebjørn Karisari for all the help, and for answering all of my silly questions. Another thank you to Lina Karlsen and Brita Vassmyr for proofreading, critique and comments.

Studying is not just about studies. I would like to thank all the amazing people I have met and come to know during my studies. Thank you for all the fun adventures and for the unforgettable experiences! I would not have been able to study this for five years if it had not been for the great study environment we created. Also, thank you to my office mates for helping me and listening to my stressful mind.

To my family and friends, thank you for all the love and support and for the positive spirits for both ups and downs during these five years. A special thanks to my sister, Daghild, for always listening to me and helping me with nothing and everything.

Last but certainly not least, I would like to thank Morten for all of the support at home, and for bearing with me these past months.

Sandra Susann Solheim Nesse
Tromsø, March 2019

Abstract

The coastal areas outside Lofoten, Vesterålen and Senja, in the northern Norwegian coast, are known for their incredible nature, majestic mountains and unique fishing communities. This coastal area is known for high marine productivity and an important marine environment, being the home for valuable fish stocks including pollock, haddock, herring and cod. To study the characteristics of coastal waters, remote sensing techniques are useful tools. Level 2 ocean color images, containing water quality parameters, and sea surface temperature(SST) images are collected from the optical satellite Sentinel-3, as well as intensity images and geophysical Doppler images from the Synthetic Aperture Radar(SAR) satellite Sentinel-1 are collected. When observing ocean color water quality parameters such as chlorophyll(CHL), total suspended material(TSM) and colored dissolved organic material(CDOM), and SST images, we can observe patterns that appear to be generated by ocean dynamics. The SAR intensity is modified by wind stress and currents variations, and the geophysical Doppler can tell us something about the velocity field in the line of sight direction of the satellite. This study has investigated the relations between ocean color parameters, the SST and the SAR intensity and geophysical Doppler. Using statistical analysis approaches, the results show a clear relation between the various ocean color parameters, a less significant relation between ocean color parameters and SST, but no clear correlation between CHL or SST and the SAR products. The optical and near infrared radiation used to estimate ocean color and SST parameters is dependent on light and nice weather, while the microwave radiation that is used in the SAR products is not. Our investigations do not establish a significantly clear relation between CHL, SST and the SAR products to maintain that SAR images can complement optical sensors in understanding coastal waters during periods with less light and bad weather conditions.

Contents

List of Figures

List of Tables

1 Introduction

This introductory chapter starts with the motivation of the work of the thesis, before it provides a brief overview of the state of the art. Then it presents the topic of research and gives a short summary of the upcoming chapters.

1.1 Motivation and State of the Art

Lofoten, Vesterålen and Senja are areas known for their majestic mountains and unique fishing communities. Every year, thousands of tourists, climbers, surfers, divers, photographers and artists visit the magnificent landscape. These areas are not only incredible beautiful, but more importantly, the home for the worlds last robust cod stock, that stands for thousands of fish meals and billions of income every year. Not to mention the large bird life and the worlds biggest cold water coral reefs. [Naturvernforbundet, nd]

No other places in the world have such an importance for several of our most valuable fish stocks including pollock, haddock, herring and cod. Every year, as much as 70 percent of the fish from the fish catch of the Norwegian Sea and the Barents Sea, pass by Lofoten, Vesterålen and Senja in their most vulnerable

phases of life. [Naturvernforbundet, nd]

An EU project, Ocean Margin Exchange(OMEX)[1] , has reported a strong upwelling along the coast of Northern Norway, explained to be generated by Ekman transport during periods of north east wind, which occurs from May to July. Offshelf transport of surface water, with compensating upwelling of deep nutrient rich water occurs in this time period almost every year.

Compared with other shelf areas in Norway, this area outside Lofoten, Vesterålen and Senja have an enhanced primary production. When the demand for nutrients is high, nutrients are brought up to the surface during a given time window by unique physical properties. These physical properties are wind induced upwelling and a strong vertical mixing and, due to irregular bottom topography combined with ocean currents, a topographically steered upwelling. [Slagstad et al., 1999]

To study the characteristics of the sea, such as coastal dynamics, remote sensing techniques are useful tools. In this thesis project, optical ocean color satellite data and sea surface temperature data will be collected, as well as Synthetic Aperture Radar(SAR) imagery such as intensity images and Doppler products that are derived from SAR data, to study different features of coastal dynamics.

Optical satellites use visible and near infrared electromagnetic radiation for the retrieval of data, while SAR satellites use microwave electromagnetic radiation for the retrieval of data. Different substances on Earth react different to different types of electromagnetic radiation, and therefore the use of both types of satellites may provide more information that can be used when interpreting coastal waters in a study area.

Information from satellite images can be a tool to the gathering of information about the coastal area around Lofoten, Vesterålen and Senja. Gathering information about coastal dynamics can contribute to the broad spectrum of information needed to safeguard these unique areas.

1. The official home page of OMEX `https://www.bodc.ac.uk/omex/`

Satellite observations in the visible spectral bands allow for retrieval of ocean color parameters, such as chlorophyll-*a*(CHL-*a*), total suspended material(TSM) and colored dissolved organic material(CDOM). The concentration of CHL-*a* is considered to be a proxy for primary production in the ocean, and may here be used to identify events of high biologic activity.[Martin, 2014] Phytoplankton blooms can also be spotted from ocean color images. [Blondeau-Patissier et al., 2014].

In coastal waters, we have a variation of the availability of nutrients and sunlight, thus the primary production will vary from area to area. A growth in phytoplankton will therefore take place in upwelling regions where nutrients are brought up to the surface. These upwelling regions can be seen in ocean color images. In the ocean, the water gets colder the deeper you get. So, when you have an upwelling of colder nutrient rich water, one would think that this could be seen in satellite sea surface temperature images. [Martin, 2014]

Satellite observations in the short-wave infrared spectral bands allow for the retrieval of sea surface temperature(SST). Images of CHL-a, CDOM, TSM and SST shows different patterns, which are considered to be associated with ocean dynamics. The combination of these products may hence give a good indication on the local sea surface dynamics.

Sea surface dynamics can be seen in Synthetic Aperture Radar(SAR) images. SAR satellites provide intensity images showing the intensity of the backscattered radiation from the ground. A SAR sensor on a satellite is sensitive to surface roughness, and therefore, from an intensity image, one can get information on wind and waves of a surface. The intensity image of the sea surface will be modified by wind stress, variations in ocean currents and surface slicks. [Henderson, 1998] Another product that can be derived from SAR data, are geophysical Doppler products. This product contains information of the velocity field in the line of sight direction of the satellite.

By studying ocean color images and sea surface temperature images, we can clearly see the same patterns. These patterns are probably related to the coastal dynamics in that area. If we combine ocean color data, sea surface temperature(SST) data and SAR products such as intensity images and geophysical Doppler images, we can investigate the study area and see if we can

find any relations between these different images. Not many studies have tested this topic before. [Lin et al., 2002] found a negative correlation between CHL-a and SAR NRCS(intensity image), using ocean color data from the satellite SeaWiFS(Sea-viewing Wide Field-ofview Scanner) and SAR data from the satellite ERS-2(European Remote Sensing Satellite 2). [Gade and Barale, 2008] have also studied the link between ocean color and SAR data.

In ocean color remote sensing, we observe spectral properties of natural emitted or reflected light from the water body. We can use sunlight that is backscattered from the water colon to retrieve information of the concentration of chlorophyll, color dissolved organic material and other particles in the near surface water. To get this information we use a satellite borne spectrometer to detect and measure the reflected and backscattered sunlight.

When it comes to the physics of it, one assumes to know the spectral properties of the incident sunlight that comes into the water body. Then, the spectral character of sunlight is altered, depending on the absorption and scattering properties of the water body. The properties of the water body will depend on the type and concentration of the different substances. A portion of the altered sunlight is emitted, reflected or scattered back out from the water and detected and measured at the sensor on the satellite. This measured radiation can be made into images displaying spatial distribution of the substances.

If we have the knowledge of how the different substances alter sunlight, for example by wavelength dependent absorption or scattering, then we might be able to gather from the measured radiation what types of substances and their concentration that are in the water body.

Ocean color remote sensing is used for classifying water as for what the water contain. Through satellite images, one wishes to make an image where we can separate water from chlorophyll, color dissolved organic matter(CDOM) and other particles. This can be of interest for researchers that need to know the concentration of for example chlorophyll in an area, water quality or it can be useful in the field of aquaculture and fisheries. If one sees changes in the concentration of chlorophyll, it can be an indication of change in photosynthetic activity. Primary producers in the ocean use photosynthesis for living and

growing [Blondeau-Patissier et al., 2014], and areas with much chlorophyll may also indicate areas that contain a lot of fish.

Ocean currents transports chlorophyll and other particles in the ocean. Using radar imaging systems with intensity images and Doppler products, may hence give us an indication on the motion of particles in the ocean. Additionally, it would be interesting to see if Doppler products have a relation to ocean color parameters. Ocean color remote sensing uses optical imaging systems, and are therefore sensitive to clouds and weather, while radar imaging systems are not. If there exists a relation between these optical properties and radar images, radar imaging can become a useful tool when areas are covered in clouds - which often is the case in northern Norway. [Climatestotravel.com, nd]

1.2 Research Questions

The aim of this study is to investigate which capabilities the combination of remote sensing imaging sensors offer for mapping and monitoring of coastal waters. This project will include using ocean color data and sea surface temperature data from the optical satellite Sentinel-3, and intensity images and Doppler product data from the SAR satellite Sentinel-1.

From the OLCI instrument aboard satellite Sentinel-3 we get images of ocean color parameters such as CHL, CDOM and TSM that can tell us something about the primary production and water quality in the ocean. From the SLSTR instrument aboard Sentinel-3, we get sea surface temperature(SST) data. From the satellite Sentinel-1 we get radar intensity images and derived Doppler products containing information of the velocity field in the line of sight direction of the satellite. These data can be used to retrieve information about wind, currents and velocity of the ocean surface.

Using these different products from visual, thermal and radar satellites we will analyse coastal waters of the study area. Sentinel-3 is an optical satellite and receives visual and near infrared radiation, which means that it is dependent on light and good weather conditions to get data observations. Sentinel-1 on the

other hand, is a Synthetic Aperture Radar(SAR) satellite that uses microwave radiation, which means that it is independent on light and weather conditions to provide data observations. In northern Norwegian coastal waters you typically have clouds that takes over the satellite images. Therefore, you only get optical data when you have light and nice weather conditions.

When observing ocean color parameter images and sea surface temperature images, we can clearly see some of the same patterns in all of the images. By observing these images it appears that the patterns are generated by ocean dynamics. In this thesis project I wish to investigate if the pattern one can see from ocean color and sea surface temperature images, correlates with patterns that can be observed in the intensity and Doppler product images from the SAR satellite.

In particular, this thesis will address 2 main reasearch questions:

1. *Is it possible to find a relationship between ocean color parameters and sea surface temperature images?*

2. *Are there any correlations between the patterns we can observe from ocean color parameters and sea surface temperature from an optical satellite, and intensity images or geophysical Doppler product images from a SAR satellite?*

1.3 Structure of Thesis

Chapter 2 presents coastal dynamics such as ocean currents, ocean gyres, coastal upwelling and ocean fronts.

Chapter 3 introduces remote sensing of coastal waters. It presents ocean color remote sensing and introduces SAR remote sensing.

Chapter 4 introduces the study area for this thesis. It presents the coastal dynamics of the study area.

Chapter 5 addresses information about the satellites and sensors that will be used to collect data for this project.

Chapter 6 addresses the methodology. It presents the data sets used in this thesis, and describes the set up of the data analysis.

Chapter 7 provides and discusses the results of the detection based on the different statistical analysis used for the data sets.

Chapter 8 concludes the work of this thesis and suggests some future work based on findings.

Part I

Theory

2

Coastal Dynamics

Coastal dynamics are important for understanding aspects of the ocean. This chapter presents coastal dynamics such as ocean currents, ocean gyres, coastal upwelling and ocean fronts.

2.1 The Ocean

Earth's surface is covered by approximately seventy percent oceans. The ocean contains most of Earth's water, as well as distinctive amounts of particles and minerals. The ocean has many different roles. It is the home for many marine ecosystems and many species. The coast is an important area for humans and their dependence of the ocean for fishing and trading. The coastal zones of Earth is often in change; some because of human city development and some from the erosion that the ocean has on the landscape. [Martin, 2014]

Different particles and minerals end up in the ocean. Since almost half of Earth's population live within 200 kilometres of the coastal line, a lot of waste from people ends up in the ocean. Harbor areas with in- and outgoing ships will contribute to contamination and waste. Particles and minerals from erosion of

soil, rock and other land materials, also contribute to the amount of particles in the water. As well, wind and rivers bring much sediments and other particles with them in to the ocean. So, the ocean has over millions of years become a complex system containing many different particles and minerals that need to be taken into account when studying it. [Martin, 2014]

The ocean also has a major role when it comes to climate. Both weather patterns and climate change depend upon the ocean. Large ocean currents stand for much of the heat transfer from equator to the poles, and transport heat to northern and southern parts of the globe. The ocean absorbs heat very well, and works therefore as a heat storage. Another role when it comes to climate and climate change, is that the ocean absorbs carbon dioxide and works as a CO_2 storage. [Martin, 2014]

The ability to observe and monitor the oceans of Earth and the atmosphere above it, comes from years and years of developing technology. Earth is changeing, and by observing it from satellites one can watch the physical changes - for example the decrease of ice and snow cover in the arctic and the antarctic. From satellites, one can also predict weather and storms, fisheries management, naval operations and international commerce just to mention some. When it comes to the ocean, we can use satellites both for a local scale or a global scale. [Martin, 2014]

2.1.1 Coastal Dynamics by Definition

The coast is the zone where land meet sea, and they merge together in the so called coastal zone (that reaches from the edge of the continental shelf to the high-tide mark on land). This is an area where terrestrial environmental systems meet and interact with marine environmental systems. [Park, 2017]

Dynamics is said to be a study of motion, or more precise; a study of the relationship between motion and the force that affect that motion. [Park, 2017]

Coastal dynamics will then be the study of coastal motion and all the forces that affect this motion, such as winds, ocean currents, ocean fronts, upwelling,

construction on land etc.

2.2 Introduction to Coastal Dynamics

Earth's coastlines are filled with humans, industries, harbors and terrestrial and marine ecosystems. The coast is a difficult area to study, because of its complexity. Coastal oceans contain many particles like sediments from rivers, human and industrial waste.

The study of coastal dynamics can be important for understanding aspects of the ocean in an area. It can help explain how ecosystems move or why the temperatures in northern Europe are as they are. It might tell us why primary production is better in some areas than others, or it can help us understand the forces that affect ocean motion.

One major characteristics of the ocean, is the continuous motion of water. Both vertical and horizontal movements in the water forms the ocean circulation system. There are many factors contributing to a transitional motion of ocean water. There are winds, tides, evaporation, deposition from land, coastal drainage and atmosphere pressure just to mention some. In addition, because of Earth's rotation, we have the Coriolis force that bends masses of water to the right on the northern hemisphere, and to the left on the southern hemisphere.

2.3 Ocean Gyres

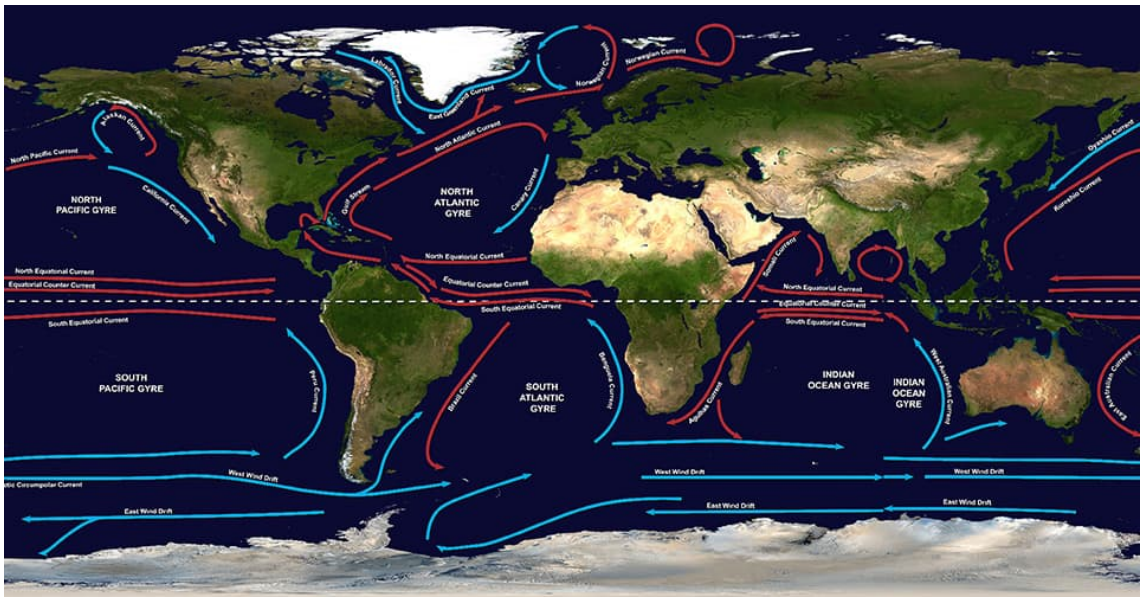

Figure 2.1: Earth's ocean gyres. (From [NOAA, nd a])

Ocean gyres are huge systems of rotating ocean currents. World wide there are many different ocean currents, and five major ocean gyres. From Figure 2.1 we can see the five major gyres; the North- and the South Pacific Gyres, the North- and the South Atlantic Gyres, and the Indian Ocean Gyre. If we look at the Arctic area in Figure 2.1, we can see a warm incoming flow of Atlantic water towards Scandinavia. This flow brings nutrients from the North Atlantic gyre to the Arctic. This warm flow also triggers melt of snow and ice as it brings a warmer climate with it, which again leads to an increase of nutrients to phytoplankton growth in the ocean. [Scott and Hansen, 2016, Randelhoff and Sundfjord, 2018]

2.3.1 Boundary Currents

Ocean currents that have dynamics that are determined by a coastline, are said to be boundary currents. The five major gyres mentioned above are all flanked by a strong and narrow Western Boundary Current, and a weak and broad Eastern Boundary Current. The westerly boundary currents are formed on the west

side of ocean basins, carrying warm tropical water towards the poles. The easterly boundary currents are formed on the eastern side of the ocean basins and carry cold water from higher to lower latitudes. The Gulf Stream is an example of a Western Boundary Current, while the Humbolt Current is an example of an Eastern Boundary Current. [Warren, 1976, Imawaki et al., 2013]

Thousands of years ago, humans thought of the ocean as this blue unlimited world filled with different species and organisms. After years and years of exploring the ocean, men gathered knowledge and information and started to become aware of the fact that not all of the ocean areas were the same. Some ocean areas contained productive marine life, while other areas almost did not contain that much marine life. Humans found the west coast of the continents to have the most productive marine life. These areas are known to be part of the eastern boundary currents, and are said to account for approximately 1 % of Earth's oceans, and at the same time stand for approximately 20 % of the worldwide fish catch. [Kämpf and Chapman, 2016]

Areas with the main eastern boundary systems can be seen in Figure 2.2.

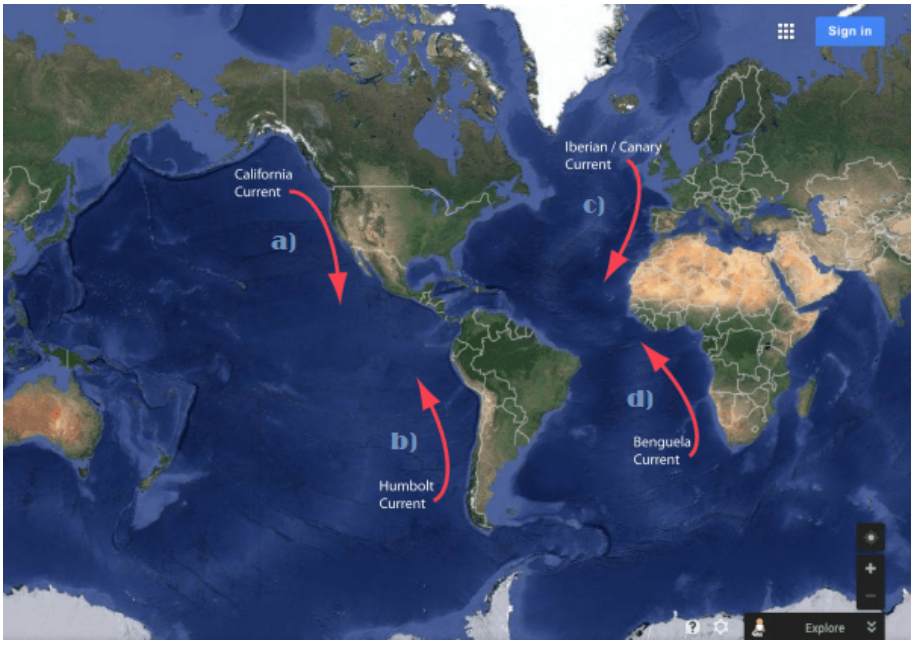

Figure 2.2: The four main eastern boundary currents. a) California/Oregon/Washington in the North Pacific. b)Peru and Chile in the South Pacific. c) Northwest Africa and Portugal in the North-Atlantic. d) South Africa and Nambia in the South Atlantic. (From [Caccioppoli, 2014])

Nutrient rich water are often brought into eastern boundary currents by coastal upwelling. These upwelling systems export phytoplankton-fixed carbon into the ocean via Ekman transport and mesoscale filaments and Eddies. This happens over complex coastal topography when eastern boundary currents flows past these areas. The four major upwelling systems we can see in Figure 2.2 are known to provide a great environment and habitat for fish, sea birds and mammals in and close to the ocean. [Kämpf and Chapman, 2016, Lovecchio et al., 2018]

2.4 Upwelling

Upwelling is a natural phenomenon that contains from deep water a vertical component toward the surface. As we can see from Figure 2.3, upwelling occurs when deep, cool and nutrient-rich water comes up to the surface to balance

the loss of surface water close to the coast. This upwelling fills surface waters with plant nutrients. [Bakun, 1990]

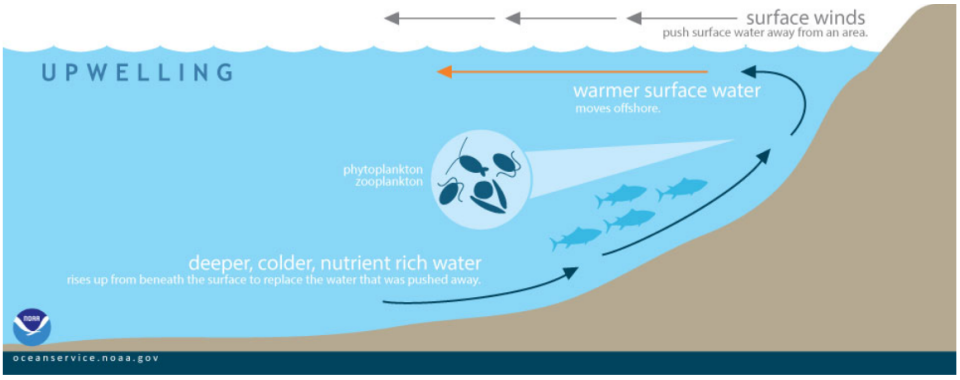

Figure 2.3: The process of upwelling.(From [NOAA, nd b])

In some specific areas upwelling occurs more than in other areas. These areas contain an overflood of marine life, and most of Earth's fisheries happens here. Phytoplankton grows where we have nutrients, and therefore it grows with this upwelling of nurtient-rich water. Microscopic animals, zooplankton, eats phytoplankton, and the zooplankton will be eaten by fish. Therefore, we can see that it tends to be a lot of fish near upwelling areas. [Bakun, 1990, Matthews, 2014]

Throughout the worldwide ocean it exist a great quantity of other upwelling systems. Some of these systems only occur on a seasonal basis, while others occur year round. Upwelling systems are important processes for coastal oceans. They are important for worldwide productivity, biochemical cycles and food-web dynamics. [Kämpf and Chapman, 2016]

In the top 50 to 100 meters of the ocean, the *euphotic zone*, we find phytoplankton and phototropic bacteria. These organisms produce organic carbon from inorganic carbon. Because of this carbon fixation, marine organisms can grow, live and reproduce. Photosynthesis happens through phytoplankton and phototropic bacteria, and almost all marine ecosystems depend on carbon fixation. The rate of carbon fixation depend on the amount of nutrients in the euphotic zone in different ways. To mention some, we have upwelling which brings up

high-nurtient cold water from deeper waters up with a current. We also have vertical mixing in the ocean and run-off water, from groundwater or rivers, from the continent that contain nutrients. [Kämpf and Chapman, 2016]

When marine life forms in Earth's oceans, there are some factors that are fundamental; sunlight, nutrients and oxygen. These fundamentals are important for the understanding between physical and biological interactions in these upwelling areas. [Kämpf and Chapman, 2016]

2.4.1 Ocean Life

The action of water, ice, wind and waves have for millions of years eroded the Earth. The elements from this erosion have in different ways ended up in the ocean. Now the ocean seems to be a huge bowl with a mixture of all of Earth's elements, and have a big variety of marine life. The food webs for these species are complex systems based on the conversion from inorganic to organic matter. [Kämpf and Chapman, 2016]

To study upwelling areas, there are many factors to take into consideration. Here is a simplified figure of processes that influence the marine life.

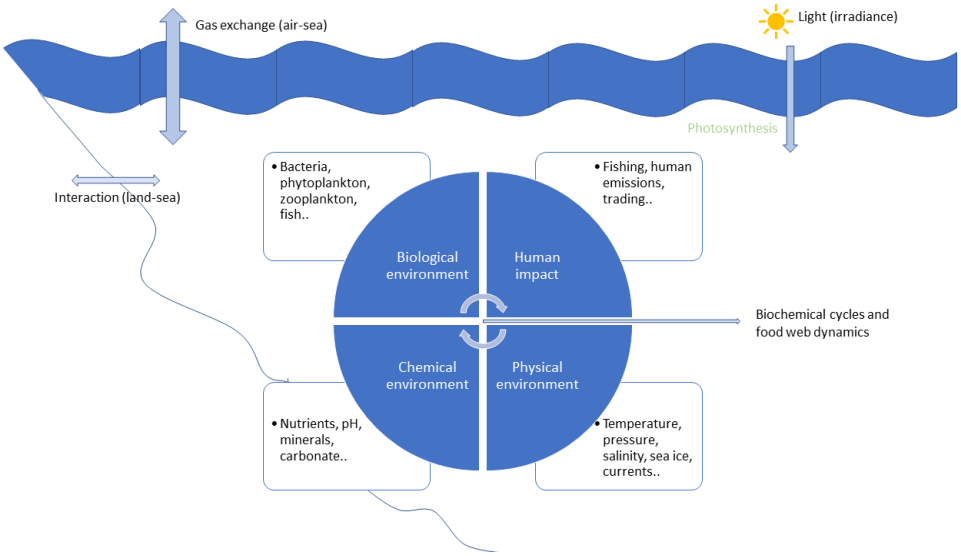

Figure 2.4: Processes influencing marine life.

2.4.2 The Physics of Coastal Upwelling

There are different types of coastal upwelling mechanisms. The classical one is wind-driven, and are the mechanism that rule for the largest upwelling areas on Earth. When it comes to the physics of it, we can describe it as an upward movement of water. The water parcels in the water column have a movement up towards the surface. This upward movement has to happen over a long enough period of time, from a few days to a couple of weeks, and rise the water parcels over a vertical distance of hundred meters or more. There are three main forms of wind-driven coastal upwelling (see Figure 2.5): [Kämpf and Chapman, 2016]

- Coastal upwelling
- Equatorial upwelling
- Ice-edge upwelling

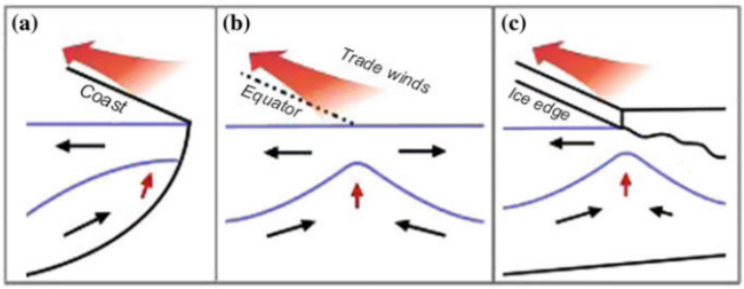

Figure 2.5: Three types of wind-driven oceanic upwelling. (a) Coastal upwelling (southern hemisphere), (b) Equatorial upwelling, and (c) Ice-edge upwelling. Relative to the coast, the eqator or the ice-edge, the red arrow shows the prevailing wind direction. (From [Kämpf and Chapman, 2016])

When it comes to the dynamics of wind-driven upwelling, there are some forces that play a dominant role - such as the rotation of Earth and related effects as the force of Coriolis. [Kämpf and Chapman, 2016]

As we can see from Figure 2.5, the three wind-driven upwelling systems act differently. Coastal upwelling, (a) in Figure 2.5 rely on two things to exist. That

is the presence of relative shallow water and a solid coast boundary that works impermeable. Equatorial upwelling, (b) in Figure 2.5 is linked with the Coriolis force, where the sign of the Coriolis parameter, which is the proportionality constant in the Coriolis force, changes over the equator. The Coriolis force represents the deflection pattern for objects that are not linked to the ground as they move large distances over and around Earth. This force deb off around the equator, but takes a full swing around >50 km from the equator. Because of these rotational effects and their spatial variation, the upwelling process for the equator is similar to that for coasts. [Kämpf and Chapman, 2016]

Ice-edge upwelling, (c) in Figure 2.5, is created slight different. The currents under the sea ice will feel a substantial dampening of the effect of wind stresses, and this will create the ice edge upwelling. [Kämpf and Chapman, 2016]

Coastal upwelling can be in a major coastal upwelling system as a quasi-permanent feature, or it can be in a seasonal coastal upwelling system as as a seasonal feature, all depending on how the typical wind condition is in that area. [Kämpf and Chapman, 2016]

Since coastlines and seafloors are often inconstant, and upwelling can occur along a straight coastline, we can get generally localized wind-driven coastal upwelling systems. The upwelling is not constant, and as a consequence some areas will have more upwelling in some regions. These regions are called upwelling centres, and have more pronounced upwelling. With these centres one associates strong frontal flows linked with upwelling jets that breaks up into Eddies. Eddies are patterns of mesoscale circular circulation (for coastal waters 10-20 km) - easily described as rotation of water mass. Close to these upwelling centres most of the primary productivity takes place. [Kämpf and Chapman, 2016, Joseph, 2014]

2.4.3 The Upwelling Process

We say that seawater is incompressible. Thus, upwelling induces a vertical volume flux. This can only happen if a divergence of a horizontal flow move laterally away the same amount of water per time. A result from this is

wind-induced offshore movement of ocean surface water that triggers upwelling of cold water from below to replace the surface water that moved away. [Kämpf and Chapman, 2016]

When it comes to equatorial upwelling, the trade winds will induce a movement of surface water away from the equator on both the northern and the southern hemisphere. This will result in a replacement by water below the surface. Generally, the lower water below the surface tends to be denser than the surface water. The potential energy of the system will be increased due to this density difference. Therefore, the system requires an external energy source, here being provided by wind stress from the surface. [Kämpf and Chapman, 2016]

Rotational effects, such as the Coriolis force, will control all dynamical processes on the ocean that lasts longer than a day. The dynamics of horizontal ocean currents in the oceans interior (somewhere between the seafloor and the sea surface) is goverened by the *geostrophic balance*. The geostrophic balance is known as a balance between two forces; the Coriolis force and the horizontal pressure gradient force. This balance indicates that the horizontal currents follows lines of constant pressure(isobars). Throughout the water column, there are horizontal geostrophic flows because of the surface pressure anomalies. If this flow is weakened by an adaptation of density interface, it is called baroclinic compensation. Frictional effects as well as geostrophic flows becomes relevant near lateral and vertical boundaries. Near these vertical boundaries we get bands called *Ekman layers*. Ekman layers are made when the balance between the friction and the Coriolis force creates a retreat of the geostrophic balance flow.[Kämpf and Chapman, 2016]

The general dynamic structure of coastal upwelling can be seen in Figure 2.6

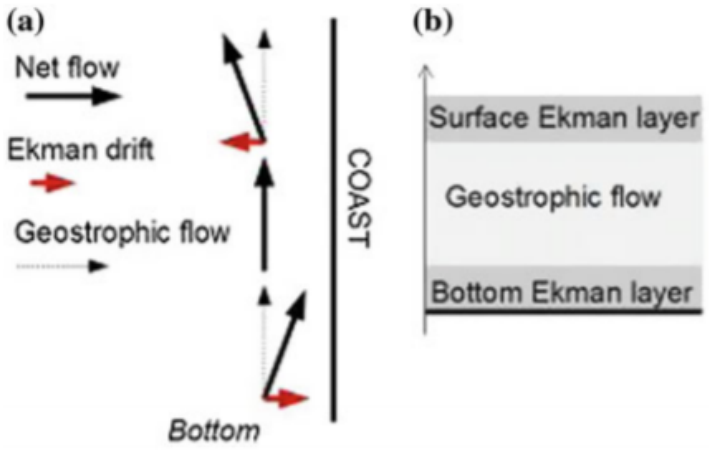

Figure 2.6: The general dynamic structure of coastal upwelling. (a) shows the flow structure in the water column, with the sea surface being in the top of the figure. (b) shows the vertical structure of the ocean dynamics. (From [Kämpf and Chapman, 2016])

In these upwelling systems there exist a geostrophic current that is parallell to the coast. This current is also called an upwelling jet, and is detected, as we can see from Figure 2.6, towards the shore in a bottom Ekman layer and away from the shore in a near surface Ekman layer. [Kämpf and Chapman, 2016]

An offshore movement in the surface Ekman layer induced by a component of wind stress that is parallel to the coast. This component lowers the sea level with approximately 5-10 cm before the lowering reasches a dynamic equlibrium. This sea level drop is important for the creation of a force with a pressure gradient towards the shore that drives the geostrophic upwelling jet into a speed of around 10 to 50 cm per second. Hence, a flow towards the shore is created in the lower Ekman layer near the bottom (with a thickness in between 5 to 25 meters), due to the fact that the frictional effects from the seafloor have an impact on the geostrophic flow. The flow towards the shore from near the bottom is the impetus that moves the lower water near the bottom towards the shore as it reaches the coast in the euphotic zone. [Kämpf and Chapman, 2016]

2.4.4 Ekman Drift and Wind Stress

From this formula

$$\tau = \rho_{air} C_D W, \tag{2.1}$$

we can calculate the magnitude of the frictional wind stress at the sea surface, τ. Here W is the wind speed (horizontally), approximately $W = 10m$ above the sea surface(a reference height), C_D is the coefficient of the wind drag with a value that depend on on the level of turbulence in the lower part of the atmosphere (set to be approximately $C_D = 0.001 - 0.002$). At last we have ρ_{air}, which is the air density and sat to be $\rho_{air} = 1.28kg/m^3$. The frictional wind stress, ρ, has the same vector direction as the horizontal wind speed. [Kämpf and Chapman, 2016]

The response of the ocean surface from wind stress is not quite uncomplicated. Currents in an Ekman layer moves in an Ekman spiral, see Figure 2.7, with the depth of the ocean when no other processes occurs. [Kämpf and Chapman, 2016]

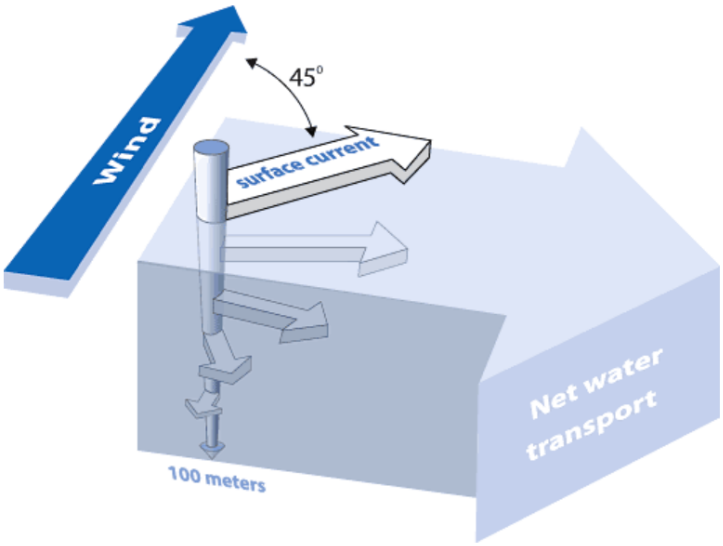

Figure 2.7: An Ekman sprial. (From [NOAA, 2017])

The Coriolis force changes direction at the equator. In a surface Ekman layer the horizontal volume transport, Ekman drift or Ekman transport, has a 90°angle to

wind stress. This is due to the fact of the change in Coriolis force at the equator. On the northern hemisphere, the Ekman drift turns right, while on the southern hemisphere, it turns left. See Figure 2.8. [Kämpf and Chapman, 2016]

(a) The northern hemisphere. **(b)** The southern hemisphere.

Figure 2.8: The relationship between Ekman drift and wind stress.

The magnitude of the Ekman drift, M, can be calculated with formula

$$M = \frac{\tau}{\rho_{sea}}|f|, \tag{2.2}$$

where τ is the magnitude of wind stress given with formula 2.1, ρ_{sea} is the sea density given at $\rho_{sea} = 1026kg/m^3$, and f being the Coriolos parameter which can be calculated by formula

$$f = \frac{4\pi}{T_{Earth}} sin(\phi), \tag{2.3}$$

where T_{Earth} is Earth's rotation period sat to be $T_{Earth} = 86400$ seconds, and ϕ is the latitude. Therefore, one only needs the geographical position and the wind stress to calculate the Ekman drift. [Kämpf and Chapman, 2016]

2.4.5 Upwelling Jets

It is typical for upwelling jets to become unstable. When they reach far up towards the surface they can often break up into mesoscale Eddies creating a turbulent field in the ocean. An upwelling zone can vary in width, some areas can have small upwelling zones and others can be up to several hundred kilometres wide. [Kämpf and Chapman, 2016]

The wind-driven circulation on Earth is important for transport around the globe. Coastal upwelling jets plays a major role for this wind-driven circulation. Especially when it comes to transporting heat and fresh water, and it helps to intensify flows from subtropical gyres towards the equator. Hence, along the coast, upwelling jets transport organic material and nutrients with the water, and they implies the establishment of divergent biological zones. These zones will have a difference in production, since phytoplankton, zooplankton, fish, etc. have different time scales linked to their creation. It takes for example 5 days for phytoplankton to be produced, 25 days for zooplankton and as much as up to a couple of months or more for small fish grow.[Kämpf and Chapman, 2016]

Upwelling jets are not very smooth flows. As mentioned earlier in the text, coastal upwelling jets tends to shed mesoscale Eddies, especially after days or weeks. Mesoscale Eddies can vary in diameter size depending on the location. Open ocean Eddies are much larger (300 km) than coastal Eddies (10-20 km). Because of the shed of Eddies, upwelling zones can increase in width along the coast for the same direction as the jets. [Kämpf and Chapman, 2016]

Filaments

Filaments are specific pathways with Eddy fields, where upwelled nutrient and organic rich matter water get transported offshore. These filaments can be seen in satellite images. [Kämpf and Chapman, 2016]

2.4.6 Other Types of Coastal Upwelling Mechanisms

So far I have only mentioned wind-driven coastal upwelling systems, which are most known, but there also exist other upwelling mechanisms. In fact, depending on how your study area is constructed, the upwelling can be different. Topography, continental shelf, tide and wind will all affect the upwelling in that area. Therefore we can have slightly different upwellings like Shelf-Break Upwelling, Tidally-Induced Upwelling or Upwelling Caused by Topography, while the result is the same; underlaying more nutrition rich water are brought up towards the surface. [Kämpf and Chapman, 2016]

2.5 Ocean Fronts

According to [Park, 2017], a oceanic front is "*a boundary that separates masses of water within the ocean that have different temperatures and densities*". Easily explained, an ocean front is a boundary separating two different masses of water. This can be seen in satellite images using microwave remote sensing.

3

Remote Sensing of Coastal Waters

Remote sensing of coastal waters include the use of several different satellite instruments. As mentioned in the introductory chapter, we can get different information about the coast from different types of remote sensing. From ocean color remote sensing, we can get information about different parameters in the ocean, such as the concentration of chlorophyll, total suspended matter or color dissolved organic material. From thermal remote sensing, we can get sea surface temperature. And from Synthetic Aperture Radar(SAR) remote sensing we can get information about the ocean dynamics.

3.1 Remote Sensing

Remote sensing involves using electromagnetic radiation to obtain information. This can be done from a sensor on a satellite or an aircraft for example. When it comes to remote sensing, one often seek information about land, the ocean

and/or the atmosphere. While obtaining the information, one is not in physical contact with the investigating object or phenomenon. [Martin, 2014]

So, using remote sensing can give us information about many important an interesting factors to help us understand and measure different aspects of the Earth.

3.1.1 Electromagnetic Waves

The electromagnetic spectrum is important for remote sensing. Remote sensing uses electromagnetic radiation to obtain information from the surface, the atmosphere and the ocean. One can use different wavelengths of the electromagnetic spectrum for different purposes. The optical spectrum, the infra-red spectrum and microwave spectrum are mostly used. This is because the atmosphere in the other parts of the electromagnetic spectrum often absorb all the energy, and are therefore unpracticle to use for remote sensing. [Elachi and Van Zyl, 2006]

When the electromagnetic radiation interacts with an object, the energy reflected, emitted or scattered back from that object will depend on the wavelength of the radiation and the physical properties of the object. Thereafter, when the radiation is on its way to the sensor, it will carry the information from when it interacted with the object, and propagate through the atmosphere all the way to the sensor. To extract the information from this radiation, you can use a collector and a detector to investigate the information. [Elachi and Van Zyl, 2006]

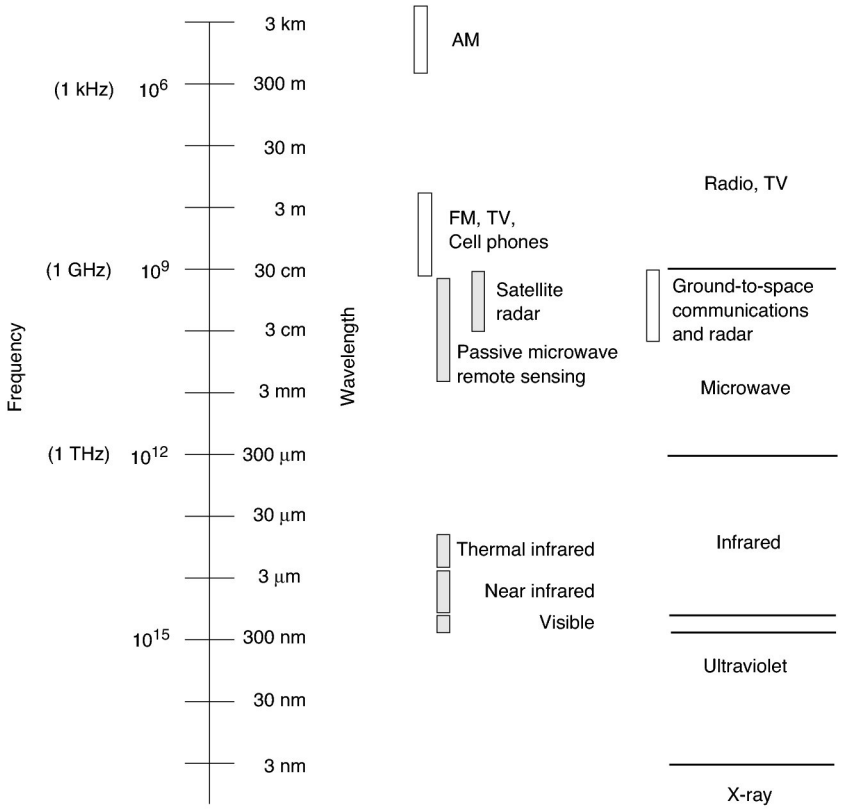

Figure 3.1: The electromagnetic spectrum by frequency and wavelength. (From [Martin, 2014])

The electromagnetic spectrum is divided into many regions as we can see from the Figure 3.1. We can see the five gray bands of the spectrum that are used for satellite remote sensing: visible, near infra-red, thermal infra-red, passive microwave remote sensing and satellite radar. [Martin, 2014]

3.1.2 Ocean Remote Sensing

The first ocean remote sensing satellite was launched by the USA in 1970. After that many other countries have also launched satellites with oceanographic instrumentation on board. From a satellite with instrumentation like this combined with in-situ information from for example boats, we can get several interesting variables related to ocean color remote sensing. Just to mention some different variables; sea surface temperature(SST), directional

distribution and height of ocean swell, the direction and speed of wind, water content and rain rate in the atmosphere, concentration of phytoplankton, sediments, suspended and dissolved materials, and types and areal extent of polar sea ice. These variables can help us to study and understand the ocean. [Martin, 2014]

Before we got the opportunity to study the ocean from space, we only had the possibility to study it on Earth. Then, the only way to get the information was from expensive expeditions on ships, air craft surveys or ice islands. These methods were slow and time consuming, and one could only get a small overview of the ocean. When using satellite imagers, the desired variables can be observed on a scale all from 1 km to 1000 km. The same observation would have needed several ships and a lot more time. However, not all variables can be observed by satellites. Some need to be measured by ships or buoys placed in the ocean. To get information deeper down in the ocean, one can for example use instruments as an Argos float. An Argos float is a device that measures the interior of the ocean over a time period before it reaches the surface and sends its information to a satellite. When using all these methods, we get a good picture of the important variables used for ocean color remote sensing. [Martin, 2014]

3.2 Ocean Color Remote Sensing

Ocean color remote sensing is developed to retrieve information of different particles in the top layer of the ocean. This following section introduces ocean color remote sensing and describes how we can use this method to classify the water for what it contain.

3.2.1 Introduction

In ocean color remote sensing, we observe natural emitted light or reflected light by the water body. We can use sunlight that is backscattered from the water colon to retrieve information of the concentration of chlorophyll, color dissolved organic material (CDOM) and other particles in the near surface

water. To get this information we use a satellite to detect and measure the reflected and backscattered sunlight.

When it comes to the physics of it, one assume to know the spectral properties of the incident sunlight that comes into the water body. Then, the spectral character of sunlight is altered, depending on the absorption and scattering properties of the water body. The properties of the water body will depend on the type and concentration of the different substances in the water body. A portion of the altered sunlight is emitted, reflected or scattered back out from the water and detected and measured at the sensor on the satellite. This measured information can be made into a set of data or an image that can be used for further analysis.

If we have the knowledge of how the different substances alter sunlight, for example by wavelength dependent absorption or scattering, then we might be able to gather from the measured radiation what types of substances and their concentration that are in the water body.

Ocean color remote sensing are used for classifying water as for what the water contain. Through satellite images, one wishes to make an image where we can separate water from chlorophyll, color dissolved organic matter(CDOM), total suspended material(TSM) and other particles. This can be of interest for researchers that need to know the concentration of for example chlorophyll in an area, it can be useful in the field of aquaculture and fisheries, and to measure water quality. If one sees changes in the concentration of chlorophyll, it can be an indication of change in photosynthetic activity. Primary producers in the ocean uses photosynthesis for living and growing, and areas with much chlorophyll may also indicate areas that contain a lot of fish.

Ocean color remote sensing can also be used for the detection, mapping and monitoring of phytoplankton blooms, where algal blooms can be an indication of the health of marine ecosystems. It is important to map the amount of chlorophyll in the ocean for applications mentioned above.

3.2.2 Phytoplankton

Most of the plants in the ocean are called phytoplankton or algae, and they have a huge global distribution. They can range from less than $1\mu m$ to more that $100\mu m$. Phytoplankton uses photosynthesis just as other plants, to convert light energy into chemical energy with help from the pigment chlorophyll. The process of photosynthesis in the ocean have been going on for many millions of years. [Wright et al., 2005, Callot, 1991]

One recognizes phytoplankton as a basis for animal production at sea. This animal production supports the food web for fish, and are the base for fisheries. It is therefore important to monitor the population of phytoplankton, since this can have an effect on the fisheries through the timing and abundance of algal blooms. [Lasker, 1981]

The marine food webs dominant source of organic material can be found in the upper layer of the ocean where the sun reaches. Here will the production of phytoplankton associated with photosynthesis take place. Around half of the total primary production on land and at sea comes from phytoplankton. Primary production is measured by the change of biomass. In phytoplankton the photosynthesis is used for making organic forms of carbon from inorganic carbon. Phytoplankton actually transform 10^{11} kg, one hundred million tonnes, carbon dioxide into organic material. One can clearly say that phytoplankton plays an important role in the global carbon cycle, converting CO_2 to organic carbon. [Siegel et al., 2012, Martin, 2014]

Through the process of the oceanic biological pump, the phytoplankton dies, sinks and brings carbon to the deep ocean. So, one can say that phytoplankton helps taking down a part of the atmospheric carbon to the deep oceans. The carbon cycle is out of balance due to fossil fuel consumption with more CO_2 transferred into the atmosphere and the ocean. Because of this unbalance, it is important to measure and monitor the amount and distribution of chlorophyll and primary production. [Martin, 2014]

Ocean color remote sensing depend on the photosynthesis. The photosynthetic pigment within each phytoplankton cell is important for ocean color remote

sensing. This pigment consist of chlorophyll *a*, *b* and *c*. Where *a* is the ubiquitous one, and *b* and *c* are the accessory pigments. When we study ocean color remote sensing, we are interested in chlorophyll *a*, because it is the pigment that appears in all phytoplankton and therefore it can tell us how much phytoplankton we have in the ocean. [Martin, 2014, Wright et al., 2005]

The global distribution of phytoplankton are different from various areas on the globe. Here is an image showing the distibution of chlorophyll.

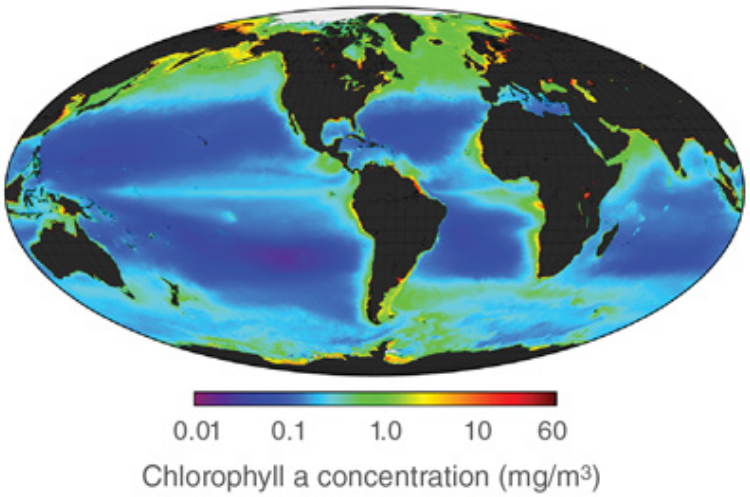

Figure 3.2: The global distribution of chlorophyll *a*. Dark red indicates the most, purple indicates the least and green indicates the moderate regions. Data are from the Sea-Viewing Wide Field-of-View Sensor (SeaWiFS) (Courtesy SeaWiFS Project). (From [Naranjo, nd])

As we can see from Figure 3.2, the regions that contains great concentrations of chlorophyll *a* are located north of 45° in coastal areas and on continental shelves. These regions contain strong nutrient supply. We can see moderate chlorophyll regions around equator and in the subtropical convergence zone south of 45° south. The equator region contains an upwelling of deep nutrient cool water that mix with the warm equatorial waters. And the areas south of 45° contain cool nutrient rich water mixing with warm nutrient poor water from the subtropical waters. [Cullen, 1982, Blondeau-Patissier et al., 2014, Huisman et al., 2006]

3.2.3 Ocean Color

The presence of phytoplankton, suspended material and dissolved material affect the scattering, absorption and reflectance of the ocean. The color of the ocean will be affected by the size and distribution of particles, and the properties and consentration of dissolved matter. This dissolved organic material is also called chromophoric dissolved organic matter (CDOM). CDOM is also called gelbstoff, which is yellow substance and dissolved organic matter that is colored. [Martin, 2014, Zaneveld et al., 2006, McClain, 2009]

There are both oceanic CDOM and terrestrial CDOM. Terrestrial CDOM is produced from land-based runoff that contains dissolved humic acid and fulvic acid. While oceanic CDOM is produced from the degradation of phytoplankton through photolysis. Where photolysis is the chemical process where molecules breaks down into smaller pieces, from absorption of light. The particles split up in organic and inorganic materials. The organic material, also called detritus, are made up of cell fragments from zoo- and phytoplankton. While the inorganic materials are made up of dust and sand from erosion of soil, rock and other land materials. The inorganic material flows into the ocean with rivers, or it blows into the ocean with wind. [Carder et al., 1999, Martin, 2014, Callao and Larrechi, 2015, Mobley, 1994]

The optical properties of sea water is different when it comes to open ocean water and coastal waters. Morel and Prieur(1977) split the ocean into two cases; case 1 waters and case 2 waters. For case 1 waters we have that the optical properties of sea water are dominated by phytoplankton, where the concentration of chlorophyll a is C_a $[mgm^{-3}]$. Open ocean waters are mostly case 1 waters. For case 2 waters, the optical properties of sea water are dominated by suspended material, organic particles and CDOM. This is typical for coastal areas with river runoffs, high human activities like shipping, recreation and fisheries. On Earth, we therefore have mostly case 1 waters. [Morel and Prieur, 1977, Martin, 2014]

3.2.4 Absorption

The total absorption properties can be described by

$$a_T(\lambda) = a_W(\lambda) + a_{ph}(\lambda) + a_{CDOM}(\lambda) \tag{3.1}$$

where a_T is the total absorption, a_W is the absorption value from clear water, a_{ph} is the absorption value from phytoplankton and a_{CDOM} is the absorption value from CDOM and inorganic particles. [Martin, 2014]

The absorption is different from phytoplankton, CDOM and inorganic particles.

CDOM and particles

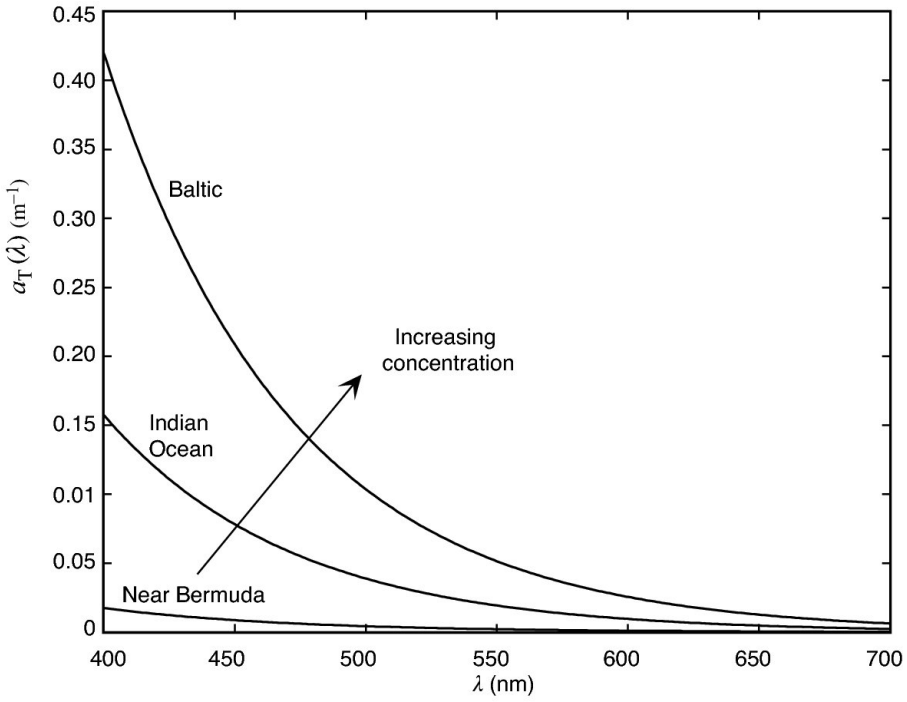

Figure 3.3: The wavelength dependence of the total absorption from three locations, where Indian Ocean and Near Bermuda are oceanic waters, and Baltic Sea is coastal and estuarine water. (The figure is from[Martin, 2014] with data from [Mobley, 1995]

As we can see from Figure 3.3, coastal and estuarine waters contain more CDOM and particles than Oceanic waters. Clearly from Figure 3.3 above, the more CDOM and particles in the water, the more absorption we have in the blue wavelengths. The upper curve for coastal and estuarine waters decreases exponentially with longer wavelengths. For wavelengths between 350 nm and 700 nm, one can write a_{CDOM} as [Hoepffner and Sathyendranath, 1993, Roesler et al., 1989, Maritorena et al., 2002, Martin, 2014]

$$a_{CDOM} = a_{CDOM}(\lambda_0) exp[-S(\lambda - \lambda_0)] \tag{3.2}$$

Or in other words, the absorption from CDOM and inorganic particles equals the functional dependence of the absorption on wavelength, times the CDOM absorption value at a specific wavelength. Where λ_0 is usually set to $443nm$, and S is a constant for a specific species and sat to $0.0206m^{-1}$. [Hoepffner and Sathyendranath, 1993, Roesler et al., 1989, Maritorena et al., 2002, Martin, 2014]

Phytoplankton

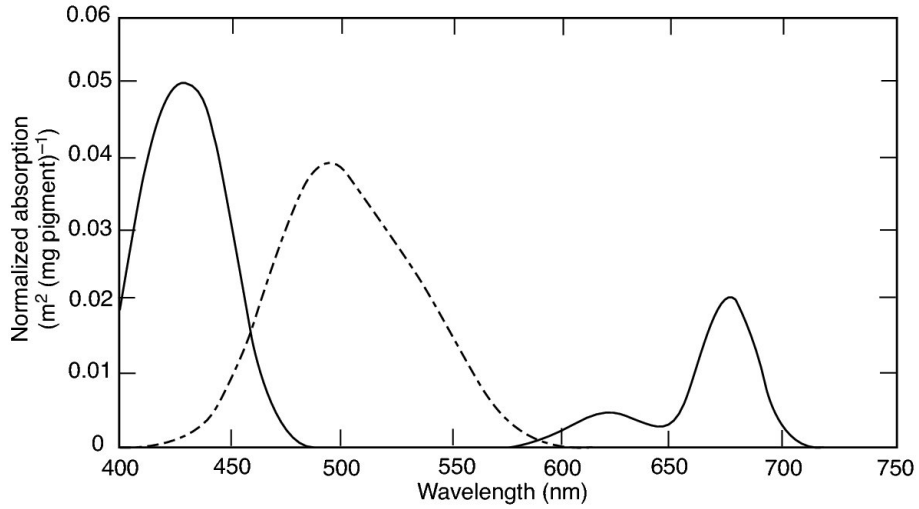

Figure 3.4: The wavelength dependance absorption of phytoplankton. The solid line is the normalized absorption for CHL-a, and the dashed line is the normalized absorption for carotenoids (pigments poduced by plants and alge [Stahl and Sies, 2003]). (From [Martin, 2014] with data from [Hoepffner and Sathyendranath, 1993])

We can see from Figure 3.4 that we have two significant absorption peaks for chlorophyll *a*. One around 440 nm in the blue band, and one around 665 nm in the red band, where the peak in the blue band is almost three times greater than the peak in the red. Furthermore we have that the absorption of phytoplankton is zero between wavelengths 490 and 580, and within this region lays the green spectral band. This is the reason for chlorophyll appearing green in blue oceanic areas. [Martin, 2014]

The phytoplankton absorption can be written as

$$a_{ph}(\lambda) = C_a a^*_{ph}(\lambda) \tag{3.3}$$

where C_a is the concentration of chlorophyll and a^*_{ph} is the coefficient of the specific absorption of chlorophyll. To put it another way, the absorption of phytoplankton is equal to the chlorophyll concentration times the coefficient of the specific absorption of chlorophyll. [Martin, 2014]

3.2.5 Scattering

The total backscattering properties can be described by

$$b_T(\lambda) = b_W(\lambda) + b_p(\lambda) \tag{3.4}$$

where b_T is the total backscatter, b_W is the backscatter value from clear water and b_p is the backscatter from CDOM and particles. [Martin, 2014]

In a study from Mobley(1995), he writes that even small quantities of particles at presence in the water column, will increase the scattering coefficient by an order of magnitude. The reason is that the particles will generate a strong forward scatter. Depending on the size of the particles, the scatter and the wavelength dependence will be different. Small particles will show a tendency towards Rayleig solution, while larger particles will show tendensy towards Mie solution. For smaller particles the forward scattering will be smaller and have a stronger wavelength dependence, while for larger particles the forward scattering will be larger and have a weaker wavelength dependence. Harbor areas with large particles will have a higher scattering than coastal areas with smaller particles, while clear ocean will have smaller scattering. [Martin, 2014, Mobley, 1995]

In other words, the more suspended material lead to an increase in forward scattering up to five orders of magnitude, and an increase in backscatter up to one order of magnitude. Compared to the forward scattering, the backscatter is relatively small. [Martin, 2014, Carder et al., 2002]

The particle and CDOM backscatter coefficient can be written

$$b_p(\lambda) = b_p(\lambda_0)[\lambda/\lambda_0]^{-\lambda} \tag{3.5}$$

where Y is a power-law exponent and depends on the scattering. If the scattering is from small particles with stronger wavelength dependence, $Y < 0$. And if the scattering is from larger particles, $Y = 0$. $\lambda = 443nm$. [Martin, 2014, Carder et al., 1999]

To observe phytoplankton, CDOM and particles by using ocean color instruments, one need to make sure the instrument takes images at specific wavelengths. From wavelength 443 nm at the chlorophyll absorption peak and the

CDOM dominating peak at 410 nm, we can get information of chlorophyll and CDOM concentrations. As well, we need information between 500 nm and 550 nm, where chlorophyll is absorbed and carotenoid absorption is dominating. If we take this into consideration, we can try to find the concentration of these particles in ocean water. [Martin, 2014]

3.2.6 Algorithms Used for Ocean Color Parameters in This Thesis

The search for accurate concentrations of chlorophyll in coastal and open oceans from ocean color remote sensing happens through ocean color algorithms. Because of the complex case 2 waters, it can be difficult to differentiate between chlorophyll and CDOM. Therefore, one need to use different algorithms for case 1 and case 2 waters. For this thesis project, Sentinel-3 Level-2 products will be used. These level-2 products have been derived using the following algorithms.

CHL

In this thesis, level-2 Full Resolution Water & Atmosphere geophysical products data from the Sentinel-3 satellite will be used. Chlorophyll data will be taken from the OLCI-instrument, and the CHL-*a* concentration will be calculated with two algorithms depending on what case of water it is. The reference for the algorithm in case 1 waters are collected from the Sentinel-3 OLCI Level-2 Algorithm Theoretical Basis Document for Ocean Color Products in Case 1 Water [Antoine, 2010], while the reference for the algorithm in case 2 waters are collected from the Sentinel-3 OLCI Level-2 Algorithm Theoretical Basis Document for Ocean Color Turbid Waters[Doerffer, 2010].

Case 1 Waters

Case 1 waters, or open waters, are calculated with the OC4Me algorithm. OC4Me is a Band-Ratio Algorithm, and it is called a Maximum Band Ratio (MBR) semi-analytical algorithm developed by [Morel et al., 2007]. This

algorithm is the MERIS[1] algal pigment 1 forth-order polynomial algorithm merged with analysis of AOPs(Apperent Optical Properties) measured in-situ data over the past decades in different ocean areas. [Tilstone et al., 2017, Morel and Antoine, 2011]

The OC4Me algorithm gives out the concentration of CHL-a derived from remote sensing reflectance(R_{rs})(in the blue and green areas in the visible spectrum) and in-situ measurements of chlorophyll. [ESA, nd c] The input of the algorithm is R_{rs} at two to four wavelengths between 440 and 670 nm, and gives out the concentration of chlorophyll in mgm^{-3}.

The OC4Me Algorithm is expressed as

$$log10[Chl] = \sum_{x=0}^{n} A_i[log10(\rho_{i,j})_0]^x \tag{3.6}$$

where $\rho_{i,j}$ is the ratio of the irradiance reflectance, R, at band $i(\lambda i)$ to band $j(\lambda j)$. The maximum found among the three ratios that are formed using 2-4 bands, is the value of the irradiance reflectance ratio. The band used here for λi is 443 nm, 490 nm or 510 nm, while for λj 560 nm is used. [Morel and Antoine, 2011, ESA, nd c, ESA, nd e]

Its polynomial structure of 4_{th} order, $n = 4$, gives five coefficients. These are derived using AOPs measured in-situ data that are collected over the past decade in different ocean areas. The coefficients are: [ESA, nd e]

A_0 = 0.4502748

A_1 = -3.259491

A_2 = 3.522731

A_3 = -3.359422

1. MERIS Algorithm Theoretical Basis Document(ATBD) 2.9 (`https://earth.esa.int/documents/700255/2042855/MERIS_ATBD_2.9_v4.3+-+2011.pdf`)

$A_4 = 0.949586$

Since the OC4Me algorithm uses the irradiance reflectance R and since the MERIS atmospheric correction provides directional reflectance, ρ_w, one need a conversion

$$R = \frac{\rho_w Q}{\pi \mathbb{R}} \tag{3.7}$$

where Q is a factor from [Morel et al., 2002], and $\mathbb{R}$ is the geometrical factor defined as

$$\mathbb{R}(\theta') = \left[\frac{(1-\bar{\rho})}{(1-\bar{r}R)} \frac{(1-\rho_F(\theta'))}{n^2} \right] \quad \text{(subscript 0 when } \theta' = 0) \tag{3.8}$$

where $\mathbb{R}$ at air-sea interface, merges all reflection/refraction as in [Morel and Gentili, 1996], n is the refractive water index, $\bar{\rho}$ is, for downward irradiance at the sea surface, the mean reflection coefficient, $\rho_F(\theta')$ is, for incident angle θ, the Fresnel coefficient, $\bar{r}$ is, for upward irradiance at water-air interface, the average reflection, and θ' is the refracted viewing angle $\theta' = sin^{-1}(nsin(\theta v))$. [Morel and Antoine, 2011, ESA, nd c, ESA, nd e]

Case 2 Waters

Case 2 waters, or coastal waters, are calculated with an Inverse Modelling Technique(IMT), that uses an Inverse Radiative Transfer Model-Neural Network(IRTM-NN) to estimate different coefficients from normalized water-leaving reflectance at different OLCI bands. This algorithm gives out coefficients that can be used to derive CHL-*a* concentration. [ESA, nd b]

For this algorithm, also following the heritage of MERIS, an artificial neural network(NN) has been chosen as a multiple non-linear regression technique. The neural network will convert the directional water leaving radiance reflectance(RLw) into several Inherent Optical Properties(IOP) - and

these properties can be converted into different concentrations of constituents. To convert these properties to concentrations of constituents, regressions are used. Here is an overview to the steps that create the NN algorithm. [ESA, nd b, Morel and Antoine, 2011]

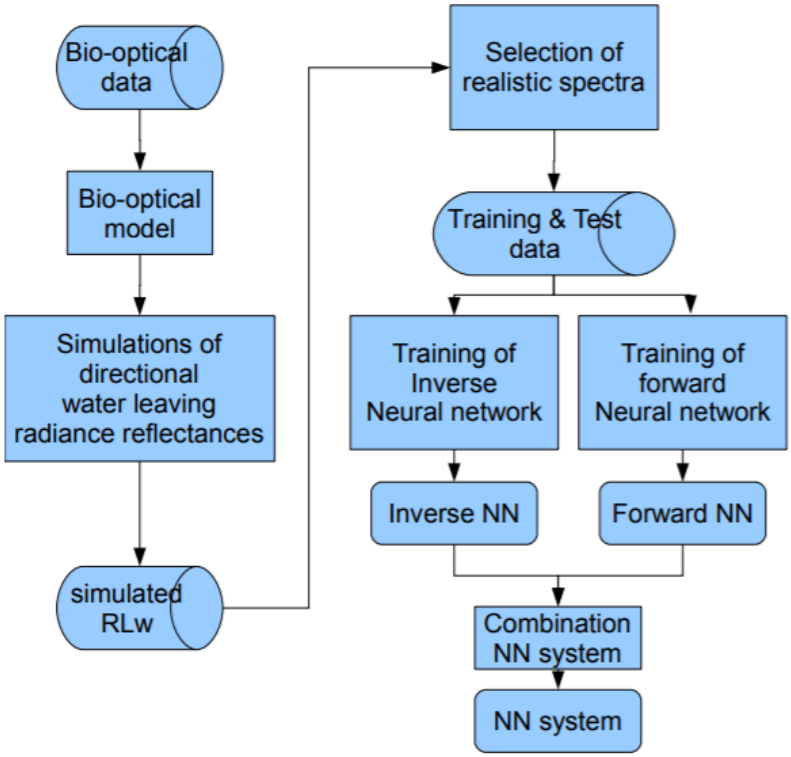

Figure 3.5: Steps overview to create the NN algorithm. Figure from the Sentinel-3 ATBD Ocean Color Turbid Water (From [ESA, nd f]

The output coefficient from the NN system will depend on the training process of the inverse and forward neural network. In this process, directional RLw are simulated with a complex radiative transfer model. This radiative transfer model includes a bio-optical model which expresses the inherent optical properties that describes optically active different classes of water constituents that affect RLw and the underwater light field. [ESA, nd b, Morel and Antoine, 2011, ESA, nd f]

Description of the algorithm:

The bio-optical model have been based on pure water and five components:

1. absorption by phytoplankton pigments
2. absorption by dissolved organic matter / fulvic acids
3. absorption by particulate organic matter / humic acids
4. scattering by total suspended matter
5. scattering by white particles

The objective is that, for case 2 waters, a mix of these five components will represent mostly standard optical properties. [ESA, nd f]

Simulation of the radiance reflectance spectra are done with Hydrolight. Hydrolight is a numerical radiative transfer model, which calculates the distributions of sprctral radiance and associated quantities for water bodies. [Mobley, 1998, ESA, nd f]

For all of the OLCI spectral bands, the radiance distribution is calculated with Hydrolight for 36x24 zenith and azimuth angles(quads) for 17 sun zenith angles. The radiance distribution of RLw, are for the 15 spectral bands, calculated in the same direction as the incoming radiance.[ESA, nd f]

Selection of spectra for the training process happens through a subset of simulated RLw that are in the range of measured spectra of the North Sea by GKSS and stored in the MERMAID data set. Easily explained, the MERMAID data set is used as a selection criteria to determine, for some of the spectral bands, upper and lower reflectances for the selection of realistic spectra. [ESA, nd f]

Training and test data are chosen from the 15 OLCI spectral bands with wavelengths 400, 412.5, 442.5, 490, 510, 560, 620, 665, 673.75, 681.25, 708.75, 753.75, 778.75, 865, and 1020 nm. The 10 chosen to train the neural network are 400, 412.5, 442.5, 490, 510, 560, 620, 665, 673.75 and 708.75 nm.

[ESA, nd f]

The neural network system consist of two neural networks; one inverse network and one forward network. The inverse neural network is used to describe the IOPs from the measured RLws. The forward neural network is used to make a test to see if the input RLw spectrum is in concurrence with the spectra that is included in the training data set. [ESA, nd f]

The structure of the inverse NN is as follows; 15 input neurons, 4 hidden layers with 45, 20, 15 and 8 neurons, and 5 output neurons. The input neurons are the log10 RLws of the OLCI spectral bands 1-9 and 11, salinity, temperature and 3 angles (the sun zenith angle, the nadir viewing angle and the azimuth difference between sun direction and viewing direction). Output are the five IOPs mentioned above with the bio-optical model. [ESA, nd f]

The structure of the forward NN is as follows; 10 input neurons, 3 hidden layers with 45,20 and 15 neurons, and 11 output neurons. The input neurons are the log10 of the five IOPs mentined above, salinity, temperature and the same three angles as in the inverse NN. Output are the log10 RLws from the 11 first bands of MERIS. [ESA, nd f]

Standard for NN is hat the inverse NNs output is used as input to the forward NN. To determine how far the input spectrum is out of scopt with the training data set, the output from the forward NN is compared with the measuered RLw spectrum in consistent with

$$X^2 = \sum_{i=1}^{n} \left((RLw_m(i) - RLw_s(i))^2 / n \right) \tag{3.9}$$

where X^2 is the out of scope distance, $RLw_m(i)$ is the measured radiance reflectance for OLCI band i, and $RLw_s(i)$ is the simulated spectrum from forward NN. The RLw values can be very low such that they can become uncertain or negative. To avoid this, one define a threshold for all RLws. [ESA, nd f]

Converting the IOPs into concentrations are done at last to give users concentrations of different constituents instead of IOPs. This is converted on the bases of empirical relationships. [ESA, nd f]

TSM and CDOM

Level-2 data from Sentinel-3 and the OLCI instrument gives both TSM and CDOM concentrations calculated with Neural Network algorithms. Neural Network algorithms tends to give more accurate results in complex areas. The NN system described for case 2 waters are the same that is used for these contituents as well. [ESA, nd n, ESA, nd a, ESA, nd f]

3.2.7 Errors With the Algorithms

None of these algorithms can give a perfectly correct result. There will always be errors, and it is hard to know how dominant these errors are. If in-situ data are available, one can test them up with the data from the algorithm to see how correctly it is. When this is said, many ocean color algorithms are good algorithms to use, but one must not forget that errors will show up. Chlorophyll data for case 1 water and case 2 water are often found with different algorithms. Case 2 waters (coastal waters) are more complex and contains CDOM that often causes errors to classification of chlorophyll in coastal areas.

Another problem can occur with the algorithm for case 1 water. This comes from the fact that this algorithm is merges with in-situ data collected over the past decades from different areas in the ocean. If these areas are far from the study areas we use in this thesis, we might get less accurate answers.

3.3 Synthetic Aperture Radar(SAR) Remote Sensing

Synthetic Aperture Radar(SAR) remote sensing is quite different from optical remote sensing such as Ocean Color remote sensing. SAR systems are side-looking systems that transmits microwave radiation and receive the backscattered radiation. The received backscatter radiation is saved and constructed into an image. [Campbell, 2011]

To obtain two- or three-dimensional images with high resolution, SAR satellites uses the motion of the radar antenna. Typically, one says that the larger the aperture, the higher the resolution on the images will be. A synthetic(moving antenna) will therefor allow a SAR satellite to create, with a relatively small physical antenna, an image with high resolution. [Campbell, 2011]

A SAR satellite will receive signals scattered from the landscape during an interval of time, as the satellite moves along its flight path. The satellite saves and stores the backscattered information and re-constructs the received signal as if they were received by a single antenna. When re-creating the image with the correct positions of features as representation of the landscape, this can be a complicated process. This problem occurs because features in the landscape will experience different frequency shifts relative to their distance from the satellite. This effect is called the Doppler shift. [Campbell, 2011]

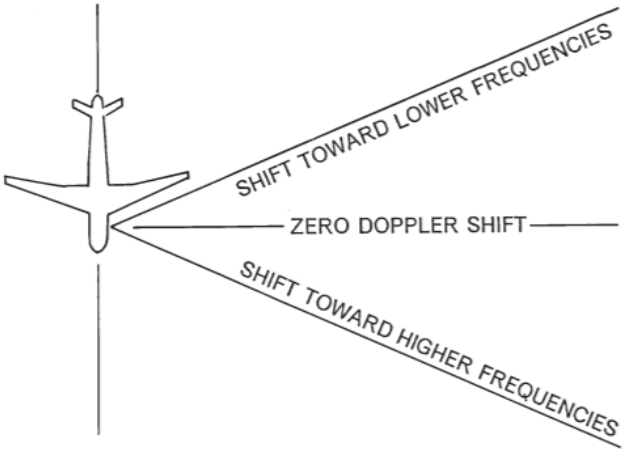

Figure 3.6: Features within the field of view of the radar will experience frequency shifts. (From [Campbell, 2011])

As we can see from Figure 3.6, depending on where the feature is in the field of view of the radar, it will experience a frequency shift towards lower or higher frequency depending on the position of the feature relative to the radar.

SAR imagery allows for the detection of structures in the ocean like ocean swell, currents and internal waves. A knowledge of wave conditions in coastal waters will help researches gain information relevant to their study area, and can actually provide better safety for many operations. The values in SAR Normalized Radar Cross Section(intensity) images will have variations in its short-scale surface roughness. This roughness are induced by geophysical phenomena. The intensity image of the sea surface will be modified by wind stress, variations in ocean currents and surface slicks. [Henderson, 1998]

[Henderson, 1998] also informs the SAR images associated with thermal images of sea surface temperature, have shown to be good tools together for observing currents from satellite images.

Overall, Sentinel-1 provides us with different products that can give us information about the ocean.SAR images are sensitive to surface roughness that are modulated by a surface current. Because of this, mesoscale oceanic phenomena can be seen in SAR images. Relative to this project, we are most interested

in information about motion of wind, waves and currents in coastal waters. [ESA, nd d]

3.3.1 Geophysical Doppler Product

When scanning the ocean, and recording backscatter with a SAR satellite, one get phase information from the ocean backscatter. This phase information can be used to obtain range velocity, or Doppler centroid frequency equivalently. This has previously been demonstrated to give valuable estimates of ocean surface currents and near surface wind speed. [Engen et al., 2014]

Based on the satellite orbit/attitude and the rotation of Earth, one can predict a Doppler centroid. In addition, one can record a Doppler centroid frequency over the ocean. The difference between these Doppler centroids, the Geophysical Doppler, is a measure of the radial velocity of the moving ocean surface. Since this Geophysical Doppler product is based on the difference between the two Doppler centroids, it will be very sensitive to the motion of scatters that comes from winds, ocean waves and surface currents. [Engen et al., 2014]

In this project, I use radar intensity images and, derived from SAR data, a geophysical Doppler product that tells us about the velocity field in the line of sight direction. An image showing the velocity field in an area, can help with the analysis of motion in ocean color images.

4

Lofoten, Vesterålen and Senja

The study area for this thesis is the unique areas outside Lofoten, Vesterålen and Senja. As mentioned in the introduction, these areas are quite popular for tourists, outdoor enthusiasts and photographers, because of their incredible nature and significant marine life. These areas are unique, not only because of their nature, but also because of the large fish stocks that pass these areas every year. The marine life in these areas are vulnerable, as well as important for the many fishing communities that depend on the income these areas bring with them. [Naturvernforbundet, nd]

This chapter presents some of the coastal dynamics in the study area, before it shows the ocean color parameters for the area.

4.1 Coastal Dynamics for Study Area

The Arctic region is dominated by large areas of ocean waters. In these areas the warmer North Atlantic current and the North Pacific current meets cold Arctic oceans. The study area for this thesis is an area in the Norwegian Sea outside Lofoten, Vesterålen and Senja, see Figure 4.1

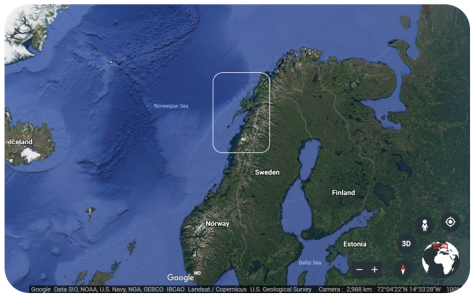

(a)

(b)

Figure 4.1: The study area for this thesis. Images collected from Google Earth (From `https://www.google.com/intl/no/earth/`)

Lofoten, Vesterålen and Senja are known to be unique areas. They are ar-

eas known for their incredible nature, ocean as far as the eye sees and a significant marine life and high marine productivity. These are the areas for Norway's most important fish stocks, and play a major role in the marine ecosystems while they form the basis for the country's most important fisheries. [Naturvernforbundet, nd]

4.1.1 Ocean Currents

The ocean currents for this study area will be slightly different during the season on a local scale, but they have a clear trend. Figure 4.2 shows the ocean currents for the Norwegian Sea, the Barents Sea, the Greenland Sea and the North Sea.

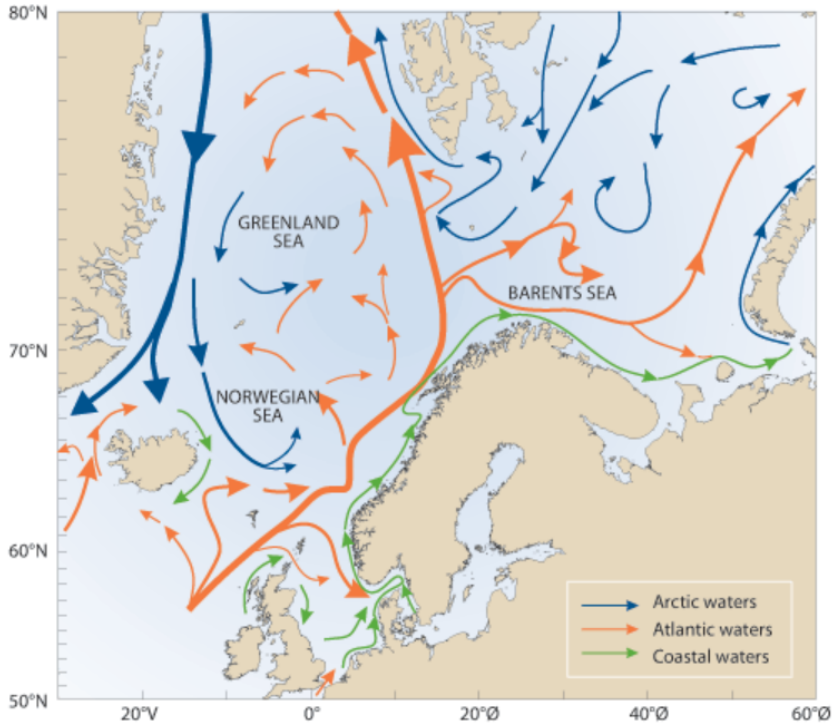

Figure 4.2: The system of ocean currents in the Norwegian Sea, the Barents Sea and the Greenland Sea. (From [Regjeringen.no, 2002])

As we can see from Figure 4.2, the North Atlantic current brings warm water northwards as it swipes past the Norwegian coast and runs further north

meeting Arctic waters. Figure 4.3 shows a more detailed image of ocean currents outside the study area.

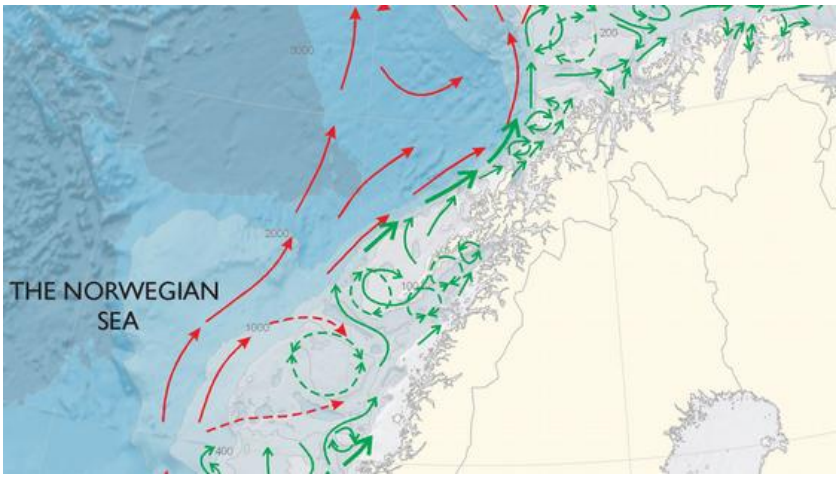

Figure 4.3: Ocean currents study area.
(From [Havforskningsinstituttet, 2011])

As we can see from Figure 4.3, the island group Lofoten and Vesterålen gives resistance to both the North Atlantic current and the Norwegian coastal water, which affects both currents. Because of upwelling from the continental shelf-edge, nutrient rich warmer water is brought up to the surface mixing with the Norwegian coastal water. As we can see from the figure, the green arrows represents coastal water. At the Norwegian coast, the Norwegian coastal water has the same direction as the North Atlantic current. This is a phenomenon that often leads to high marine productivity many places on Earth. [Havforskningsinstituttet, 2011] Outside Lofoten, Vesterålen and Senja the continental shelf is quite narrow. Thus, the mixing of different waters will happen on a small area outside the study area. The fronts between these water masses will therefore be closer to land compared to other places at the Norwegian coast, and they will also be unstable because of the topography of the continental shelf. The tide in this area is very significant, and some areas have a difference of more than 1.5 meters. This leads to a forceful mixing of the different water masses. [Havforskningsinstituttet, 2011]

4.1.2 Upwelling

The study area is known to have upwelling of nutrient rich water. Due to stable and nutrient rich inflow of water, as well as the wind and ocean currents in the study area, the water mixes with upwelled water due to the topography of the area. This upwelling feeds the surface waters with nutrients helping phytoplankton to grow. [Myhre, 2013] This is probably a major source for the large fish stocks in the area. As mentioned in chapter 2.4, upwelling of nutrient rich water causes the increased phytoplankton growth is often linked with cold water that flows up to the surface. Because of this phenomenon, it will be interesting to investigate if there exists a relation between ocean color parameters and sea surface temperature. At first thought, correlation and image subtraction will be natural to check. Another interesting thing to investigate here, will be to check if the relationship is linear or non-linear.

4.2 Ocean Color Parameters

Ocean color parameters such as the concentration of chlorophyll, TSM and CDOM, and sea surface temperatures, can give information about the biological activity and the water quality in the top layer of the ocean.

4.2.1 Chlorophyll(CHL)

Using images of chlorophyll concentration gives a measure of the amount of chlorophyll in different areas, and therefore it can tell us something about the biological activity. Depending on what case of water we are studying, we use either CHL_{NN} (case 2) or CHL_{OC4Me} (case 1). Figure 4.4 shows an ocean color image with the concentration of chlorophyll(this is a CHL_{OC4Me} image).

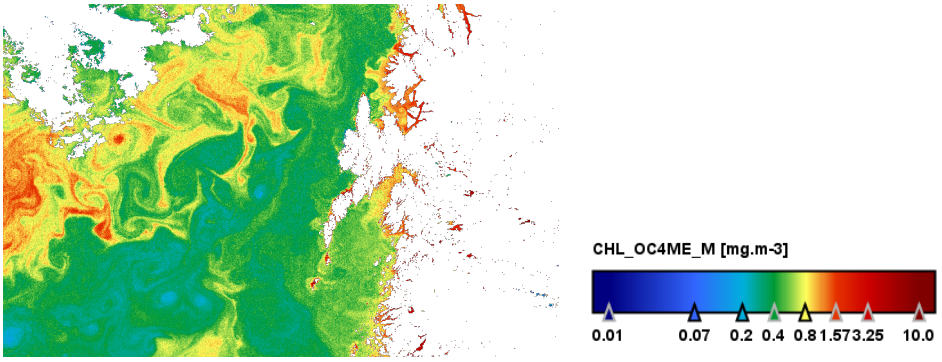

Figure 4.4: Ocean color data with chlorophyll concentration outside study area 07.28.2018. (Image with colorbar produced in SNAP(Sentinel Application Platform))

From Figure 4.4 land and cloud areas are illustrated in white, and ocean areas in a range of colors. These colors tells us the concentration of chlorophyll in water, where blue is the lowest and red is the highest amounts(mgm^{-3}). The range for the concentration of chlorophyll in Figure 4.4 is between 0 and 10 mgm^{-3}.

4.2.2 CDOM

As mentioned in Chapter 4.3, CDOM is colored dissolved organic material. It is produced both on land from land based run-off containing dissolved humic and fulvic acid, and at sea from the degradation of phytoplankton through photolysis. Water with high amounts of CDOM will look brown- and yellow-ish. For example in inland waterways, one can often observe brownish waters. This is because of high concentration of CDOM. Figure 4.5 shows an image of ocean color data showing the concentration of CDOM.

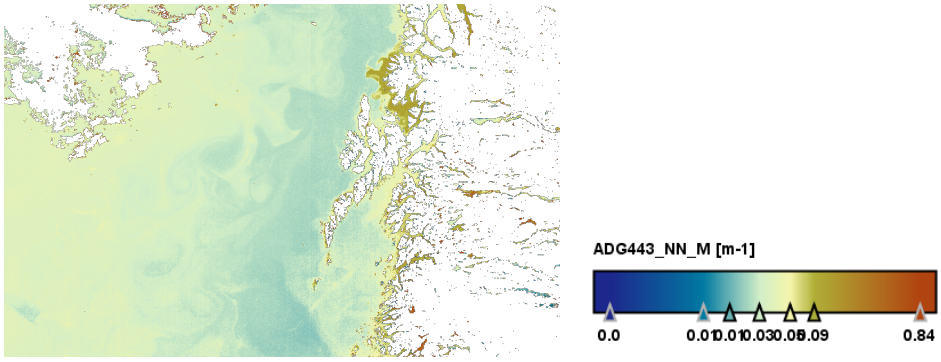

Figure 4.5: Ocean color data with CDOM concentration outside study area 07.28.2018. (Image with colorbar produced in SNAP(Sentinel Application Platform))

From Figure 4.5 land and cloud areas are illustrated in white, and ocean areas in a range of blue, yellow and brown-ish colors. These colors tells us the amount of cdom in the water, where blue and light yellow is the lowest and the rusty orange is the highest amounts(m^{-1}). The range for the concentration of CDOM in Figure 4.5 is between 0 and 10 m^{-1}.

4.2.3 TSM

TSM is, as mentioned earlier, total suspended material. It is important for the control of water quality, especially for turbid inland waters. TSM carries nutrient input and photosynthetic process, and will therefore affect the aquatic ecosystem. When it comes to case 2 waters, one often link TSM to primary production, heavy metal fluxes and micro-pollutants. Inland turbid waters can also be linked to problems with sediment transport. [Song et al., 2012]

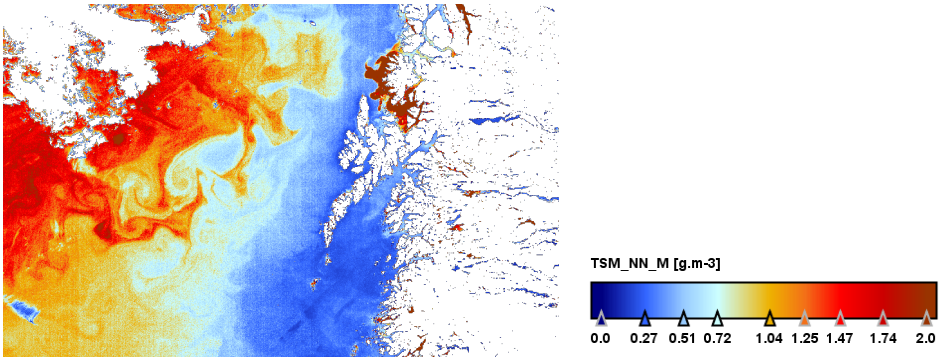

Figure 4.6: Ocean color data with TSM concentration outside study area 07.28.2018. (Image with colorbar produced in SNAP(Sentinel Application Platform))

From Figure 4.6 land and cloud areas are illustrated in white, and ocean areas in a range of blue to red-ish colors. These colors tell us the amount of TSM in the water, where blue is the lowest and the red is the highest amounts(gm^{-3}). The range for the concentration of TSM in Figure 4.6 is between 0 and 2 gm^{-3}.

4.2.4 SST

Sea Surface Temperature(SST) data contains data of the sea surface temperature over the ocean. Figure 4.7 is an example of an SST image.

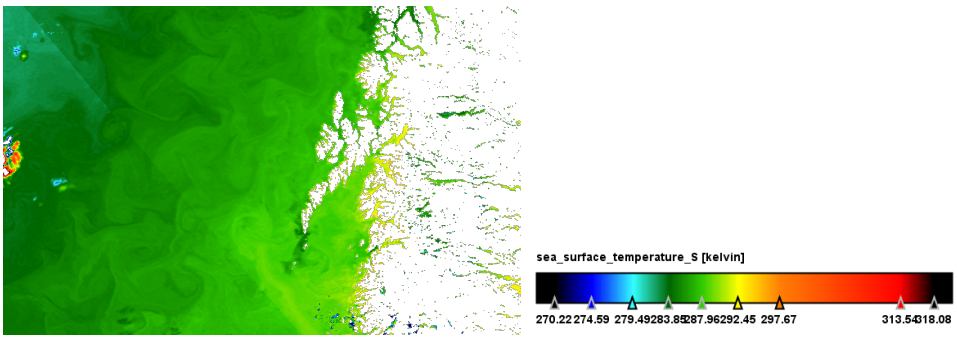

Figure 4.7: Sea Surface Temperature(SST) data outside study area 28.07.2018. (Image with colorbar produced in SNAP(Sentinel Application Platform))

From Figure 4.7 land areas are illustrated in black and ocean areas in a range of blue to red colors. These colors tell us the degrees(Kelvin) of water temperature, where blue is the lowest and the red is the highest degrees(K). The range of the sea surface temperature in Figure 4.7 is between 270 and 320 K.

4.3 Ocean Dynamics

Turbulent structures in the ocean are generated by several different factors. Depending on coastal instability, irregular topography, coastal currents, shears, islands and other obstacles, all affects and give rise to the turbulent structures in the ocean. These turbulent structures can be mesoscale fronts, eddies and filaments. [Lovecchio et al., 2018]

From ocean color chlorophyll data one can spot some turbulent structures in the ocean, especially filaments.

4.3.1 Upwelling Areas

Along the western boundaries of the continent, coastal regions are characterized by winds flowing towards the equator inducing an offshore Ekman transport. This generates an upwelling of cold nutrient rich water near the shore, increasing the biological activity. From chlorophyll data one can see where the concentration of chlorophyll is highest. In upwelling areas one can clearly see high amounts of chlorophyll. [Lovecchio et al., 2018]

From ocean color data with the concentration of chlorophyll, one can clearly see areas along the coast containing high amounts of chlorophyll. Many of these areas are upwelling areas, and others have a large input of nutrients giving rise to phytoplankton.

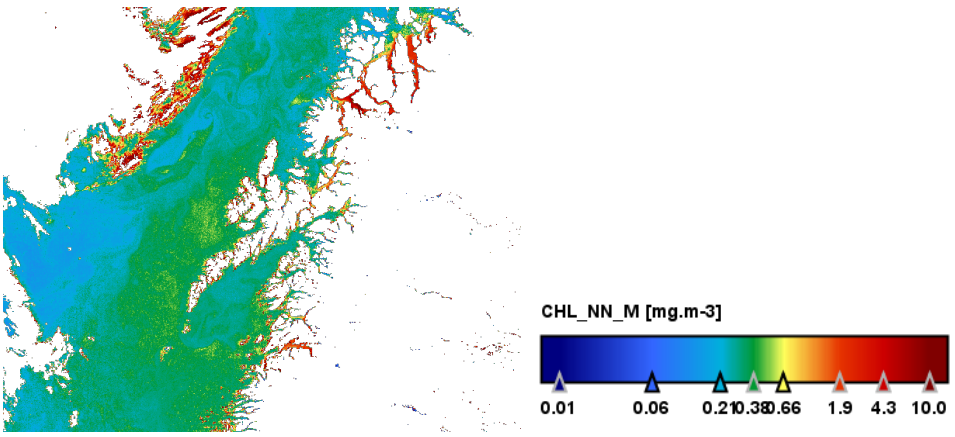

Figure 4.8: Ocean color data with CHL_{NN} concentrations outside study area 10.05.2018. (Image with colorbar produced in SNAP(Sentinel Application Platform))

In Figure 4.8 we can see the study area. This data is calculated with a Neural Network (NN) algorithm giving better results in case 2 waters. We can see high concentrations of chlorophyll in coast and fjord areas, and on the west side of Lofoten and Vesterålen. Top left in Figure 4.8 we can see a black area with high concentrations of chlorophyll. This is the effect from clouds on ocean color data. So, we should just look away from this area. All of the green area outside Lofoten contains moderate amounts of chlorophyll. One of the factors deciding these amounts of chlorophyll, can be the known upwelling area mentioned in the introduction part, due to offshelf transport of surface water.

4.3.2 Ocean Currents

As mentioned in chapter 3.5.1, the coastal currents outside the study area meet the North Atlantic current (see Figure 4.2 and 4.3). This phenomenon, where the North Atlantic current and the coastal current flow the same direction, leads to a high marine productivity. We can clearly see this in our study area in Figure 4.8. Because of the narrow continental shelf, the topography and the tide difference outside our study area, the fronts of the water masses will act unstable. This can be slightly difficult to see from ocean color data, but we can

clearly see motion in the water.

In Figure 4.8, in the area between Senja and the clouds, we can see some hints of circle-ish features. These are ocean current eddies, making turbulent circle like feature in the ocean.

Filaments are also to be seen in these images. They look like "arms" in ocean color CHL data. Here are some examples.

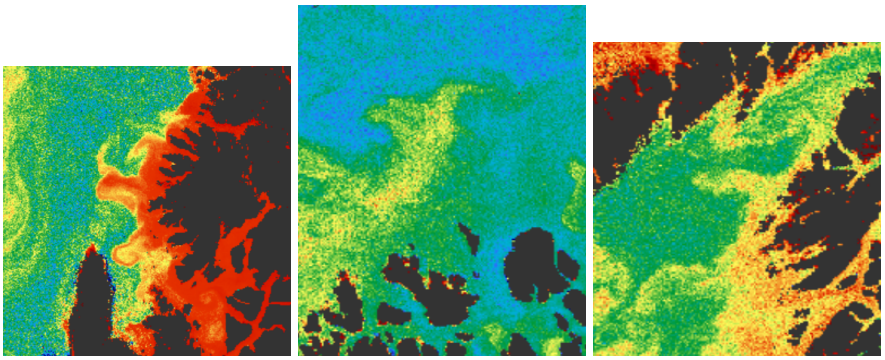

Figure 4.9: Filaments. (Image with colorbar produced in SNAP(Sentinel Application Platform))

4.3.3 Water Masses

From looking at SST images, one can clearly see indications of different water masses. We can see fronts meeting and mixing. We can see how the turbulent water features brings and mixes the different water masses.

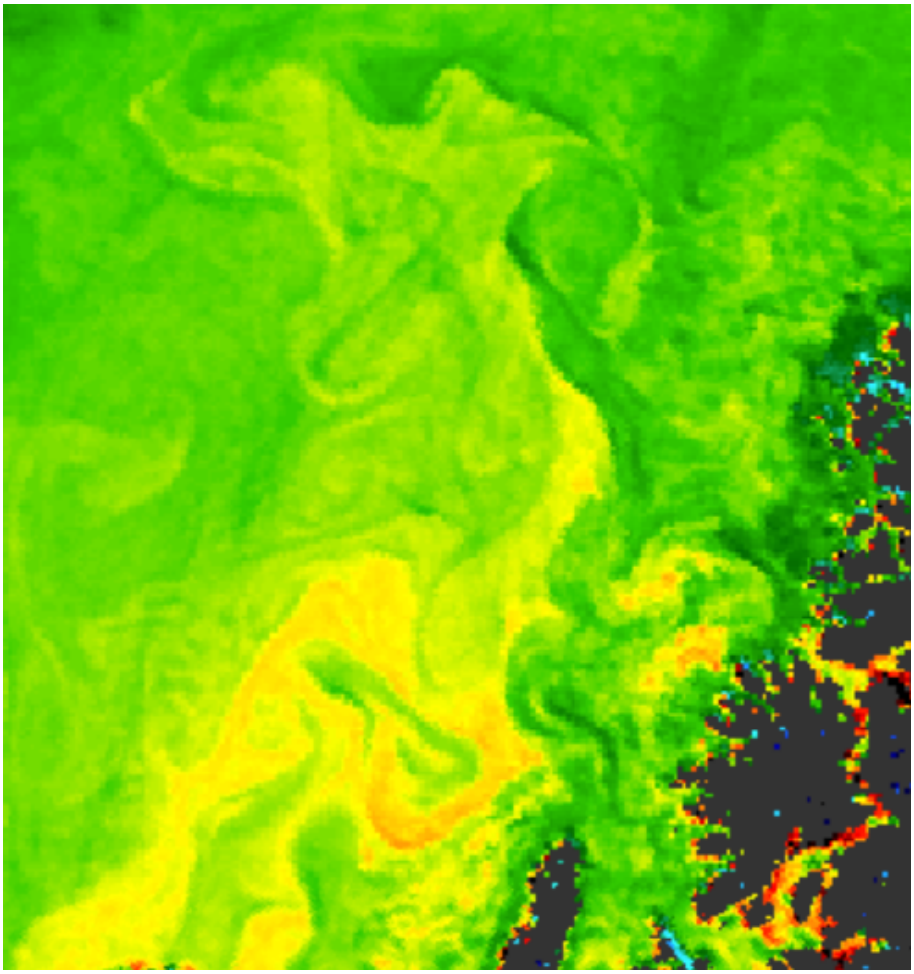

Figure 4.10: Sea Surface Temperature(SST) data outside study area 10.05.2018. (Image with colorbar produced in SNAP(Sentinel Applcation Platform))

If we compare the motion in Figure 4.7 to the normal motion of currents outside the study area in Figure 4.3, we can see that in the North of Senja, currents start flowing northwards. Just as we can see from the SST image in Figure 4.7.

4.4 Similarities Between CHL and SST

Only looking at images of CHL and SST, one can clearly see similarities in the patterns in the two images shown in Figure 4.11.

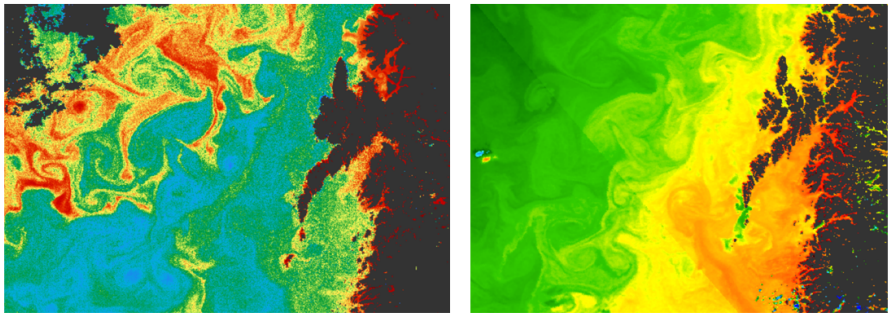

Figure 4.11: Images of chlorophyll concentration and sea surface temperature, 28.07.2018. (Image with colorbar produced in SNAP(Sentinel Applcation Platform))

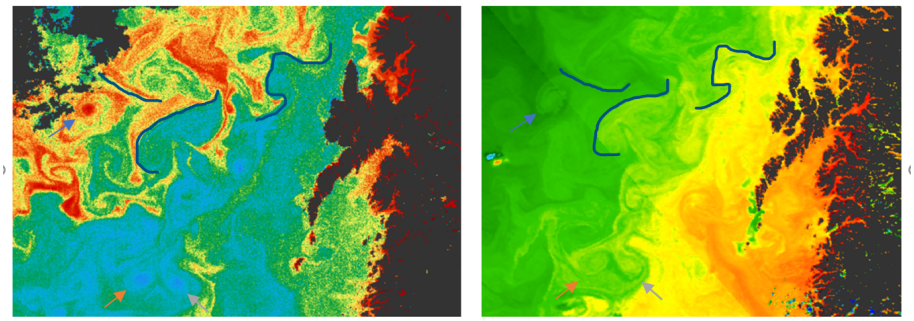

Figure 4.12: Figure 4.11 with a few pointers showing some similarities between a) and b). (Image with colorbar produced in SNAP(Sentinel Applcation Platform))

In Figure 4.12, some of the similarities are pointed out with arrows or dark blue pen. We can clearly see some of the rotating eddies (see arrow blue, orange and grey) in both images. Furthermore we can see a similar pattern for both the CHL and the SST image where the blue pen is drawn. These fronts show up for both of these images and for TSM and CDOM images as well. As we can see in

Figure 4.12, we can see a connection between areas with high amounts of CHL in the left image, and areas with colder water in the same areas in the right image. This correspond with the theory from chapter 2 and 3 about upwelling, where colder water tends to have more nutrients that helps phytoplankton growth. It would be interesting to see if these patterns also appear in radar imaging.

Observing the CHL image in Figure 4.12 and comparing it to the currents that can be seen in Figure 4.3, we can see that the area with higher concentrations of CHL to the top left corner corresponds with the North Atlantic current, and the areas with CHL close to land seems to be generated by upwelling and the Norwegian coastal currents. On the tip south of Lofoten, we can also observe area with a bit colder water from the SST image(the green area on the tip of Lofoten) in Figure 4.12, and areas with higher concentrations of CHL in the CHL image. This is considered to be upwelling of nutrient rich colder water that increases phytoplankton growth.

5

Sensors and Satellites

To retrieve remote sensed data we need to use for example satellites or air crafts with sensors that collect the information we want. In some cases, one need several instruments as well to get the information one seeks. This chapter presents differences with optical vs. microwave remote sensing. Thereafter, it addresses information about the satellite and sensors that will be used to collect data in this thesis.

5.1 Introduction

As mentioned, when using remote sensing, the satellite instrument is not in physical contact with the investigating object. Because of this, the properties of the satellite instrument must be inferred from the frequency distribution and intensity of the radiation that is received. This radiation has propagated through the atmosphere, and therefore its distribution will depend on the propagation. We have three princpal sources for the radiaton; reflected solar radiation, blackbody radiaton (emitted from surface) and backscattered energy (recieved at sensor). [Martin, 2014]

The radiation does not only depend upon the propagation through the atmosphere, it also depend on the sensor. Depending on what information you are interested in, you need to choose the right sensor to use. The sensor have to be designed such that it uses appropriate wavelengths for the investigating object. The recieved data can now be collected and organized into data sets so that the information can be viewed. There are two ways of collecting satellite data; by optical remote sensing and microwave remote sensing. [Martin, 2014, Elachi and Van Zyl, 2006]

5.2 Optical vs Microwave Remote Sensing

We can classify imaging sensor systems as passive and active imaging systems.

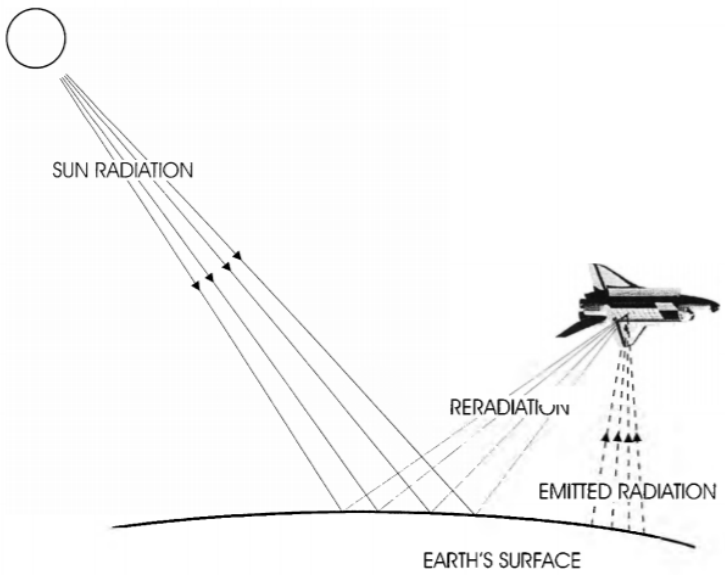

Figure 5.1: Electromagnetic radiation received by a passive imaging sensor.(From [Franceschetti and Lanari, 1999])

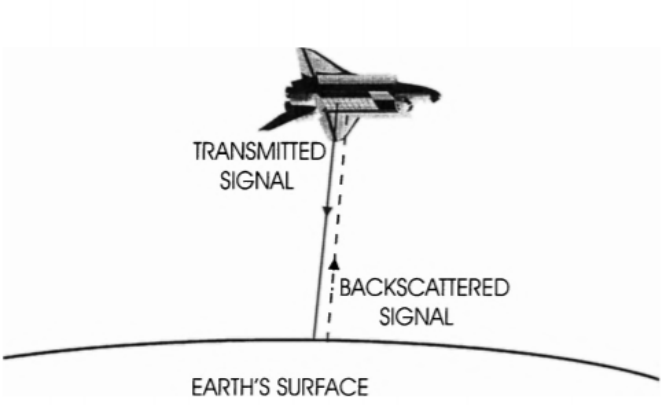

Figure 5.2: Electromagnetic radiation received by an active imaging sensor. (From [Franceschetti and Lanari, 1999])

Optical remote sensing expands from visible wavelengths and into the near infra-red wavelengths. We can divide optical remote sensing into active and passive sensing, see Figure 5.1 and Figure 5.2. The most commonly used one is the passive type of remote sensing, which depends upon illumination from the sun to reach Earth's surface and reflect back to the satellite to be recorded. Because of the dependence of the sun, this type of remote sensing is restricted to daylight and cloud-free periods. This will also vary from where you are on Earth, since the length of daylight will vary from place to place and from the time of year, and it will be very dependent of the weather. Examples of satellites that use passive optical sensors are Landsat, MODIS and Sentinel-3. An active optical sensor will send out radiation and then measure the backscatterd energy. An example of a sensor of this type is LiDAR. [Martin, 2014]

Microwave remote sensing on the other hand, can also be divided into two different groups of remote sensing; active microwave remote sensing and passive microwave remote sensing. Passive remote sensing instruments observe the radiation that is naturally emitted. An example of a satellite using passive microwave sensing is SSM/I. Active remote sensing instruments, on the other hand, actually transmit energy itself and collect the backscattered energy that is emitted. An advantage of using active sensors, is the independence of illumination and weather, and is the reason why active microwave sensors are more used than passive microwave sensors. Examples of active microwave

satellites are ENVISAT, TerraSAR-X and Sentinel-1. [Martin, 2014]

5.3 Optical Imaging Systems

The optical electromagnetic spectrum extends from wavelengths of the visible spectrum (approximately 400 nm to 700 nm) and into the near infrared spectrum (approximately 700 nm to 2500 nm). The most commonly used system for optical imaging is passive systems. These systems are sensitive to variations in illumination from the sun, since they measure the reflected illumination from the ground. These systems are also sensitive to weather and night conditions, since they depend on the illumination of the sun. [Martin, 2014, Campbell, 2011]

5.3.1 Ocean Color Remote Sensing

For ocean color remote sensing one chooses to use optical passive imaging systems. This is because light penetrates water depths of 10-100 meters, and the only wavelengths that can reach theses depths are the visible and near infrared wavelengths. Furthermore, chlorophyll only absorbs certain wavelengths from the visible part of the electromagnetic spectrum. The visible spectrum is only a small part of the electromagnetic spectrum, as we can see from Figure 3.1, and it only reaches wavelengths betweeen 400 and 700 nano meters. [Martin, 2014]

5.3.2 Sentinel-3

Sentinel-3 is a multi-sensor European Space Agency(esa) satellite. It was launched in February 2017, primarily for ocean missions. However, it can also provide applcations for land and atmosphere. [ESA, nd j]

This satellite consists of two satellites; Sentinel-3A and Sentinel-3B with a phace shift between them of around 140°. Sentinel-3A launched in February 2017, while Sentinel-3B launched in April 2018. The satellite has a sun-synchronous

orbit type with orbit height 814 km above ground. Its repeat cycle is 27 days. Sentinel-3 has several different sensors aboard. Some of them are OLCI(Ocean and Land Color Instrument), SLSTR(Sea and Land Surface Temperature Radiometer), GNSS(Global Navigation Satellite System) and MWR(Microwave Radiometer). [ESA, nd j]

The satellite's main objective is measuring ocean- and land-surface color, sea-surface topography and sea- and land-surface temperature. For this thesis, we are mostly interested in data from the OLCI insturment and the SLSTR instrument. [ESA, nd j]

5.3.3 Ocean and Land Cover Instrument (OLCI)

As mentioned earlier, OLCI is an instrument on the satellite Sentinel-3. It is an instrument with 21 bands, reaching from 400 nm to 1020 nm, using a spatial resolution of 300 m. With five cameras it provides a wide field of view with swath width 1270 km. This instrument gives us both data from the ocean and land, but for this thesis we are most interested in data from the ocean. From OLCI we can get level-2 data with estimations of for example Chl-a concentration and the concentration of total suspended matter (TSM). OLCI uses spectral bands in the visible and short infrared spectrum to retrieve information. [ESA, nd k]

Table 5.1: OLCI band characteristics. (From [ESA, nd h])

Band	λ centre (nm)	Width (nm)	Function
Oa01	400	15	Aerosol correction, improved water constituent retrieval
Oa02	412.5	10	Yellow substance and detrital pigments (turbidity)
Oa03	442.5	10	Chlorophyll absorption maximum, biogeochemistry, vegetation
Oa04	490	10	High Chlorophyll,
Oa05	510	10	Chlorophyll, sediment, turbidity, red tide
Oa06	560	10	Chlorophyll reference (Chlorophyll minimum)
Oa07	620	10	Sediment loading
Oa08	665	10	Chlorophyll (2nd Chlorophyll absorption maximum), sediment, yellow substance/vegetation
Oa09	673.75	7.5	For improved fluorescence retrieval and to better account for smile together with the bands 665 and 680 nm
Oa10	681.25	7.5	Chlorophyll fluorescence peak, red edge
Oa11	708.75	10	Chlorophyll fluorescence baseline, red edge transition
Oa12	753.75	7.5	O2 absorption/clouds, vegetation
Oa13	761.25	2.5	O2 absorption band/aerosol correction.
Oa14	764.375	3.75	Atmospheric correction
Oa15	767.5	2.5	O2A used for cloud top pressure, fluorescence over land
Oa16	778.75	15	Atmos. corr./aerosol corr.
Oa17	865	20	Atmospheric correction/aerosol correction, clouds, pixel co-registration
Oa18	885	10	Water vapour absorption reference band. Common reference band with SLSTR instrument. Vegetation monitoring
Oa19	900	10	Water vapour absorption/vegetation monitoring (maximum reflectance)
Oa20	940	20	Water vapour absorption, Atmospheric correction/aerosol correction
Oa21	1 020	40	Atmospheric correction/aerosol correction

5.3.4 Sea and Land Surface Temperature Radiometer (SLSTR)

SLSTR is an instrument on the satellite Sentinel-3, and is designed for a global coverage of the surface temperature on Earth. This is not directly an ocean color instrument, but for different purposes we are interested in sea surface temperature(SST). From this sensor we can get level-2 data with estimation of temperature on land and sea, and in this project we are more interested in SST. SLSTR uses spectral bands in the short-wave infrared region to retrieve SST. [ESA, nd l]

Table 5.2: SLSTR band characteristics. (From [ESA, nd g])

Band	Central Wavelength (nm)	Bandwidth (nm)	Function
S1	554.27	19.26	Cloud screening, vegetation monitoring, aerosol
S2	659.47	19.25	NDVI, vegetation monitoring, aerosol
S3	868.00	20.60	NDVI, cloud flagging,Pixel co-registration
S4	1374.80	20.80	Cirrus detection over land
S5	1613.40	60.68	loud clearing, ice, snow,vegetation monitoring
S6	2255.70	50.15	Vegetation state and cloud clearing
S7	3742.00	398.00	SST, LST, Active fire
S8	10854.00	776.00	SST, LST, Active fire
S9	12022.50	905.00	SST, LST
F1	3742.00	398.00	Active fire
F2	10854.00	776.00	Active fire

5.4 Radar Imaging Systems

The microwave electromagnetic spectrum extends from wavelengths of approximatley 1 μm to 1 m. The most commonly used systems for radar imaging are active systems. These systems are not dependent on illumination from the sun. Active systems transmit energy themselves and collect the backscattered energy that is emitted from the ground. One major difference in ocean remote sensing is that optical imaging systems are able to sense a few meters below the ocean surface, while radar imaging systems are not. As mentioned in the introduction, the main objective of this thesis is to invesigate if there is a correlation between ocean color and SST images against SAR images. We wish to see if patterns in ocean color or sst images, can be seen in SAR images. If patterns in the ocean color images are below the surface, these will not appear in the SAR images.

On the other hand, if the patterns in the ocean color images lay on the surface, they should appear if the patterns are controlled by wind stress and currents. [Martin, 2014, Campbell, 2011, Henderson, 1998]

5.4.1 Coastal Dynamics

Mapping and monitoring of coastal dynamics from satellite sensors include the use of different instruments and sensors to get the data we needs. One need a combination of optical data from passive sensing and radar data from active sensing.

5.4.2 Sentinel-1

The Sentinel-1 satellite is a constellation of two satellites Sentinel-1A and Sentinel-1B. Sentinel-1A launched in April 2014 and Sentinel-1B launched in April 2016. The prime objective of this satellite is to provide C-Band SAR data for land and ocean monitoring. [ESA, nd i]

Sentinel-1 has a sun-synchronous orbit type with orbit height 693 km above ground. Its repeat cycle is 175 orbits in 12 days. The satellite's has only one instrument aboard; the C-Band Synthetic Aperture Radar(C-SAR) instrument. The C-SAR uses wavelengths of 7.5-3.75 cm. The satellites main objectives are land monitoring of forest and soil, marine monitoring, sea ice observations, mapping of oil spills, and climate change monitoring. [ESA, nd i]

5.4.3 C-Band Synthetic Aperture Radar(C-SAR)

To manage good monitoring of land and sea, Sentinel-1 carries a C-SAR sensor that offers, in all weather conditions, medium and high resolution images. The satellite is very useful for land and ocean monitoring because it detects small movements on the ground, as well as it takes night imagery. [ESA, nd i]

The C-Band Synthetic Aperture Radar instrument has four resolution and Swath widths; Strip Map Mode: 80 km Swath and 5x5 m spatial resolution,

Interferometric Wide Swath: 250 km Swath and 5x20 m spatial resolution, Extra-Wide Swath Mode: 400 km Swath and 25x100 m spatial resolution, and last Wave-Mode: 20x20 km Swath and 5x20 m spatial resolution. [ESA, nd i]

Part II

Data Analysis

6 Method

This chapter presents where the data for this thesis are collected, as well as it introduces the software used for data processing and analysis. Thereafter, it continues by describing the design and setup of the data analysis.

6.1 Data

The ocean color data collected for this thesis are downloaded from EUMETSAT(European Organization for Meteorological Satellites)[1], which is an earth observation portal that originally was made for monitoring climate and weather. EUMETSAT is an intergovernmental organisation owned by 30 European countries.

From this portal it is possible to download Sentinel data. The ocean color data used in this thesis is collected by Sentinel-3 from the OLCI instrument, mentioned in Chapter 5, while SST data is collected from the SLSTR instrument. As mentioned earlier, these data are level-2 data, which means that they are

1. https://www.eumetsat.int/website/home/index.html

processed with algorithms to give the information we want.

In addition to ocean color data and sea surface temperature data, I got some SAR data containing intensity images(Normalized Radial Cross Section(NRCS)), Geophysical Doppler products and Radial Velocity data. These data have been downloaded from Copernicus Openn Access Hub[2] which provides a complete, free and open access to satellite data from the Sentinel satellites. Thereafter, the data have been ran through an algorithm giving out Geophysical Doppler product and Radial Velocity products. I have gathered this data from Senior Research Scientist, Harald Johnsen[3], at Norut(Northern Research Institute).

6.1.1 Data sets

In this project, I have searched for satellite images of the study area between May and July for year 2018. Using optical ocean color data, one is dependent on cloud free days, and in northern Norway this can be challenging. I managed to find 7 dates between May and July with few clouds over my area of interest.

For this project I am using three different data sets, for each date. The first data set consist of 4 ocean color parameters stored in images; two different chlorophyll images(CHL_{NN} and CHL_{OC4Me}), one total suspended matter image(TSM) and one color dissolved organic material image($CDOM$). Depending on the case of water, I will use either CHL_{NN} or CHL_{OC4Me}. The concentration of these parameters are stored in each image.

The second data set consists of a sea surface temperature image(SST). While the third data set consist of two SAR products; NRCS(Normalized Radar Cross Section) as intensity image and geophysical Doppler product. Table 6.1 gives an overview of the data sets.

2. https://scihub.copernicus.eu/
3. https://norut.no/en/employees/harald-johnsen

Table 6.1: Overview of the three data sets for this project. This table gives an overview of what satellites and sensors the different images are from, what time the images are taken and what resolution the images have.

Data Set	Satellite & Sensor	Product	Sub Area	Time	Resolution
1	Sentinel-3 OLCI	CHL	A	0944-0947	300 m
			B	1036-1039	
		TSM	A	0944-0947	300 m
			B	1036-1039	
		CDOM	A	0944-0947	300 m
			B	1036-1039	
2	Sentinel-3 SLSTR	SST	A	1855-2046	1 km
			B	1947-2128	
3	Sentinel-1 C-SAR	Intensity image	A	0528-0529	3.3 - 3.9 km
			B	1631-1632	
		Geophysical Doppler	A	0528-0529	3.3 - 3.9 km
			B	1631-1632	

6.1.2 Possible Sources of Error

Given the conditions of the experiment, some effects can not be avoided. These effects are possible sources of error.

- There is a time difference between the data from the different sensors. OLCI data is collected around noon, while the SLSTR data is collected around nine hours after the OLCI data, and SAR products are from both early morning and dinner time. This can have an effect on the result when comparing data from different sensors.

- There is also a difference in resolution between the data from the different sensors. OLCI data have a resolution of 300 m, while SST and the SAT products have a resolution of 1 km. To be able to compare the images, an interpolation method has been used to resample the data after Ocean Color data from the OLCI satellite.

6.2 Data Pre-Processing

The software used for all of the pre-processing and analysis programming is Matlab[4], which is a mathematical programming tool. The software used for looking at the Sentinel images is SNAP(Sentinel Application Platform) [ESA, nd m]. This is a good tool to use to look at Sentinel images, since they have specially designed color scales for each of the parameters.

6.2.1 Image Interpolation Methods

Image interpolation is often necessary before analysing images against each other, since the resolution between two images can be very different. The data used in this thesis have different resolutions; OLCI have a resolution of 300 m, SLSTR of 1 km and SAR products of around 1 km. In this case I chose to use the level-2 image from the OLCI sensor as my master, and use the level-2 image from SLSTR sensor and the SAR products as my slaves. To resample the images, one needs to choose what type of image interpolation method one wants for the output.

Choosing an interpolation method can be difficult. They all have different pros and cons, some better that others. Depending on which interpolation method one chooses, the output will be slightly different. Some methods have a longer processing time while others give an output with higher quality. For these operations I chose to use Nearest Neighbour interpolation resampling. This is a very common interpolation method. It has a quick processing time, it is simple and at the same time gives an okay output. [Gu and Zhang, 2011]

4. https://se.mathworks.com/

6.3 Set Up of the Statistical Analysis

This data analysis will be divided into four cases. In the first case, data set one will be used. I will test four different statistical analysis approaches and investigate if these approaches gives an idea of the relationship between the ocean color parameters in data set one. In the second case, data set one and two will be used. I will test the same four statistical analysis approaches as for case one, to see if these approaches can give an idea of the relationship between ocean color parameters in data set one and sea surface temperature(SST) in data set two. Figure 6.2 shows the set up of the statistical analysis of case one and two.

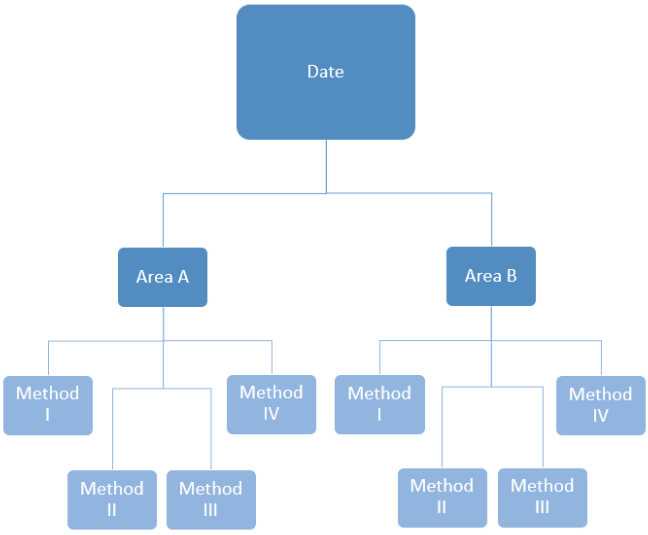

Figure 6.1: Set up of statistical analysis for case 1 and Case 2.

As we can see from Figure 6.2, for each date I choose different sub areas(in 6.2 for example, there are two sub areas A and B) that I wish to investigate further. These areas should be as cloud free as possible, and contain features of coastal dynamics such as Eddies or interesting patterns. Some sub areas near land have also been chosen. Thereafter, for each of the sub areas I have applied four different statistical analysis approaches or methods. The main objective is to find the approach that shows the best relation between the data, and the approach that can tell us anything about the relation of the coastal

dynamics.

For case three and four, I will for each date use one statistical analysis approach on the different sub areas. In case three, data set one and three will be used. I will investigate if there are any correlations between CHL in data set one and SAR products in data set three. In case four, data set two and three will be used. I will investigete if there are any correlations between SST in data set two and SAR products in data set three.

6.4 Statistical Analysis

As mentioned, to study the relation between the different parameters described above, I will use four different statistical analysis approaches. I have chosen to test these different approaches or methods:

6.4.1 Image Subtraction

By using image subtraction between two images, one takes the pixel value in one image and subtracts it from the same pixel in the other image. This method is very quick and simple, and will detect changes between the two images containing parameters. The formula can be described like this

$$D = |\overline{A} - \overline{B}| \tag{6.1}$$

where D is the resulting image subtraction between the two normalized images $\overline{A}$ and $\overline{B}$.

6.4.2 Regression

Regression is an approach where the objective is to investigate how sufficient a set of predictor variables manage to predict (dependent) outcome variables. In this thesis I am interested in the relation between two parameters(images), therefore I use a set of randomly chosen test data from each image to make a

model which describes the relationship between the predictor variables and the response variables. Afterwards I will run the model on all the data, and determine how well the model predicts the outcome parameter by calculating bias, R squared and Normalized Root Mean Squared Error(NRMSE):

$$Bias = \frac{1}{N}\sum_{i=1}^{N}|(y_i - \hat{y_i})| \tag{6.2}$$

$$R^2 = \frac{\sum_{i=1}^{N}(\hat{y_i} - \overline{y})^2}{\sum_{i=1}^{N}(y_i - \overline{y})^2} \tag{6.3}$$

$$NRMSE = \frac{1}{y_{max} - y_{min}}\sqrt{\frac{1}{N}\sum_{i=1}^{N}(y_i - \hat{y_i})^2} \tag{6.4}$$

where y is the actual data, $\hat{y}$ is the predicted data, y_{max} and y_{min} are the maximum and minimum observed value of y, $\overline{y}$ is the mean of the actual data, and N is the number of observations. A goodness of fit table with values of Bias, R^2 and NRMSE will tell how good the model is. [Blix et al., 2018]

A resulting image showing the difference between the predicted data versus the actual data will also visually show how well the regression model functions.

To derive the different regression models, I will use the Regression Learner app in Matlab. I use 5000 random pixels from each parameter image as training data, and fit the model with all of the pixels in the image.

Linear Regression Model

A linear regression model will give us a model that describes the linear relationship between two sets of variables. The model will describe a relationship

between a dependent variable, y, and an independent variable, $x_1, ..., x_n$, described with equation

$$y = \beta_0 + \beta_1 x + \varepsilon \tag{6.5}$$

where β_0 is the y-intercept, β_1 is the regression coefficient and ε is the term of error. [MathWorks, nd b]

Support Vector Machine(SVM) Regression Model

A Support Vector Machine regression can give us both a linear and a nonlinear model to describe the relationship between two sets of variables. I have chosen to use a nonlinear SVM regression approach that uses a Gaussian kernel function. The goal using this method is to obtain a function $f(x)$ that deviates from observed response values y_n by a value that is smaller than ε for all training points x. A nonlinear SVM finds the coefficients that minimize equation [MathWorks, nd c]

$$L(\alpha) = \frac{1}{2}\sum_{1=1}^{N}\sum_{j=1}^{N}(\alpha_i - \alpha_i^*)(\alpha_j - \alpha_j^*)G(x_i, x_j) + \varepsilon\sum_{i=1}^{N}(\alpha_i + \alpha_i^*) - \sum_{i=1}^{N} y_i(\alpha_i - \alpha_i^*) \tag{6.6}$$

subject to

$$\sum_{n=1}^{N}(\alpha_n - \alpha_n^*) \tag{6.7}$$

$$\forall n : 0 \leq \alpha_n \leq C \tag{6.8}$$

$$\forall n : 0 \leq \alpha_n^* \leq C \tag{6.9}$$

where α_n and α_n^* are nonnegative multipliers for each observation x_n, $G(x_i, x_j)$ is the Gram matrix and ε is the term of error. Since I have chosen to use a

Gaussian kernal, the Gram matrix looks like this:

$$G(x_i, x_j) = exp(- \parallel x_j - x_k \parallel^2) \tag{6.10}$$

To predict the new values this function is used

$$f(x) = \sum_{n=1}^{N} (\alpha_n - \alpha_n^*) G(x_n, x) + b \tag{6.11}$$

To obtain optimal solutions the formula requires optimization constrains; Karush-Kuhn-Tucker(KKT) complementary conditions. These are

$$\forall n : \alpha_n(\varepsilon + \xi_n - y_n + f(X_n)) = 0 \tag{6.12}$$

$$\forall n : \alpha_n^*(\varepsilon + \xi_n^* + y_n - f(X_n)) = 0 \tag{6.13}$$

$$\forall n : \xi_n(C - \alpha_n) = 0 \tag{6.14}$$

$$\forall n : \xi_n^*(C - \alpha_n^*) = 0 \tag{6.15}$$

where ξ_n and ξ_n^* are slack variables, and C is the box constraint. [MathWorks, nd c]

6.4.3 Correlation

The correlation coefficient between two images, let's say A and B, can be calculated with this formula

$$r = \frac{\sum_m \sum_n (A_{mn} - \overline{A})(B_{mn} - \overline{B})}{\sqrt{\left(\sum_m \sum_n (A_{mn} - \overline{A})\right)^2 \left(\sum_m \sum_n (B_{mn} - \overline{B})\right)^2}} \tag{6.16}$$

where $\overline{A}$ and $\overline{B}$ is the mean of the matrices A and B. [MathWorks, nd a]

The correlation coefficient of two matrices, or images, is a scalar. To get a resulting image showing the correlation coefficients, one can implement a loop with two sliding windows of size MxN pixels, let's say 9x9, that slides over the two images A and B and calculates the correlation coefficient within MxN. This loop slides over both images, collecting scalar values and stores them in a new

matrix, giving a resulting matrix that can be displayed as a correlation image of A and B, holding the information of how the images correlate.

Deriving the correlation coefficient, one assumes a linear relationship between the two images A and B. In other words, one assumes that a change in A involves a certain constant change in the corresponding average value of B. The correlation coefficient does never exceed $[-1, 1]$, where $+1$ gives a perfect correlation, 0 gives no correlation, and -1 gives a perfect negative correlation. Easily explained, the correlation between two variables tells us something about the underlying dependency between the variables - how much they connect with each other. [Wright, 1921]

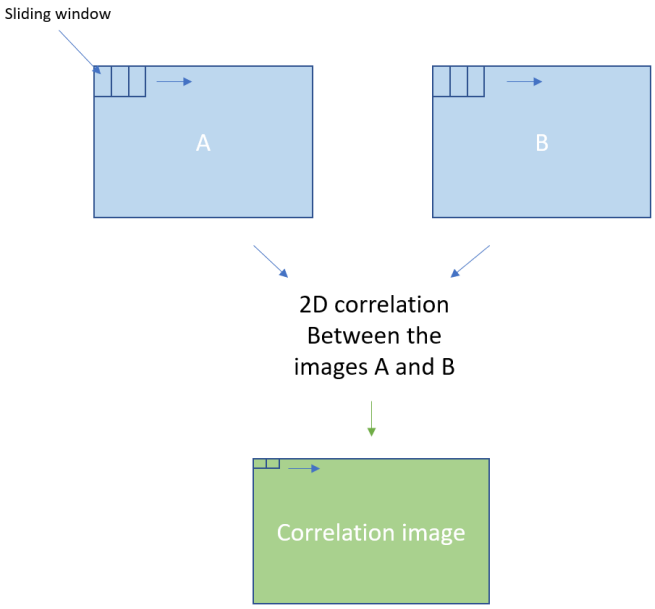

Figure 6.2: The correlation method.

7

Results and Discussion

This chapter will present the results and discussion of four different test cases. I will only present the results from two dates, with one sub area for each date, since the trends among my results are almost the same and the result of all of the sub areas from all of the dates will occupy many pages. Therefore, I will present the results from 10th of May and 28th of July.

7.0.1 Sub Areas

Figure 7.1 and 7.2 presents roughly the different sub areas chosen as different study areas for the two dates I am presenting results from. I choose to show the results for one sub area per date. But these images gives an idea on the different sub areas I have investigated in this project.

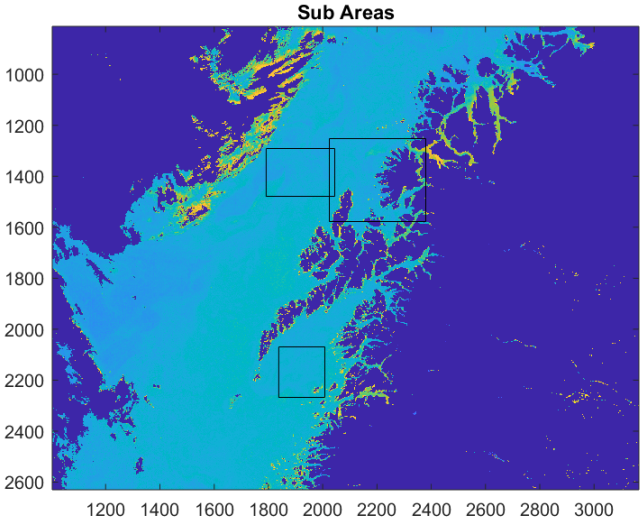

Figure 7.1: Sub areas, 2018.05.10.

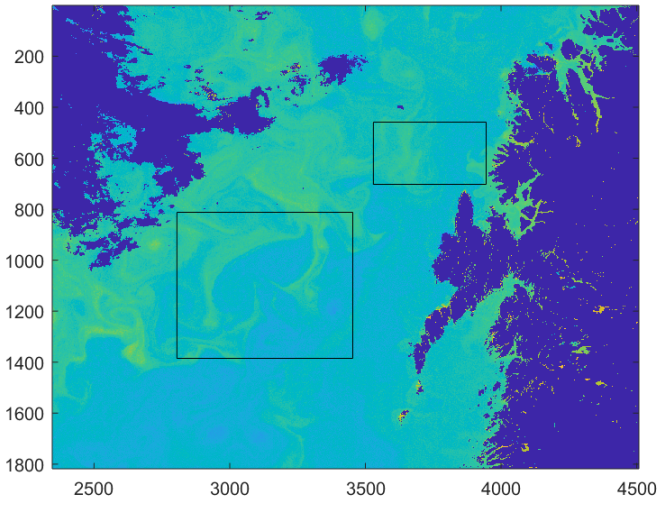

Figure 7.2: Sub areas, 2018.07.28.

The SAR data scenes can be seen in Figure 7.3.

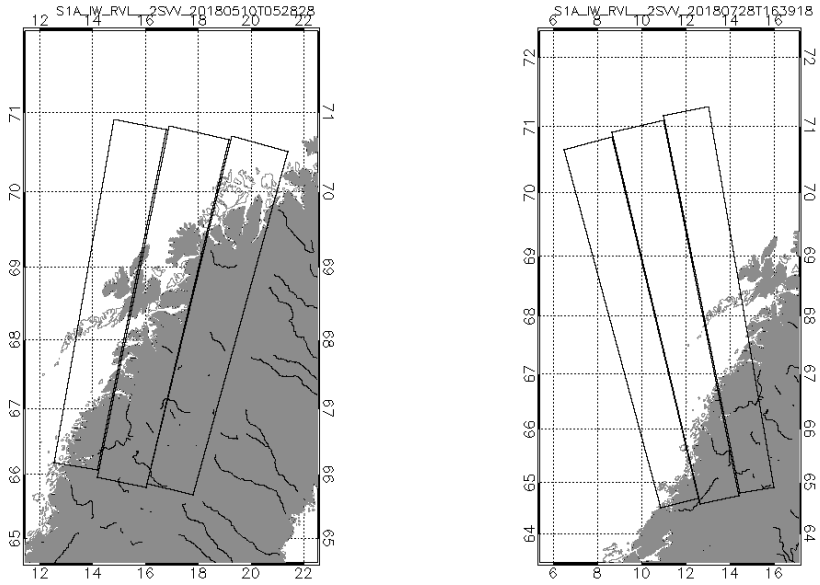

(a) 2018.05.10 **(b)** 2018.07.28

Figure 7.3: SAR scenes. (From Harald Johnsen, Norut)

7.0.2 Parameters

The following Figures shows the different parameter images in each data set for the two dates and study areas chosen two show the results for, 10th of May and 28th of July 2018. Since these two sub areas are not by the coast, the OC4Me algorithm for chlorophyll concentration is used. Sub area A is the area in the top left rectangle in Figure 7.1, and sub area B is the area in the biggest rectangle in Figure 7.2.

Sub Area A

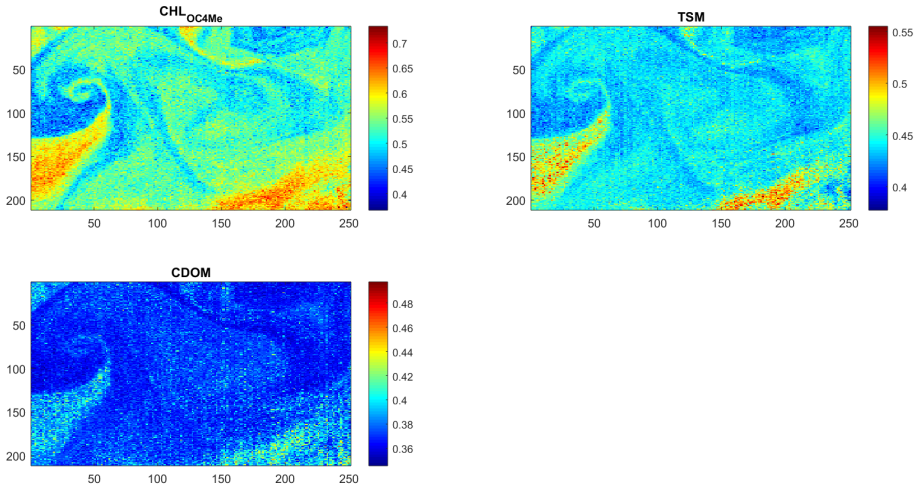

Figure 7.4: Parameter images for data set 1, 2018.05.10. (Normalized data.)

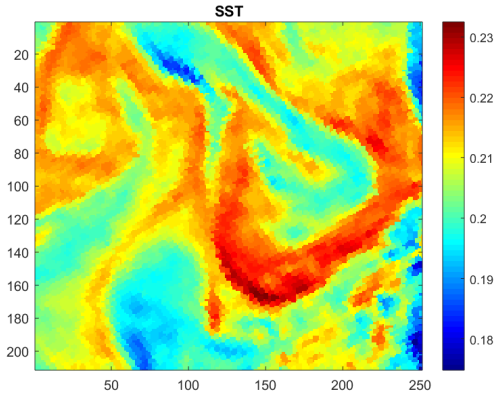

Figure 7.5: Parameter image for data set 2, 2018.05.10. (Normalized data.)

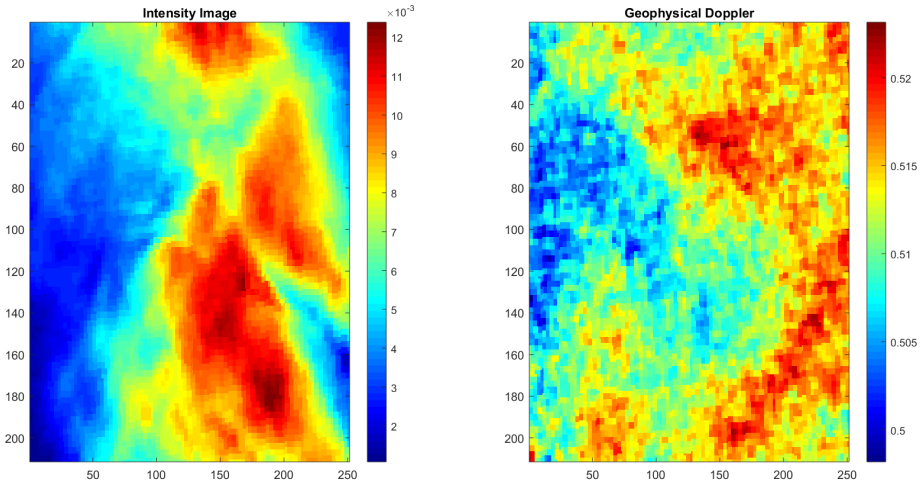

Figure 7.6: Parameter image for data set 3, 2018.05.10.

Sub Area B

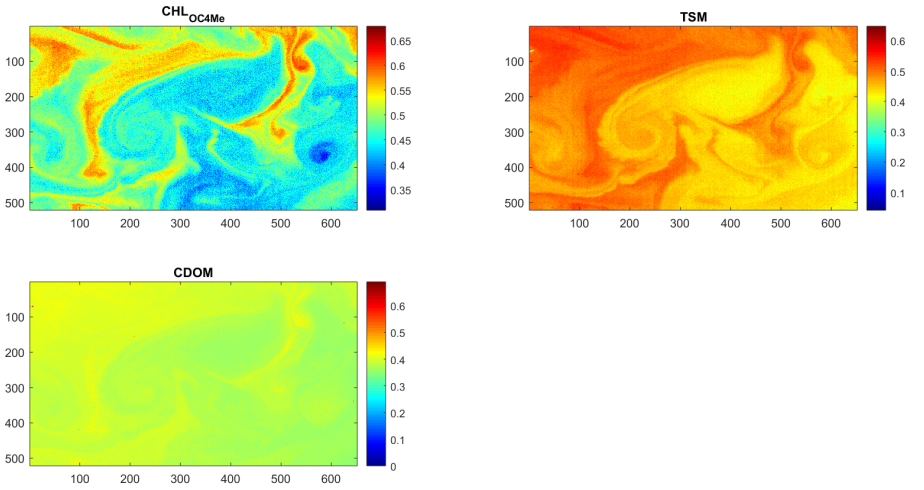

Figure 7.7: Parameter images data set 1, 2018.07.28. (Normalized data.)

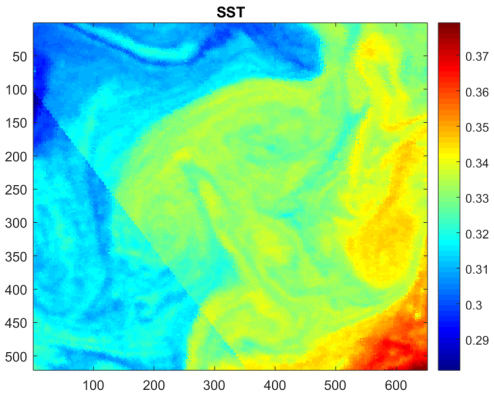

Figure 7.8: Parameter image for data set 2, 2018.07.28. (Normalized data.)

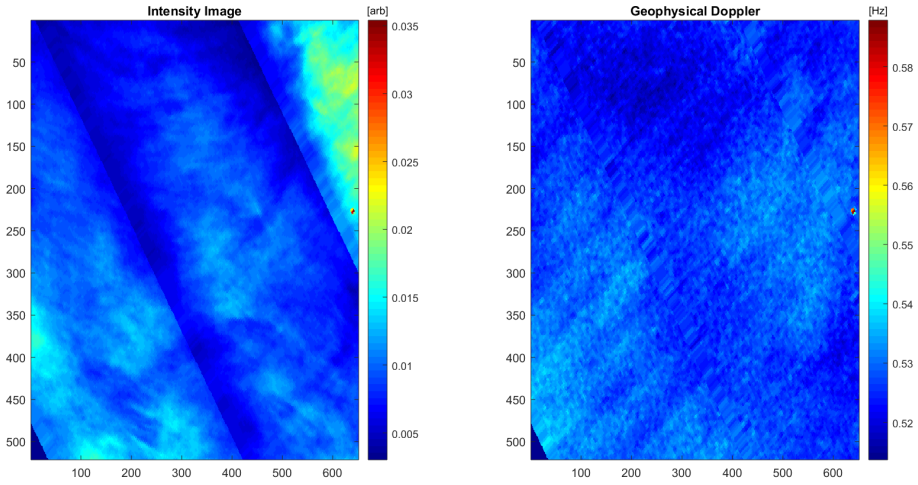

Figure 7.9: Parameter images for data set 3, 2018.07.28.

By observing the ocean color parameters from data set one in Figure 7.4 and 7.7, and the SST images in Figure 7.5 and 7.8, we can clearly see some of the same patterns in the images - especially between CHL, TSM and CDOM. Also, we can observe some of the patterns in the SST images, but not as clearly as between CHL, TSM and CDOM (the three OLCI parameters). For example in Figure 7.4, we can observe the Eddie stream to the left in the CHL, TSM and CDOM images. We can also see some of that "Eddie path" in the SST image in Figure 7.5. The clear light blue path in the SST image just to the right of the

centre of the image, can also be seen in the parameter images. In Figure 7.7, we can clearly see the oval shape of a whale in the middle of the CHL, TSM and CDOM images. This pattern can also be seen in the SST image in Figure 7.8, but it does not stand out as much as in the other images.

From the parameter images, we can also observe that areas containing high amounts of CHL also contain high amounts of TSM and CDOM. Given this, and the pattern they together form in the ocean, this is probably caused by coastal dynamics in the area. If we look at the SST image in Figure 7.8 we can see that in the top left corner of the SST image, we can see that there are lower temperatures compared to other areas in the sub-image. These areas with lower temperature also correspond with the high concentration of chlorophyll in the CHL image in Figure 7.7. This corresponds with the literature discussed earlier in chapter 2 and 4 in the thesis. That colder nutrition rich water often helps in the production of phytoplankton. In the areas where there are the lowest concentration of CHL, there are also warmer waters in the SST image.

By observing the parameters in Figure 7.6 and 7.9 we can see that the patterns in the parameter images in Figure 7.4 and 7.7 are not sticking out in the SAR product images. If we look at the intensity image in Figure 7.6, with Figure 7.4 in mind, we can see that where we have the Eddie pattern in the parameter images in Figure 7.4, we can see something happening in the intensity image in Figure 7.6. The triangle Eddie path we can spot in Figure 7.4 and the SST image, we can see hints of in the intensity image in Figure 7.6. If we look at the geophysical Doppler image, we can see some similarities with the intensity image. We can see the dark area to the left in the intensity image corresponding to the blue area to the left in the geophysical Doppler image.

If we look at the parameter images for sub area B in Figure 7.7 and the SAR products in Figure 7.9, we can actually see hints of the whale shaped pattern that can be seen in the parameter images in Figure 7.7, in the intensity image. Down in the left corner area in the geophysical Doppler image we can see a bit lower Doppler values. In the same area in the ocean color parameter images, we have moderate to high concentrations of CHL, TSM and CDOM. As mentioned in the introductory chapter and in chapter 3, the intensity images are sensitive to changes in surface when it comes to wind and waves. While

geophysical Doppler is a measure of the velocity in the in line of sight direction. Looking at the Geophysical Doppler images we can see some similarities with the intensity images. If we look to the left in the geophysical Doppler image in Figure 7.6, we can see low values that correspond with low values in the intensity image. We can also see the red spot on the top of the intensity image, corresponding with the green area in the top of the geophysical Doppler image. In Figure 7.9 we can see that the middle area in both images correspond with each other. Also the light blue area towards the left lower corner in both images. Except these examples, there are not many more similar features.

7.1 Case 1

In this case, I have investigated, with the four different statistical analysis approaches described in Chapter 6, the relationship between the ocean color parameters in data set one. The parameter images from data set one can be seen in Figure 7.4 for the 10th of May, and in Figure 7.7 for the 28th of July.

Method I: Image Subtraction Figure 7.10 for sub area A and Figure 7.11 for sub area B, shows the results of the image subtraction method for different combinations of ocean color parameters.

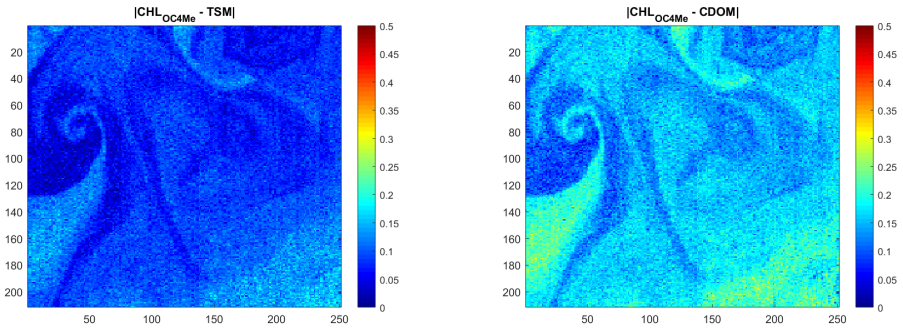

(a) CHL-TSM **(b)** CHL-CDOM

(c) TSM-CDOM

Figure 7.10: Result images from the image subtraction method, sub area A

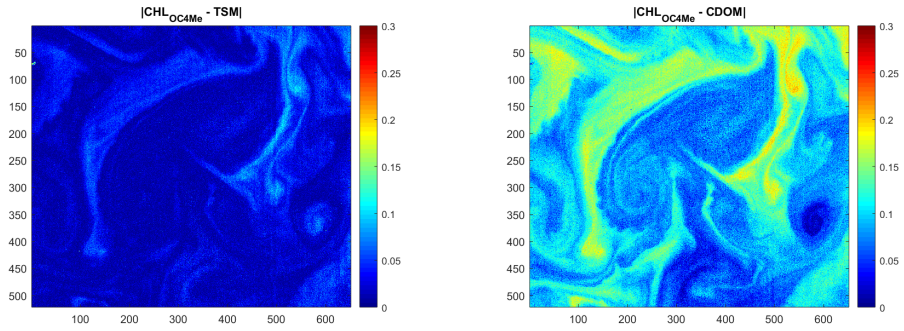

(a) CHL-TSM **(b)** CHL-CDOM

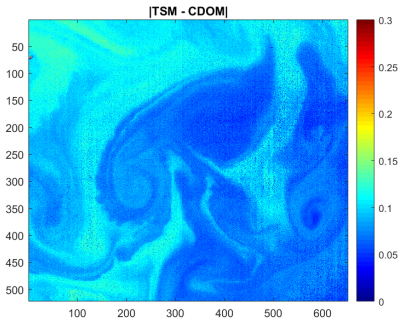

(c) TSM-CDOM

Figure 7.11: Result images from the image subtraction method, sub area B.

The image subtraction method is a very quick and easy method to detect differences between pixels in two images. In Figure 7.10 and 7.11 we can see the results of the image subtraction between ocean color parameters in sub area A and B, respectively. The parameters have been normalized before taking the image subtraction. The range on the colorbars are $[0, 0.5]$. These images tells us if the original images are much alike. The lower values, the more alike are they. This method shows changes between images very easily. If we have the ocean color parameter images in Figure 7.4 and 7.7 in mind, we can see that the Eddie feature in sub area A and the whale shaped pattern in sub area B are visible in the resulting image subtracting images. From Figure 7.10, sub area A, we observe that CHL and TSM in (a) and that TSM and CDOM in (c) are very alike, meaning that there are not that many changes between the parameters CHL and TSM, and TSM and CDOM. From Figure 7.11, sub area B, we observe almost the same trends as in sub area A. We observe that CHL and

TSM in (a) and that TSM and CDOM in (c) are very alike. A few more changes between CHL and CDOM. Overall, it looks like the areas with the most changes between two parameters are in the same area for all combinations. This can also be observed in Figure 4.4, 4.6 and 4.5 in Chapter 4, where we can see the patterns. As well, we can see that areas with high amounts of CHL, there is also high amounts of TSM and CDOM.

All in all, there seems to be a clear trend if we look at the three parameters CHL, TSM and CDOM that are taken with the same instrument. It seems to be few significant changes between these parameters.

Method II: Linear Regression Figure 7.12 for sub area A and Figure 7.13 for sub area B, shows the resulting difference images between predicted and actual data.

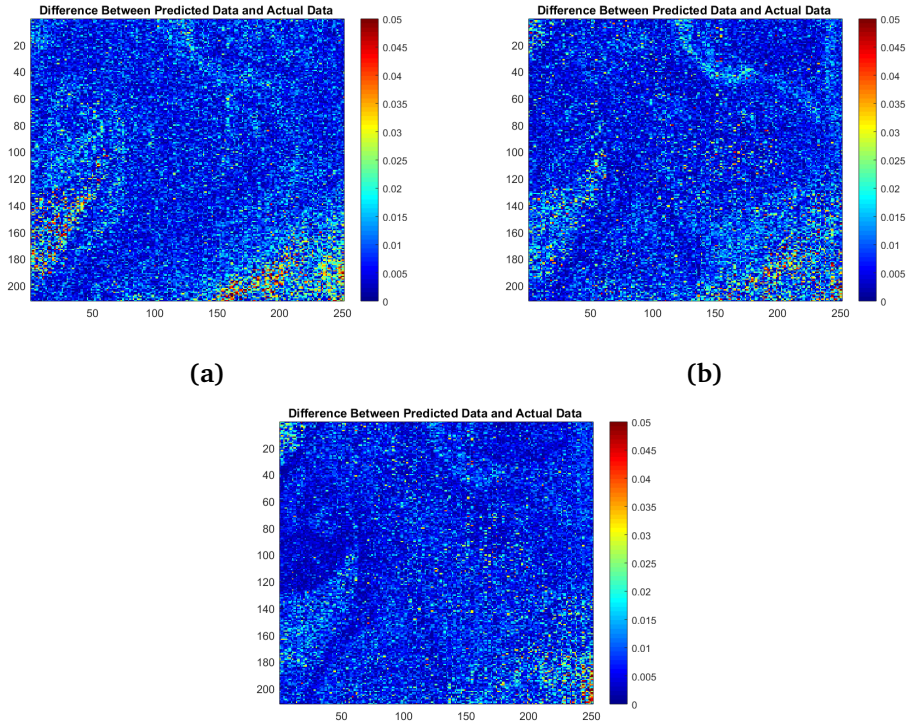

(a) **(b)**

(c)

Figure 7.12: Difference images between predicted and actual data, for the linear regression method, sub area A. (a) shows the difference image between the predicted TSM data based on CHL data, and actual TSM data. (b) shows the difference image between the predicted CDOM data based on CHL data, and the actual CDOM data. (c) shows the difference image between the predicted CDOM data based on TSM data, and the actual CDOM data.

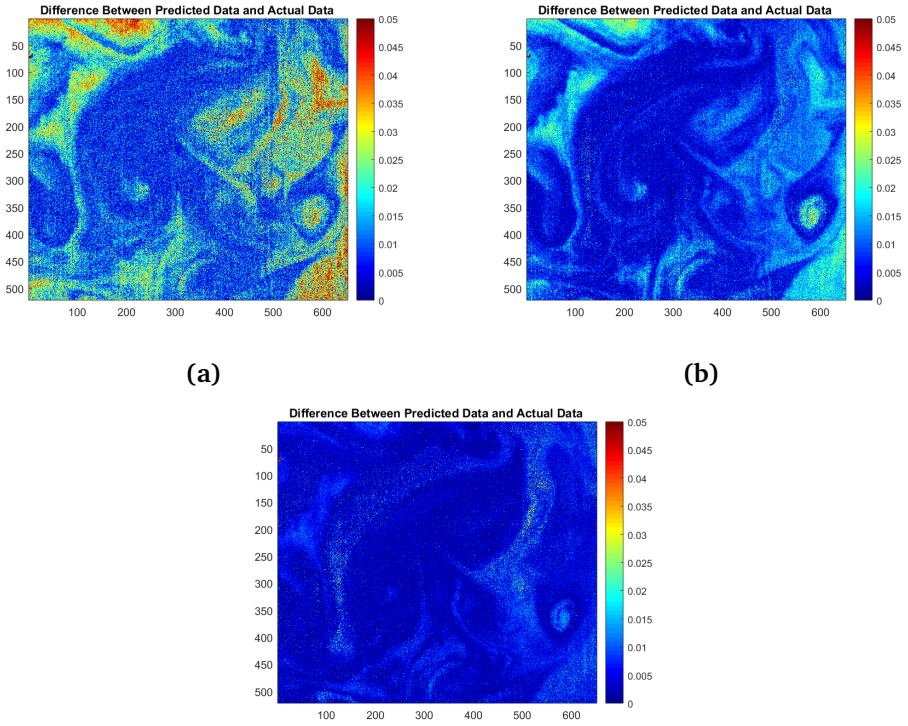

(a) **(b)**

(c)

Figure 7.13: Difference images between predicted and actual data, for the linear regression method, sub area B. (a) shows the difference image between the predicted TSM data based on CHL data, and the actual TSM data. (b) shows the difference image between the predicted CDOM data based on CHL data, and the actual CDOM data. (c) shows the difference image between the predicted CDOM data based on TSM data, and the actual CDOM data.

Table 7.1 shows the goodness of fit table for the linear regression models between ocean color parameters in sub area A, while Table 7.2 shows the goodness of fit table for the linear regression models between ocean color parameters in sub area B.

Figure	Bias	R^2	NRMSE
a	1.2989e-04	0.6057	0.0646
b	3.8017e-05	0.3900	0.0720
c	4.3331e-06	0.5334	0.0615

Table 7.1: Goodness of fit table for the linear regression models for the combinations of ocean color parameters, sub area A.

Figure	Bias	R^2	NRMSE
a	2.0766e-04	0.6928	0.0284
b	1.9716e-04	0.5492	0.0150
c	5.9614e-05	0.8486	0.0087

Table 7.2: Goodness of fit table for the linear regression models for the combinations of ocean color parameters, sub area B.

In the linear regression method we wish to check if there exists a linear regression model between two parameters, and how good this model is. Normalized data were also used here. The range of the colorbar is $[0, 0.05]$. In figure 7.12 we can see the difference images between the predicted data and actual data from sub area A. At first sight we can see that the difference images looks almost the same. In (a) we trained a linear regression model based on CHL and response values of TSM, to predict TSM values from CHL values. While in (b) we trained on CHL and CDOM to predict CDOM based on CHL, and in (c) we trained on TSM and CDOM to predict CDOM based on TSM. These three combinations of parameters gives a relatively high R^2. This can bee found in the goodness of fit table in Table 7.1. "R squared" tells us how much better the regression line is, compared to a horizontal line that goes through the mean of the data. Given the relatively high values of R^2 means that knowing the "x-value" actually helps with the prediction of the "y-value". From Table 7.1 we can see that the combinations in (a) and (c) have a relatively high R^2 and a low Bias and NRMSE.

The results of the linear regression method in sub area B can be seen in Figure 7.13. We can see that the difference image between predicted CDOM based

on TSM, and actual CDOM gives mostly low values. Meaning that the linear relationship is good. This can also be seen from the goodness of fit table in Table 7.2. We can also see that the linear model in (a) and (c) have high R^2, giving a good liner relationship between the ocean color parameters.

All in all, linear regression models gives clear trends with these combinations of ocean color parameters. Predicting an ocean color parameter based on another ocean color parameter with linear regression works well.

Method III: SVM regression Figure 7.14 for study area A and Figure 7.15 for study area B, shows the resulting difference images between predicted and actual data.

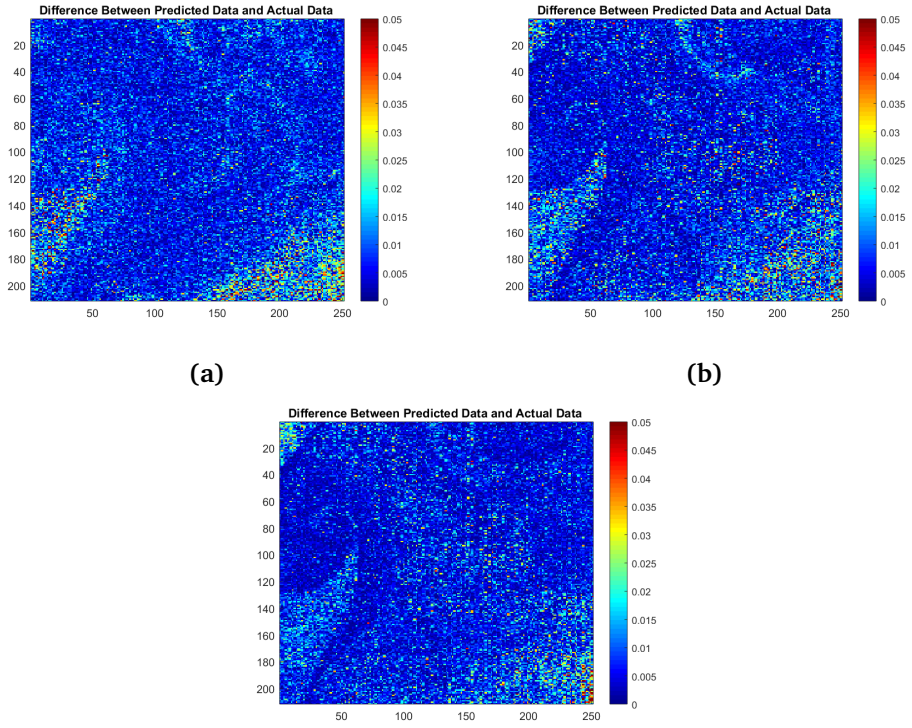

(a) **(b)**

(c)

Figure 7.14: Difference images between predicted and actual data, for the SVM regression method, sub area A. (a) shows the difference image between the predicted TSM data based on CHL data, and actual TSM data. (b) shows the difference image between the predicted CDOM data based on CHL data, and the actual CDOM data. (c) shows the difference image between the predicted CDOM data based on TSM data, and the actual CDOM data.

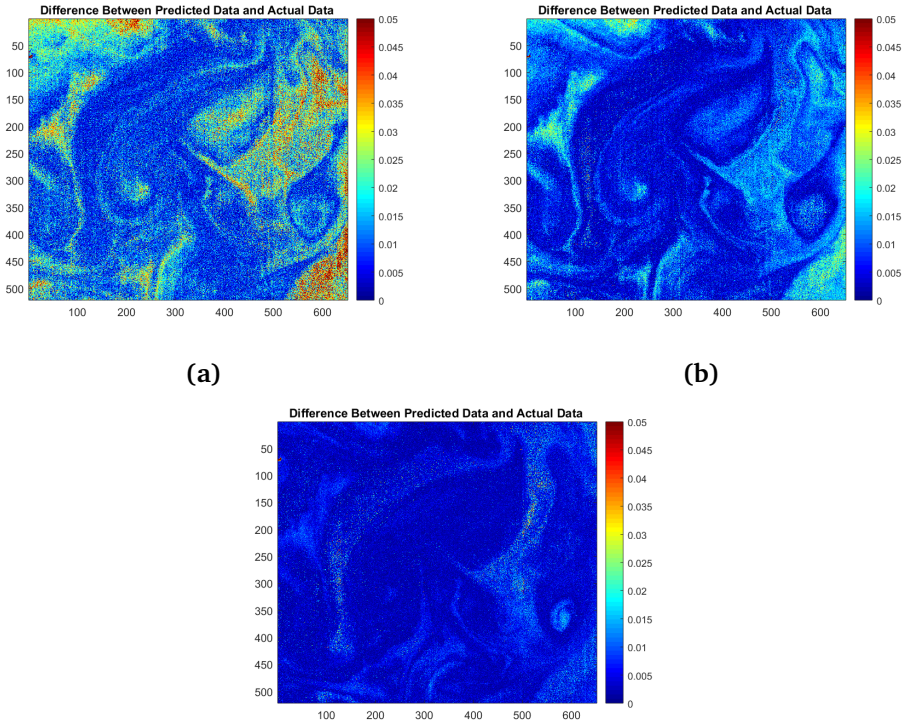

(a) **(b)**

(c)

Figure 7.15: Difference images between predicted and actual data, for the SVM regression method, sub area B. (a) shows the difference image between the predicted TSM data based on CHL data, and actual TSM data. (b) shows the difference image between the predicted CDOM data based on CHL data, and the actual CDOM data. (c) shows the difference image between the predicted CDOM data based on TSM data, and the actual CDOM data.

Table 7.3 shows the goodness of fit table for the SVM regression method for ocean color parameters in sub area A. Table 7.4 shows the goodness of fit table for the SVM regression method for ocean color parameters in sub area B.

Figure	Bias	R^2	NRMSE
a	4.3027e-04	0.5816	0.0610
b	0.0013	0.3763	0.0716
c	0.0020	0.5461	0.0621

Table 7.3: Goodness of fit table for the SVM regression models for the combinations of ocean color parameters, sub area A.

Figure	Bias	R^2	NRMSE
a	0.0011	0.7139	0.0274
b	4.3333e-05	0.5700	0.0146
c	6.0263e-05	0.8512	0.0086

Table 7.4: Goodness of fit table for the SVM regression models for the combinations of ocean color parameters, sub area B.

In the SVM regression method we wish to check if there exist a nonlinear regression model that can explain the relationship between combinations of parameters. Normalized data were also used here. The range of the colorbar is $[0, 0.05]$. In Figure 7.14 we can see the difference images between predicted and actual data from sub area A. At first sight, these difference images does not appear much different from the linear regression difference images in Figure 7.12. If we compare Table 7.1 and 7.3, there are not that big difference in values. The linear regression method provides a slightly better model for (b),CHL and CDOM, and (c),TSM and CDOM, while the SVM regression method provides slightly better models for the combination in (a), CHL and TSM.

The results of the SVM regression method in sub area B can be seen in Figure 7.15. At first sight, also these difference images between predicted and actual data look quite similar to the linear regression method difference images in Figure 7.13. If we compare the goodness of fit tables 7.2 and 7.4, there are not that big differences. But, here SVM regression models are slightly better than the linear regression models.

Overall, SVM regression models provides slightly better models compared to linear regression models. The best SVM models are provided for (a) CHL and

TSM in sub area A, and (c) TSM and CDOM in sub area B.

Method IV: Correlation Figure 7.16 for sub area A and Figure 7.25 for sub area B, shows the results of the correlation between different combinations of ocean color parameters.

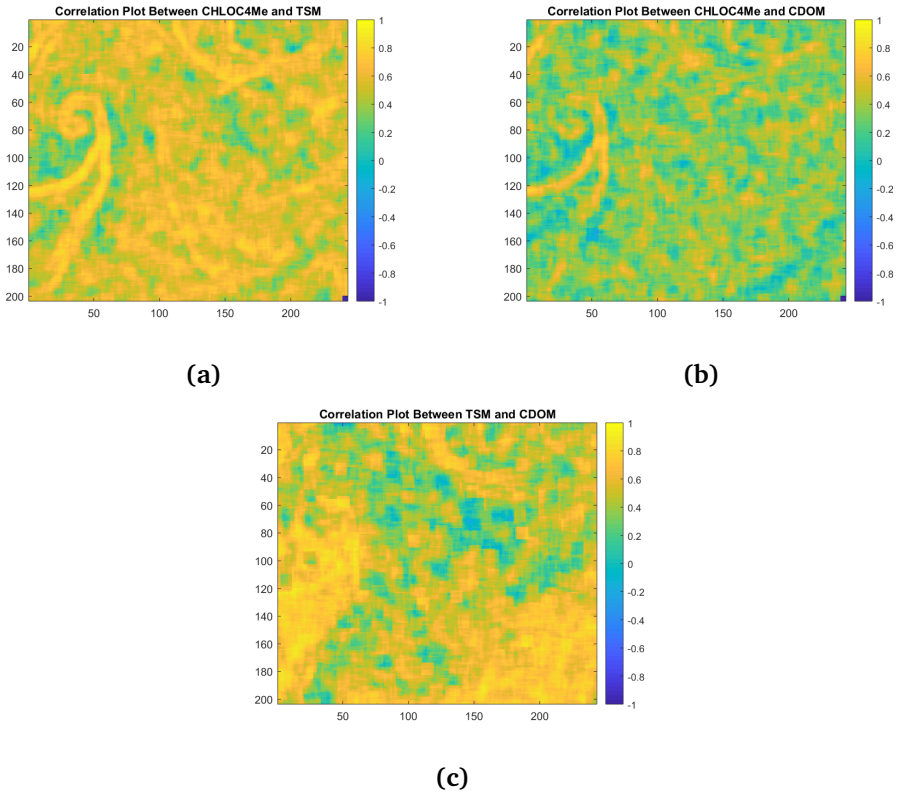

(a) **(b)**

(c)

Figure 7.16: Result images from the correlation method, sub area A. (a) shows the correlation between CHL and TSM. (b) shows the correlation between CHL and CDOM. (c) shows the correlation between TSM and CDOM.

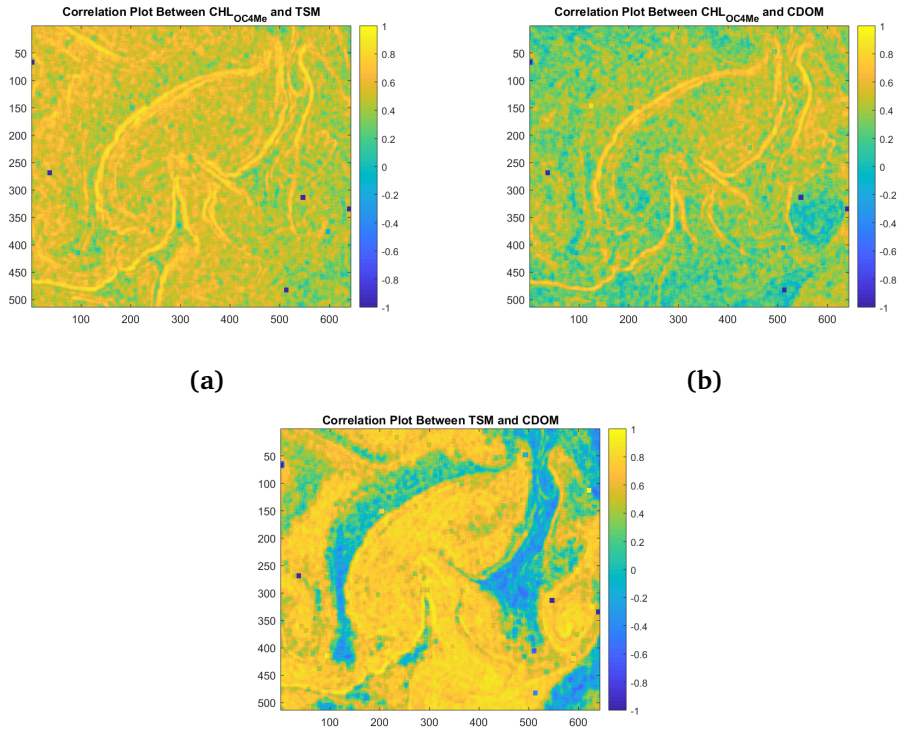

Figure 7.17: Result images from the correlation method, sub area B. (a) shows the correlation between CHL and TSM. (b) shows the correlation between CHL and CDOM. (c) shows the correlation between TSM and CDOM.

In the correlation method we wish to check the correlation between two parameters. This method uses a 9x9 pixels sliding window to perform a 2D correlation between two images. So, 9x9 pixels from two different images are compared at the same time. The resulting correlation coefficients are put into a new image. Normalized data are used, and the range of the colorbar is $[-1, 1]$, where -1 is a perfect negative correlation, 0 is no correlation and 1 is perfect correlation. The resulting correlation images for pairs of combinations between ocean color parameters in sub area A, can be seen in Figure 7.16.

Firstly, we observe many areas with high correlation(yellow areas). In all three images we can observe the Eddie path to the left in the images. We can see that the edges of the Eddie path sticks out with high correlation. Since we use

a sliding window of size 9x9 pixels, we take some of the neighbourhood into account when calculating the correlation, and not only checking pixel against pixel. The correlation images from sub area B can be seen in Figure 7.25. From these images we can clearly see that the combination of ocean color parameters have high correlation. We can clearly see the whale shaped pattern, and that the edges sticks out with high correlation.

All in all, we can see a clear trend in the correlation images. (c), TSM and CDOM, have most areas with high correlation. But, (a), CHL and TSM, and (c), CHL and CDOM, also have many areas with high correlation.

7.1.1 Summary Case 1

All of the statistical analysis approaches gives the same trend; there are definitely a relationship between ocean color parameters. This can be found from all methods. From the image subtraction method we found no big changes between any of the combinations of parameters. In the two regression methods we found slightly better nonlinear relationship between the combinations of parameters, using SVM regression models. In the correlation method we can clearly see the relationship between the parameters in the neighbourhood of each pixel, meaning that there definitely are relationships between the ocean color parameters.

7.2 Case 2

In this case, I have investigated, with the four different statistical analysis approaches described in Chapter 6, the relationship between the ocean color parameters in data set one and SST in data set two. The parameter images from data set one can be seen in Figure 7.4 and 7.7, and the parameter image for data set two can be seen in Figure 7.5 and 7.8.

Method I: Image Subtraction Figure 7.18 for sub area A and Figure 7.19 for sub area B, shows the results of the image subtraction method for different combinations of ocean color parameters and SST.

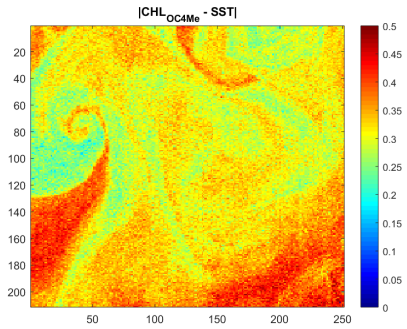

(a) CHL-SST

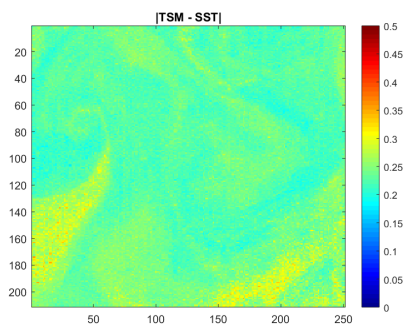

(b) TSM-SST

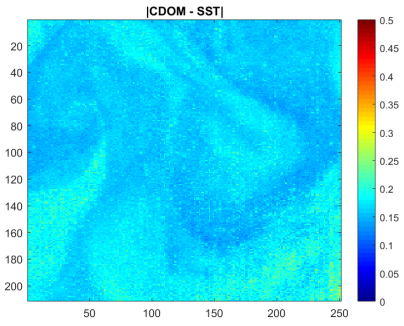

(c) CDOM-SST

Figure 7.18: Result images from the image subtraction method, sub area A.

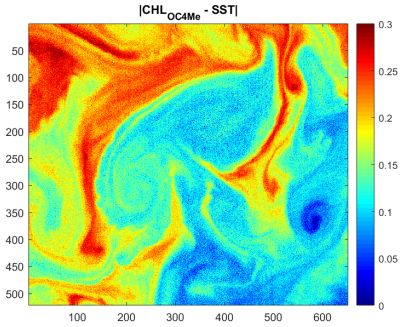

(a) CHL-SST

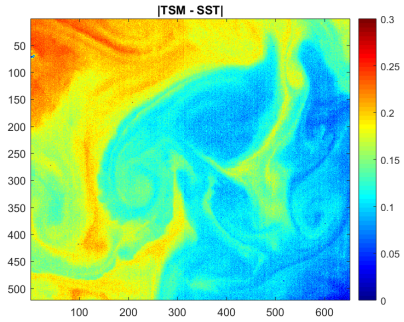

(b) TSM-SST

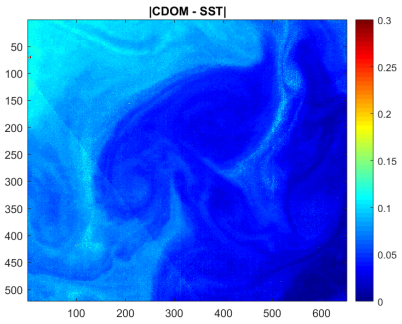

(c) CDOM-SST

Figure 7.19: Result images from the image subtraction method, sub area B.

From the resulting image subtraction images, from sub area A, in Figure 7.19 we can clearly see the same pattern and the Eddie feature as in the parameter images in 7.4 and 7.5. From Figure 7.19 we can observe that the changes between SST and an ocean color parameter are more significant that the changes between ocean color parameters. We can see that CHL and SST in (a) have greater changes between them, than TSM and SST in (b) and CDOM and SST in (c). The relationship between CDOM and SST in (c) is the best relationship with SST and another of the ocean color parameters.

From the introductory chapter and Chapter 2, we have that colder water often is more nutrition rich, and thus leads to a higher biological productivity, meaning higher concentrations of chlorophyll. This can be the reason for the high changes in (a) between CHL and SST in the top left area. Low values of SST and high values of CHL, will give high changes in the image subtraction image,

since it measures the change between normalized pixels. From (c) in Figure 7.19, we can see that between CDOM and SST, there are not that many changes. Meaning that the relationship between SST and CDOM is the best relationship including SST and an ocean color parameter.

Method II: Linear Regression Figure 7.20 for sub area A and Figure 7.21 for sub area B, shows the resulting difference images between predicted and actual data, between different combinations of ocean color parameters and SST.

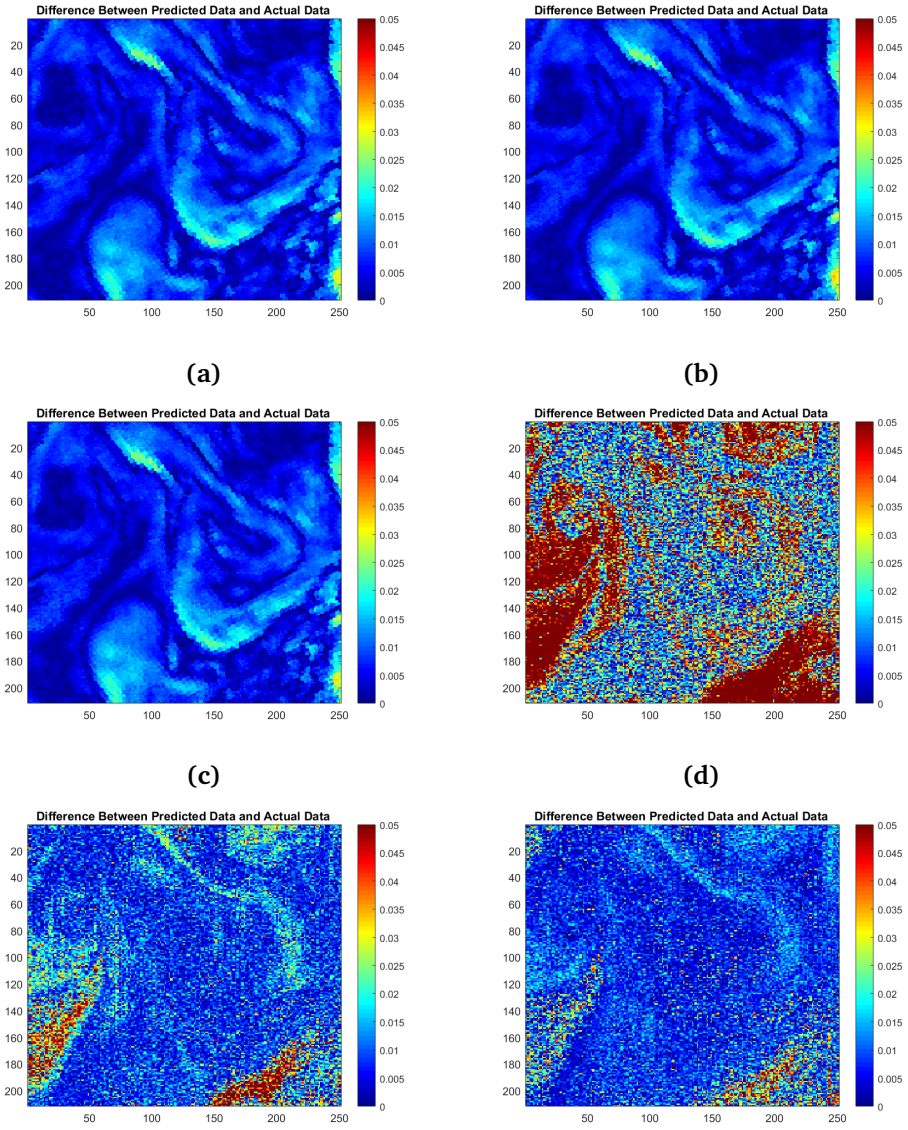

Figure 7.20: Difference images between predicted and actual data, for the linear regression method, sub area A. (a) shows the difference image between the predicted SST data based on CHL data, and actual SST data. (b) shows the difference image between the predicted SST data based on TSM data, and the actual SST data. (c) shows the difference image between the predicted SST data based on CDOM data, and the actual SST data. (d) shows the difference image between the predicted CHL data based on SST data, and the actual CHL data. (e) shows the difference image between the predicted TSM data based on SST data, and the actual TSM data. (f) shows the difference image between the predicted CDOM data based on SST data, and the actual CDOM data.

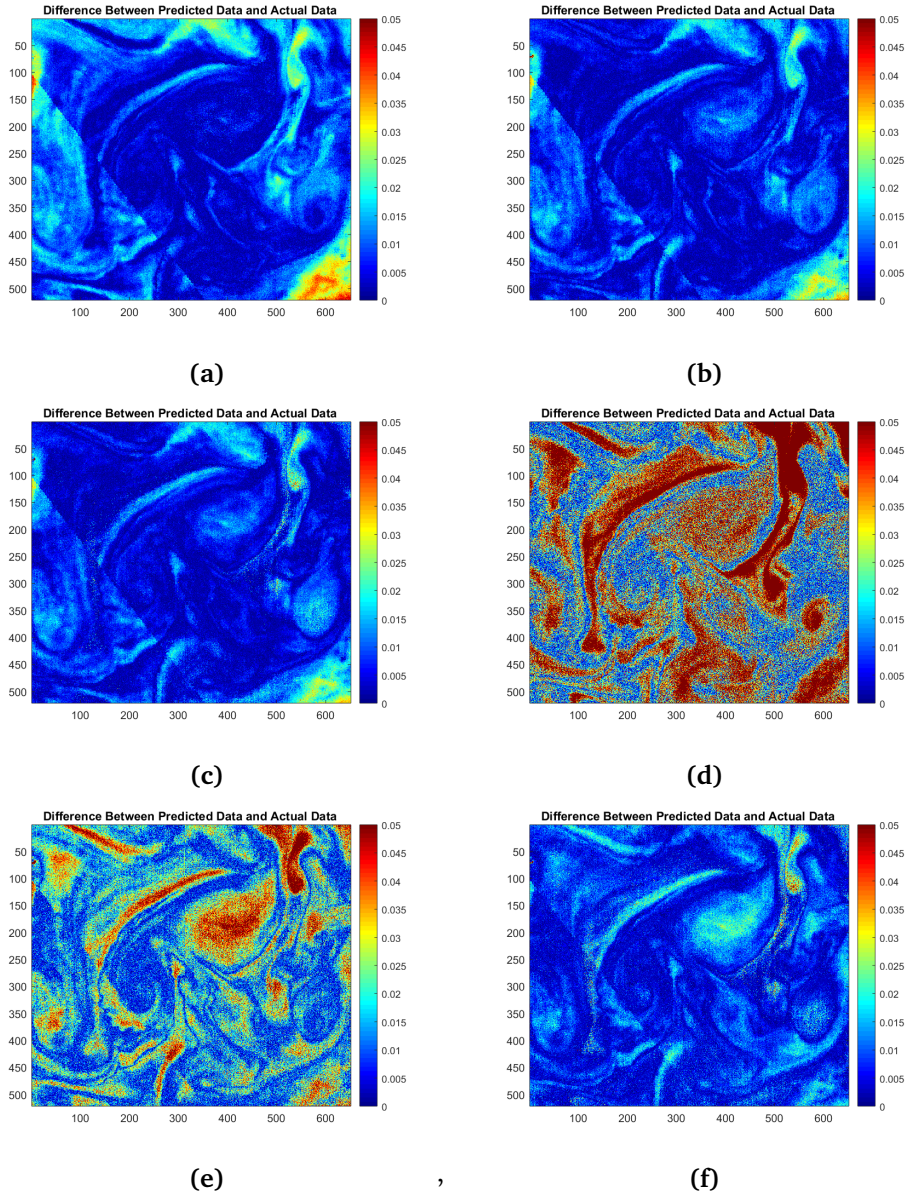

Figure 7.21: Difference images between predicted and actual data, for the linear regression method, sub area B. (a) shows the difference image between the predicted SST data based on CHL data, and the actual SST data. (b) shows the difference image between the predicted SST data based on TSM data, and the actual SST data. (c) shows the difference image between the predicted SST data based on CDOM data, and the actual SST data. (d) shows the difference image between the predicted CHL data based on SST data, and the actual CHL data. (e) shows the difference image between the predicted TSM data based on SST data, and the actual TSM data. (f) shows the difference image between the predicted CDOM data based on SST data, and the actual CDOM data.

Table 7.5 shows the goodness of fit table for the linear regression method between SST and ocean color parameters in sub area A. While Table 7.5 shows the goodness of fit table for the linear regression method between SST and ocean color parameters in sub area B.

Figure	Bias	R^2	NRMSE
a	3.9358e-05	0.0404	0.1437
b	4.1456e-05	0.0151	0.1440
c	2.6775e-05	0.0212	0.1434
d	1.5298e-04	0.0286	0.0586
e	2.9118e-04	0.0210	0.0979
f	1.8267e-04	0.0247	0.0893

Table 7.5: Goodness of fit table for the linear regression models for the combinations of SST and ocean color parameters, sub area A.

Figure	Bias	R^2	NRMSE
a	3.0403e-04	0.2540	0.1124
b	5.3084e-05	0.5255	0.0897
c	2.9478e-05	0.5596	0.0864
d	3.8095e-04	0.2580	0.0594
e	4.6722e-05	0.5317	0.0351
f	6.2553e-05	0.5629	0.0147

Table 7.6: Goodness of fit table for the linear regression models for the combinations of SST and ocean color parameters, sub area B.

In Figure 7.20 and 7.21 we can see the difference images between predicted and actual data, for the linear regression method for area A and B, respectively. At first sight, from Figure 7.20 we can see that (a), (b) and (c) looks very similar. First of all, we can see the same patterns as in the SST image in Figure 7.5. We can also see some of the Eddie path, discussed earlier. In the dark blue areas the linear model is good. These dark areas are the same in these three images. In (d), (e) and (f) we can see that the actual data are further from the predicted data. These areas can be seen especially in the Eddie path area and down in the right corner of the images. For the combination of SST and

ocean color parameters, Table 7.5 gives very low values of R^2 and relatively high values of NRMSE. This means that linear regression models between SST and ocean color parameters in sub area A are bad.

In Figure 7.21 we can see some of the trends as in Figure 7.20, by looking at the images. The three first images gives okay relationships. Looking at the last three difference images, (d), (e) and (f) for both sub area A and B, we can see the difference images from the predicted of CHL, TSM and CDOM respectively, based on SST-values. For sub are A, these models gives not that good values in the goodness of fit table in Table 7.1, but for sub area B, these models gives bad and okay models. Sub area A gives clearly worse R^2s compared to sub area B.

Overall, a linear regression model between SST and ocean color parameter does not provide a sufficient models. Meaning that the relation between SST and ocean color parameters are not sufficient, at least not for sub area A. The relationships between SST and ocean color parameters in sub area B are slightly better, but not good. CDOM is the ocean color parameter that have the best relation with SST, and predicting CHL based on SST, does not give a good liner model.

Method III: SVM regression Figure 7.22 for study area A and Figure 7.23 for study area B, shows the resulting difference images between predicted and actual data, between different combinations of ocean color parameters and SST.

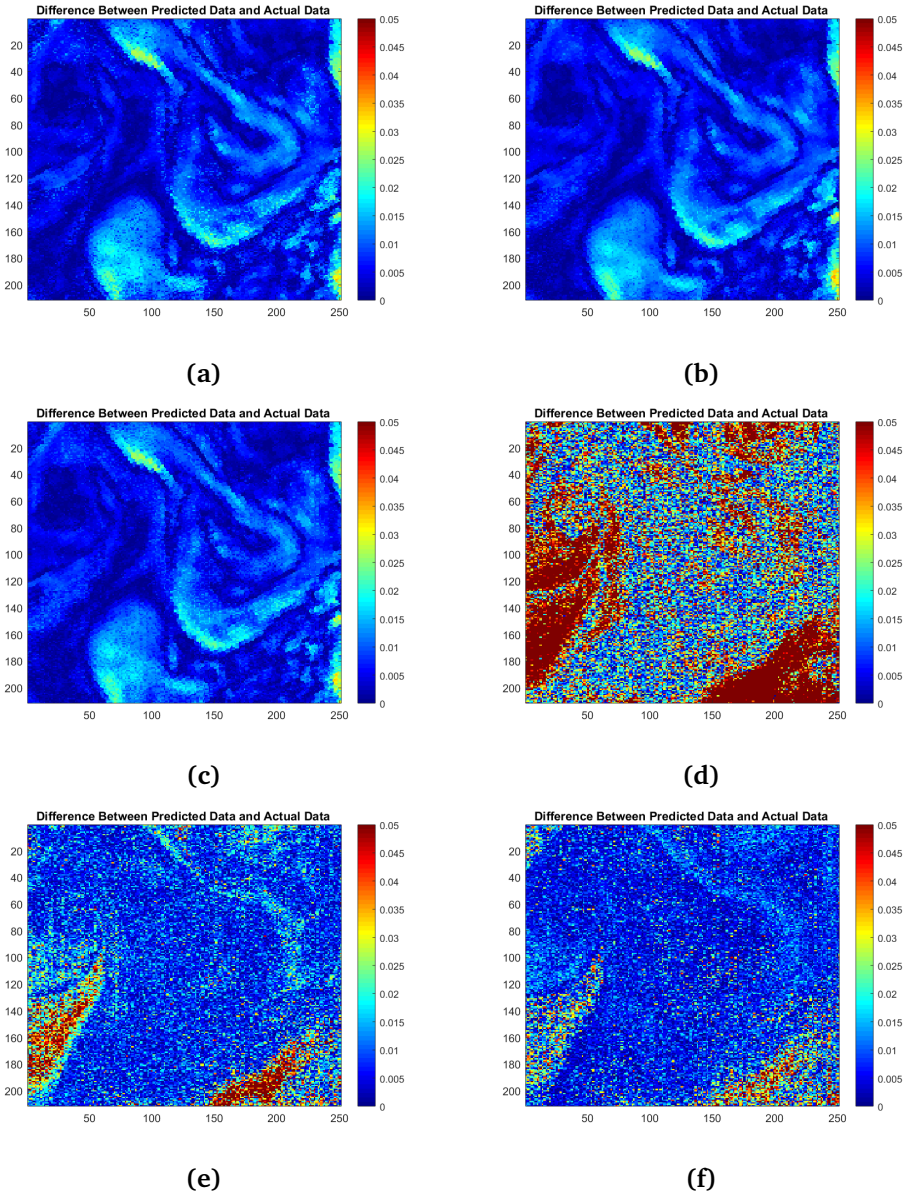

Figure 7.22: Difference images between predicted and actual data, for the SVM regression method, sub area A. (a) shows the difference image between the predicted SST data based on CHL data, and actual SST data. (b) shows the difference image between the predicted SST data based on TSM data, and the actual SST data. (c) shows the difference image between the predicted SST data based on CDOM data, and the actual SST data. (d) shows the difference image between the predicted CHL data based on SST data, and the actual CHL data. (e) shows the difference image between the predicted TSM data based on SST data, and the actual TSM data. (f) shows the difference image between the predicted CDOM data based on SST data, and the actual CDOM data.

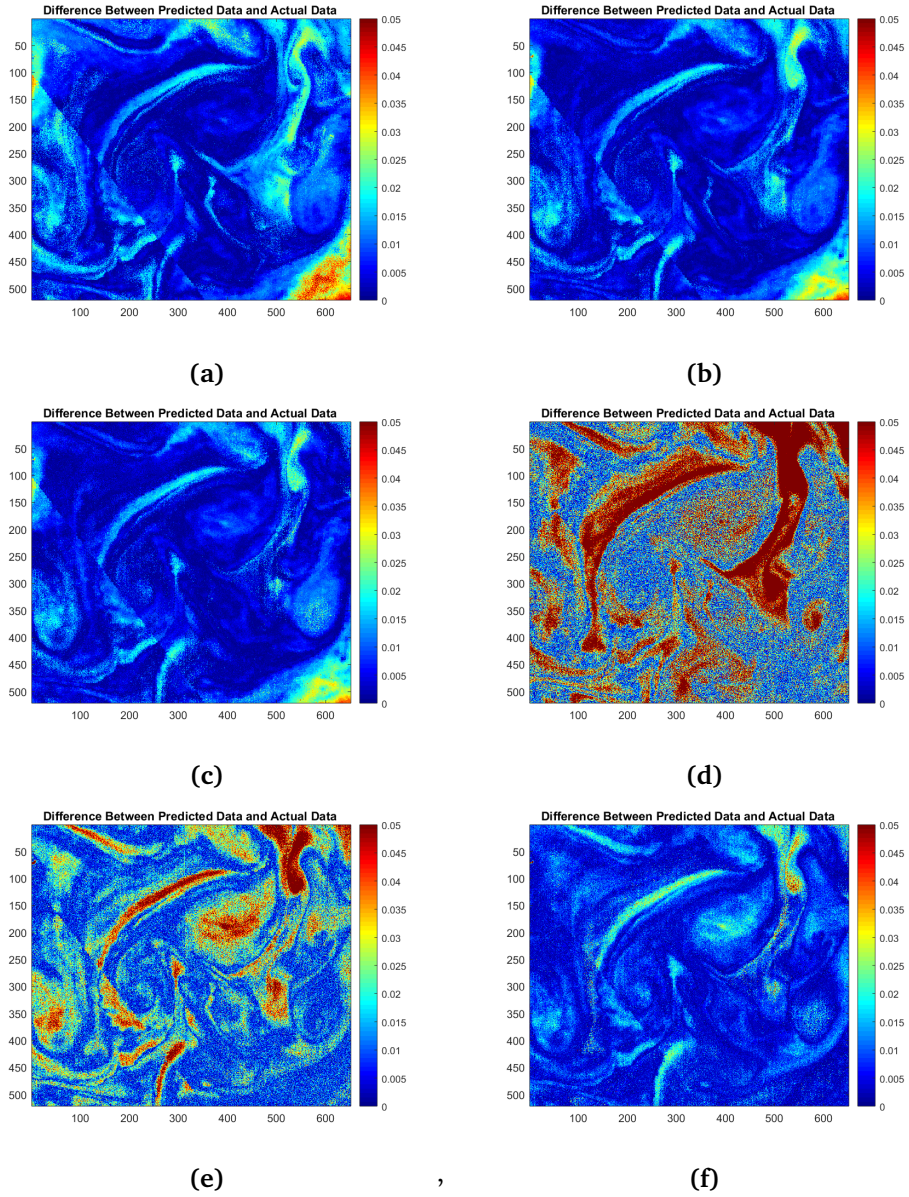

Figure 7.23: Difference images between predicted and actual data, for the SVM regression method, sub area B. (a) shows the difference image between the predicted SST data based on CHL data, and the actual SST data. (b) shows the difference image between the predicted SST data based on TSM data, and the actual SST data. (c) shows the difference image between the predicted SST data based on CDOM data, and the actual SST data. (d) shows the difference image between the predicted CHL data based on SST data, and the actual CHL data. (e) shows the difference image between the predicted TSM data based on SST data, and the actual TSM data. (f) shows the difference image between the predicted CDOM data based on SST data, and the actual CDOM data.

Table 7.7 shows the goodness of fit table for the SVM regression method between SST and ocean color parameters in sub area A. While Table 7.8 shows the goodness of fit table for the SVM regression method between SST and ocean color parameters in sub area B.

Figure	Bias	R^2	NRMSE
a	0.0011	0.1234	0.1456
b	8.0006e-04	0.0390	0.1443
c	3.2203e-04	0.0276	0.1436
d	0.0020	0.0465	0.0582
e	0.0031	0.0382	0.0996
f	0.0024	0.0362	0.0908

Table 7.7: Goodness of fit table for the SVM regression models for the combinations of SST and ocean color parameters, sub area A.

Figure	Bias	R^2	NRMSE
a	0.0012	0.2673	0.1114
b	0.0011	0.5275	0.0895
c	8.8049e-04	0.5701	0.0853
d	0.0048	0.2863	0.0582
e	2.6184e-04	0.5648	0.0338
f	0.0011	0.5835	0.0144

Table 7.8: Goodness of fit table for the SVM regression models for the combinations of SST and ocean color parameters, sub area B.

In Figure 7.22 and 7.23, we can see the resulting difference images for the SVM regression method from sub area A and B, respectively. At first sight, they look quite like the difference images from the liner regression method in Figure 7.20 and 7.21. If we compare the goodness of fit tables for both linear and SVM regression in sub area A for the combination of SST and ocean color parameters, in Table 7.5 and 7.7, we can see that the SVM regression model has slightly better goodness of fit compared to the linear regression models for the same combinations. We can also observe that for sub area A, R^2 are quite bad, meaning that SVM models are better than linear models, but still not good for

combinations of SST and ocean color parameters in sub area A. For sub area B, on the other hand, we can see that SVM regression models are slightly better than for linear regression models. Meaning that there exist an okay nonlinear relationship between SST and ocean color parameters in sub area B.

Method IV: Correlation Figure 7.24 for sub area A and Figure **??** for sub area B, shows the results of the correlation between different combinations of ocean color parameters and SST.

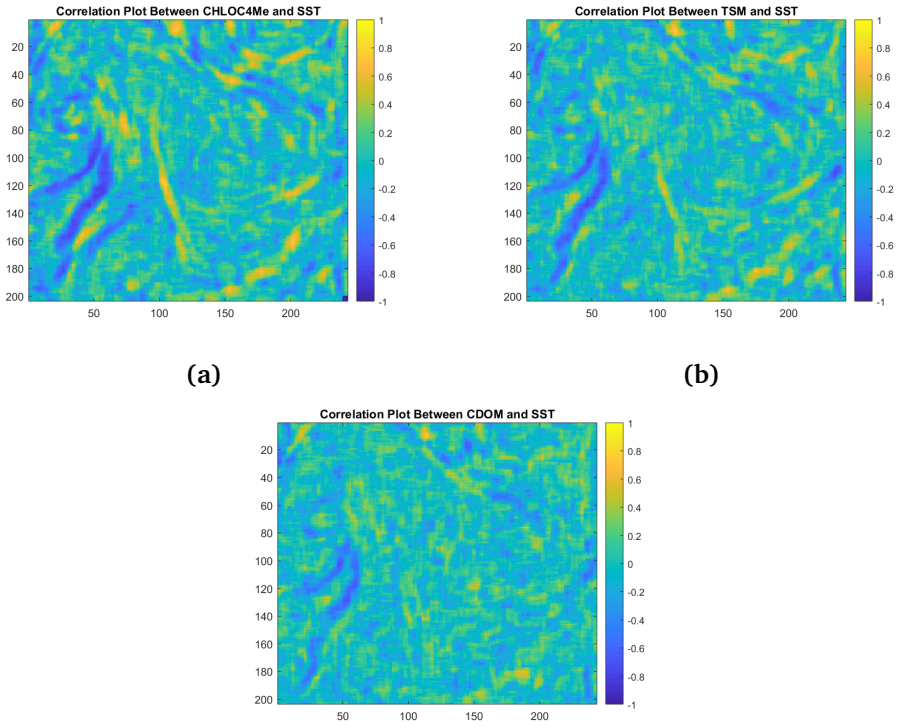

Figure 7.24: Result images from the correlation method, sub area A. (a) shows the correlation between CHL and SST. (b) shows the correlation between TSM and SST. (c) shows the correlation between CDOM and SST.

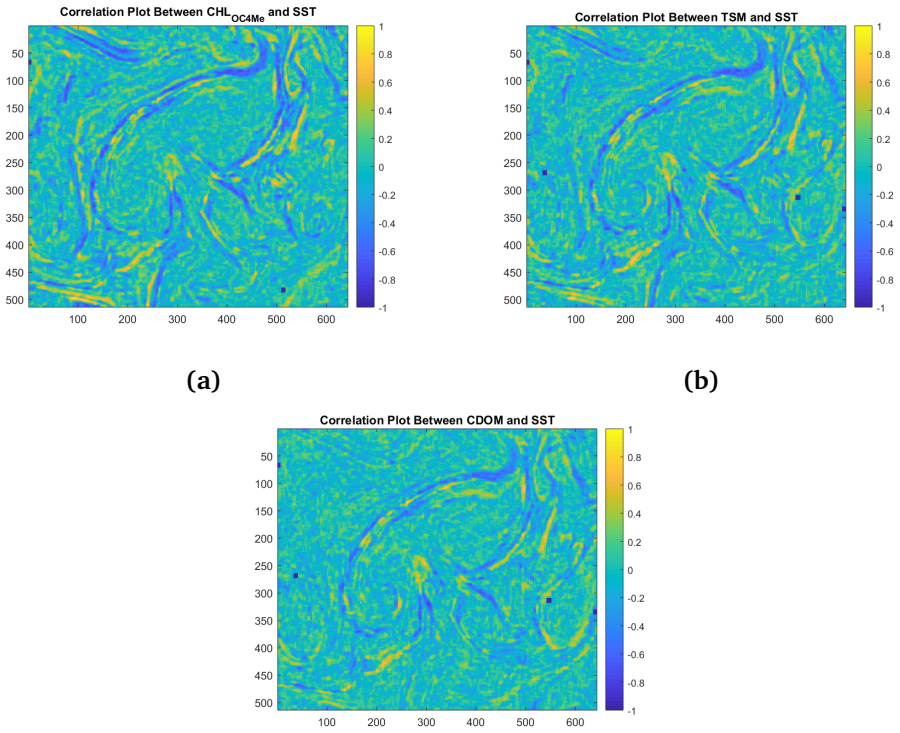

(a) **(b)**

(c)

Figure 7.25: Result images from the correlation method, sub area B. (a) shows the correlation between CHL and SST. (b) shows the correlation between TSM and SST. (c) shows the correlation between CDOM and SST.

In Figure 7.24 and 7.24 we can see the resulting correlation images from the correlation method, in sub area A and B. From both of these images we can see the edges of our whale shaped feature with negative correlation. In these images we can also see some areas with high concentrations, but not nearly as much as in the correlation images between ocean color parameters in Figure 7.16 and 7.25. In these images, the high correlation areas lays more in lines in the images. Meaning that in these lines, SST and ocean color parameters correlate well. There are not high correlation between SST and ocean color parameters, except a few areas.

7.2.1 Summary Case 2

Most of the statistical analysis methods gives the same trends, there are not very strong relations between SST and ocean color parameters for these images on these dates. Sub area B provides a better relationship between SST and ocean color parameters, compared to sub area A. Anyway, all methods give trends, and these trends show a slight sufficient relation between SST ans ocean color parameters, but not as strong as ocean color parameters alone.

7.3 Case 3

In this case, I have investigated the correlation between CHL from data set one and the SAR products from data set three. The CHL images from data set one can be seen in Figure 7.4 and 7.7, and the parameter images from data set three can be seen in Figure 7.6 and 7.9.

The correlation between CHL and SAR products can be seen in Figure 7.26 for sub area A and Figure 7.27

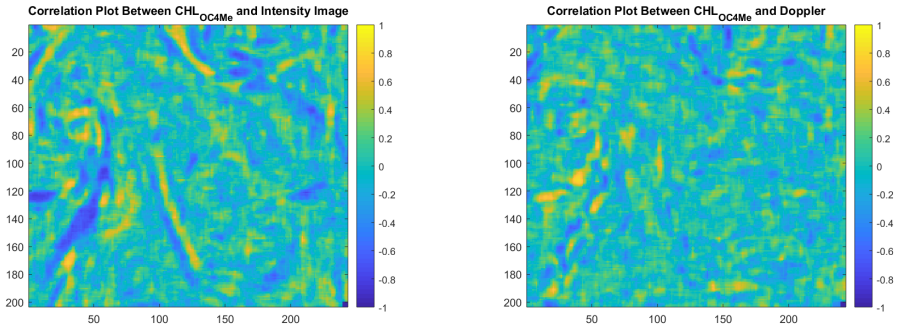

(a) **(b)**

Figure 7.26: Result images from the correlation between CHL and SAR products, sub area A

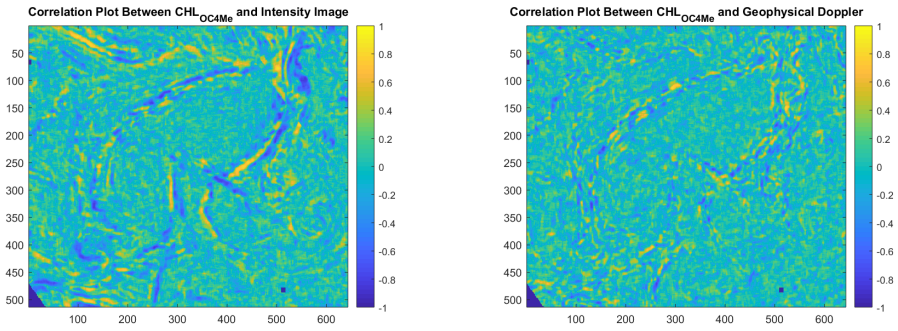

(a) **(b)**

Figure 7.27: Result images from the correlation between CHL and SAR products, sub area B

The results of the correlation between CHL and the SAR products can be seen

in Figure 7.26 and 7.27 for sub area A and B respectively. If we look at the result from the correlation from sub area A first, we can observe hints of the Eddie pattern, from the parameter images in Figure 7.4. We can also in (a), the correlation between CHL and Intensity image, see a very negative correlation in the edges of the Eddie path, and a stronger correlation where the Eddie path goes over in the "Eddie circle". We can also observe that most of the areas in (a) and (b) have a correlation between -0.2 and 0.2, meaning a low positive and a low negative correlation. It also looks like there are more areas with high correlation when we compare CHL and the intensity image, and not CHL and geophysical Doppler image. As mentioned before, intensity image are influenced by small scale waves and currents. So, maybe the patterns are more controlled by wind and waves, than the velocity of the surface.

7.4 Case 4

In this case, I have investigated the correlation between SST from data set two and the SAR products from data set three. The SST images from data set two can be seen in Figure 7.5 and 7.8, and the parameter images from data set three can be seen in Figure 7.6 and 7.9.

The correlation between SST and SAR products can be seen in Figure 7.28 for sub area A and Figure 7.29

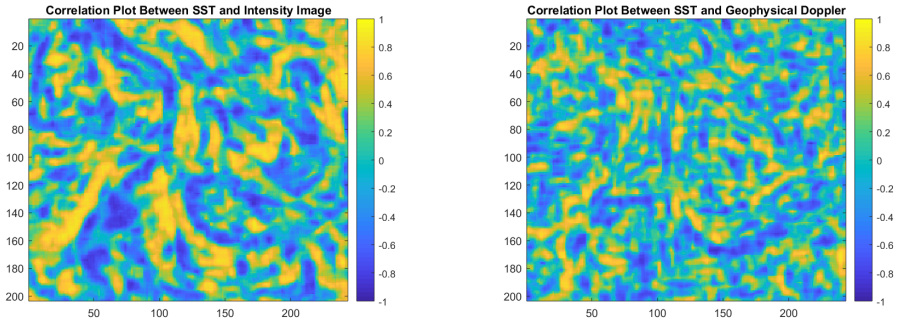

(a) **(b)**

Figure 7.28: Result images from the correlation between SST and SAR products, sub area A

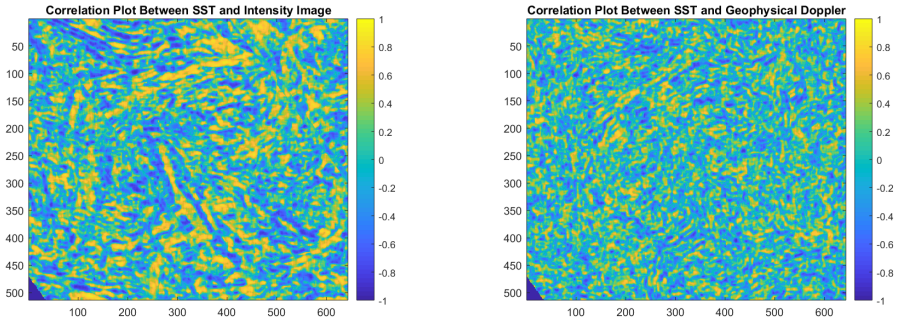

(a) **(b)**

Figure 7.29: Result images from the correlation between SST and SAR products, sub area B

The results of the correlation between SST and the SAR products can be seen

in Figure 7.28 and 7.29 for sub area A and B respectively. These images looks quite different compared to the correlation images of CHL and SAR products in Figure 7.26 and 7.27. In these images, Figure 7.28 and 7.29, we can see higher variations between high positive and high negative correlation. If we look at image (a) in both figures, between SST and intensity image, we can see many areas with high correlation, and several areas with a negative correlation. If we look at sub area A first, in Figure 7.28, n the left side, a bit below the middle, we can see a yellow strip in the intensity image. This area corresponds to the Eddie path and the light blue area in the same region in the SST image in Figure 7.5. The correlation image between SST and the geophysical Doppler image looks more chaotic. If you know where to look, you can think that it is possible to see some of the Eddie path in the geophysical Doppler, but it does not stick out at all. It is also possible to see a hint of that blue and red line that looks like a "hook" to the right of the centre in the SST image in Figure 7.5. Besides this, it looks very chaotic.

In Figure 7.29, we can see the correlation between SST and SAR products in sub area B. We can see hints of the whale pattern in the parameter images in Figure 7.7. The edge of the whale sticks out, some areas as positive correlation and some areas as negative correlation. Most of the areas in these three images have a correlation between -0.2 and 0.2, meaning low positive and low negative correlation. SST and the intensity image in (a) have more areas with high correlation, compared to (b). (b) looks more chaotic, but if you look closely where the top of the whale shape is in the parameter images, you can see hints of the top of the whale in all of the chaos, but only if you know where and what to look for. Besides that, you can not really say more.

7.4.1 Summary Case 3 and Case 4

In Case 3 we are investigating if we can see any correlation between the ocean color parameter CHL and the SAR products intensity image and geophysical Doppler image. The results from Figure 7.26 and 7.27 does not tell us that the relationship between the ocean color parameter CHL and SAR products are very good. We can observe some areas that correlates well both positive and negative, but most of the resulting images have a slightly positive or slightly

negative correlation, meaning that the images does not really correlate that much.

In Case 4 we are investigating if we can see any correlation between the SST and the SAR products intensity image and geophysical Doppler image. The results from Figure 7.28 and 7.29 does not tell us that the relationship between SST and SAR products are very good, but definitely better than for CHL and SAR products. We can observe many more areas with high positive and high negative correlation.

In both Case 3 and Case 4, we can observe that CHL and SST correlates better with the intensity images than the geophysical Doppler images. This can maybe indicate that the factors that have the biggest impact on intensity images, also have the biggest impact on CHL and SST images. Another interesting phenomenon that can bee seen in Figure 7.26, 7.27, 7.28 and 7.29, are that the patterns we have discussed through all of the results, can be seen here as well. But, you must know where to look and what to look for. Discussed in Chapter 3, intensity images for SAR satellites will be modified by wind stress and variations in ocean currents. Another ting mentioned in chapter 3, geophysical Doppler images are a measure of the velocity in the line of sight direction. This product can tell us about the velocity of the surface, and give an idea of the motion. Given this theory, one would think that the correlation between CHL, SST and the SAR products would be better than the results from Case 3 and Case 4.

There can be several possible sources of error for these results. First of all, there is a time difference between the different products. Ocean color data are taken before noon, and the SST data are taken a bit more than nine hours after. The SAR products are taken early morning or around dinner time in between four to five. The patterns can change between these times, and this can therefore have an effect on the results.

Another possible source of error, might be the different resolution on the images. I have chosen to interpolate the images to fit the ocean color parameters with the nearest neighbour method. Another method could have worked better, but it is hard to say. Instead of resampling the images to fit the ocean color data, it

could have been done the other way around. Such that the images would be on a 3.3-3.9km scale as the geophysical Doppler data. It is hard to say if this could affect the result, but it would have been interesting to check the other way around. The reason for the bad resolution in the intensity image and the geophysical Doppler image, is due to the deriving of the geophysical Doppler product.

A third possible source of error is that optical satellites sense in the top few meters of the ocean, while SAR satellites only sense the ocean surface. If the patterns we can see in the optical data are below the surface, we might not actually see them in the SAR images. From the result images for Case 3 and Case 4, one would think that some of the patterns we have seen in sub area B, is actually under water since it dos not come forward in the resulting images. But, it could also be the other errors causing these results.

It is also worth mentioning that this project has focused on using the free and open Sentinel data, found in the period between May and July 2018 for the study area. These results are of the data available from Sentinel-1 and Sentinel-3 between May and July 2018. The methods used in this thesis are also very manual, where interesting sub areas are found and investigated. A bigger project could have made a more semi-manual method and tested not only interesting areas, but all areas. In addition, testing more data will always make results better. But, at last, this thesis has focused on Sentinel images from May to July 2018, and the results will only be associated with these images.

7.4.2 Coastal waters

As we can see from satellite images of the study area, we observe high concentrations of chlorophyll, total suspended matter and colored dissolved organic material. These parameters can tell us about the biological productivity in the water or the water quality. These values are of interest for different purposes in the study area. SAR data from the study area can tell us about winds, waves and currents in the study area. Combining all of these data, can give a well overview of the coastal waters in the study area. As mentioned in the

introduction part, the period from May to July is known for having a strong upwelling along the coast of northern Norway. Offshelf transport of surface water, with compensating upwelling of nutrient rich water occurs this time period almost every year, and therefore it is interesting to look for any relation between combinations of parameters in this time period.

Unfortunately, it does not seem that we can find a well correlation between combinations of ocean color parameters, sea surface temperatures and SAR products in this study. The patterns that can be seen in the parameter images in Figure 7.4, 7.5, 7.7 and 7.8, may not be controlled only by ocean dynamics. Or they are, but this study are not able to prove it. However, it would have been interesting to make some changes to this study to see if the results get any better. For example changing the data with interpolation to fit the SAR products for example. It is not for sure that this will change the results, but it would have been interesting to investigate. Using other images from other satellites with less time difference could also have been very interesting to investigate.

8

Conclusion and Future Work

This thesis has examined four different test cases, to investigate the relationship and correlation between different combinations of parameters. Case 1 investigated the relationship between ocean color parameters(CHL, TSM and CDOM), and Case 2 investigated the relationship between SST and ocean color parameters, both cases using four different statistical analysis methods. Case 3 investigated the correlation between the ocean color parameter CHL and SAR products, while Case 4 investigated the correlation between SST and SAR products.

Based on the results presented in the previous chapter, the following findings and observations were made:

- Case 1: the four statistical analysis approaches all found a good relation between ocean color parameters.

- Case 2: the four statistical analysis approaches did not find a good rela-

tionship between SST and ocean color parameters, but there are some sufficient relations. CDOM seems to be the ocean color parameter that has the best relationship with SST.

- Case 3: the correlation method did not find a strong correlation between CHL and SAR products(intensity image and geophysical Doppler image).

- Case 4: the correlation method did not find a strong correlation between CHL and SAR products(intensity image and geophysical Doppler image), but definitely more correlation between SST and SAR compared to CHL and SAR.

8.1 Conclusion

The aim of this thesis was to investigate the combinations of remote sensing imaging sensors for mapping and monitoring of coastal waters, using ocean color and sea surface temperature data from the OLCI and SLSTR sensors on the optical satellite Sentinel-3, and intensity image and geophysical Doppler images from the C-SAR sensor on the SAR satellite Sentinel-1. From these different sensors, we get various products that can be used to investigate coastal waters. The main objective was to investigate the patterns in the ocean that can be seen in the ocean color images, and to check if these patterns could be seen in SAR products.

The two main research questions presented in the introduction were:

1. *Is it possible to find a relationship between ocean color parameters and sea surface temperature images?*

2. *Are there any correlations between the patterns we can observe from ocean color parameters and sea surface temperature from an optical satellite, and intensity images or geophysical Doppler product images from a SAR satellite?*

To answer the first research question, I would have to say that Case 1 showed

a good relationship between combinations of ocean color parameters. Case 2, on the other hand, showed not a very good relationship between SST and ocean color parameters, but an okay relationship. CDOM is the ocean color parameter that has the best relationship with SST.

To answer the second research question, I would have to say that the correlation method that was applied on different combinations on CHL or SST parameters and SAR products, did not give that good results as I would have thought. From the results in Case 3 and Case 4, we could still see hints of the patterns from the ocean color and SST parameters in the parameter images, but they did not exactly stick out that much. You would have to know where and what to look for to see some of the features. We could also see that the correlation with CHL or SST and the intensity image, gave most areas with stronger positive and negative correlation, compared to the correlation with CHL or SST and the geophysical Doppler images.

This study could not find a direct correlation between ocean color and sea surface temperature images from Sentinel-3, against SAR products such as intensity images and geophysical Doppler images from the satellites Sentinel-1. The patterns that can be seen in the ocean color and sea surface temperature images, may not only be controlled by ocean dynamics. Or they are, it is just that this study could not prove it. It is difficult to know for sure, but some limitations could affect this result.

8.1.1 Limitations

Several limitations to this study need to be acknowledged. Three possible sources of error are:

- The time difference between the data from different sensors. The ocean is a complex system in motion, thus the parameters in the ocean can move in between the sensing from the sensors on the satellites. Using satellite images from satellites with less or no time difference would probably give a more correct result.

- The resolution differences between data from different sensors. In this study, the satellite data was interpolated to fit the ocean color data, meaning an upsampling of the other products. If the images had been interpolated to fit the intensity image and the geophysical Doppler image with the lowest resolution, this could have had a positive effect on the results.

- Optical satellites sense a few meters below the surface, while the SAR satellites only sense the top of the surface. Meaning, that if the patterns in the ocean are below the surface, the SAR satellite would not be able to sense it.

8.2 Future Work

There are several possible improvements that might give better results or show relationships between different combinations of products better. Firstly, it would be interesting to test this study on images much closer in time. This can be very hard in the "World of Remote Sensing" that we live in, given that not many satellites, if there are any at all, sense the same area almost at the same time. In this thesis, the free and open Copernicus satellites Sentinel-1 and Sentinel-3 have been used, but maybe a couple of other satellites or airborne sensors can provide satellite data closer in time.

Another thing that would be interesting to check, are the results if the interpolation had been the opposite way, where the interpolation resampling had been done to fit the SAR products for example. This project has only tested some data. With more data, let us say 1000 dates, the results will be stronger. This thesis have also been done with a very manual method, so making a more semi-manual method would make this study more efficient.

Last, there are very little information out there about coastal dynamics in northern Norway. This is something that will be needed in regards to how we in the future can understand the success of the management of marine resources.

Both the fish and this billion industry of Norway deserves better analysis of the livelihood and the sustainability of these unique areas. More information and a better understanding of these coastal areas will help us, such that we in the future can understand the success of the management of marine resources in a sustainable manner.

Bibliography

[Antoine, 2010] Antoine, D. (2010). Olci level-2 - ocean colour turbid waters. *Algorithm Theoretical Basis Document*, (2.2):1–31.

[Bakun, 1990] Bakun, A. (1990). Global climate change and intensification of coastal ocean upwelling. *Science*, 247(4939):198–201.

[Blix et al., 2018] Blix, K., Pálffy, K., R Tóth, V., and Eltoft, T. (2018). Remote sensing of water quality parameters over lake balaton by using sentinel-3 olci. *Water*, 10(10):1428.

[Blondeau-Patissier et al., 2014] Blondeau-Patissier, D., Gower, J. F., Dekker, A. G., Phinn, S. R., and Brando, V. E. (2014). A review of ocean color remote sensing methods and statistical techniques for the detection, mapping and analysis of phytoplankton blooms in coastal and open oceans. *Progress in oceanography*, 123:123–144.

[Caccioppoli, 2014] Caccioppoli, B. (2014). Strengthening Winds and Upwelling in a Changing Climate. `https://oceanbites.org/strengthening-winds-and-upwelling-in-a-changing-climate/`. [Online; accessed 2019.03.01].

[Callao and Larrechi, 2015] Callao, M. P. and Larrechi, M. S. (2015). Simultaneous determination of organic dyes using second-order data. In *Data Handling in Science and Technology*, volume 29, pages 399–426. Elsevier.

[Callot, 1991] Callot, H. (1991). Geochemistry of chlorophylls. In *Chlorophylls*, pages 339–364. CRC Press London.

[Campbell, 2011] Campbell, J. (2011). *Introduction to remote sensing*. Guilford Press, New York, N.Y.

[Carder et al., 2002] Carder, K., Chen, F., Cannizzaro, J., and Campbell, J. (2002). Performance of modis semi-analytic ocean color algorithms: chlorophyll a, absorption coefficeints, and absorbed radiation by phytoplankton. In *34th COSPAR Scientific Assembly*, volume 34.

[Carder et al., 1999] Carder, K., Chen, F., Lee, Z., Hawes, S., and Kamykowski, D. (1999). Semi-analytic modis algorithms for chlorophyll a and absorption with bio-optical domains based on nitrate-depletion temperatures. *J. Geophys. Res*, 104(C3):5403–5421.

[Climatestotravel.com, nd] Climatestotravel.com (n.d-). Climate - Norway. `https://www.climatestotravel.com/climate/norway`. [Online; accessed 2019.03.01].

[Cullen, 1982] Cullen, J. J. (1982). The deep chlorophyll maximum: comparing vertical profiles of chlorophyll a. *Canadian Journal of Fisheries and Aquatic Sciences*, 39(5):791–803.

[Doerffer, 2010] Doerffer, R. (2010). Olci level-2 - ocean colour turbid water. *Algorithm Theoretical Basis Document*, (2.0):1–50.

[Elachi and Van Zyl, 2006] Elachi, C. and Van Zyl, J. J. (2006). *Introduction to the physics and techniques of remote sensing*, volume 28. John Wiley & Sons.

[Engen et al., 2014] Engen, G., Johnsen, H., and Larsen, Y. (2014). Sentinel-1 geophysical doppler product-performance and application. In *EUSAR 2014; 10th European Conference on Synthetic Aperture Radar; Proceedings of*, pages 1–4. VDE.

[ESA, nd a] ESA (n.d-a). CDM Absorption Coefficient. `https://sentinel.esa.int/web/sentinel/technical-guides/sentinel-3-olci/level-2/cdm-absorption-coefficient`. [Online; accessed 2019.03.01].

[ESA, nd b] ESA (n.d-b). IMT Neural Net. https://sentinel.esa.int/web/sentinel/technical-guides/sentinel-3-olci/level-2/imt-neural-net. [Online; accessed 2019.03.01].

[ESA, nd c] ESA (n.d-c). OC4Me Chlorophyll. https://sentinel.esa.int/web/sentinel/technical-guides/sentinel-3-olci/level-2/oc4me-chlorophyll. [Online; accessed 2019.03.01].

[ESA, nd d] ESA (n.d-d). Oceans and Ice. https://www.esa.int/Our_Activities/Observing_the_Earth/Copernicus/Sentinel-1/Oceans_and_ice. [Online; accessed 2019.03.01].

[ESA, nd e] ESA (n.d-e). OLCI Level 2 Algorithm Theoretical Basis Document - Ocean Colour Products in Case 1 waters. https://sentinel.esa.int/documents/247904/349589/OLCI_L2_ATBD_Ocean_Colour_Products_Case-1_Waters.pdf. [Online; accessed 2019.03.01].

[ESA, nd f] ESA (n.d-f). OLCI Level 2 Algorithm Theoretical Basis Document - Ocean Colour Turbid Water. https://sentinel.esa.int/documents/247904/349589/OLCI_L2_ATBD_Ocean_Colour_Turbid_Water.pdf. [Online; accessed 2019.03.01].

[ESA, nd g] ESA (n.d-g). Radiometric Resolution. https://sentinel.esa.int/web/sentinel/user-guides/sentinel-3-slstr/resolutions/radiometric. [Online; accessed 2019.03.01].

[ESA, nd h] ESA (n.d-h). Radiometric Resolution - 21 bands in VIS/SWIR. https://sentinel.esa.int/web/sentinel/user-guides/sentinel-3-olci/resolutions/radiometric. [Online; accessed 2019.03.01].

[ESA, nd i] ESA (n.d-i). Sentinel-1. https://earth.esa.int/web/guest/missions/esa-operational-eo-missions/sentinel-1. [Online; accessed 2019.03.01].

[ESA, nd j] ESA (n.d-j). Sentinel-3. https://earth.esa.int/web/guest/missions/esa-eo-missions/sentinel-3. [Online; accessed 2019.03.01].

[ESA, nd k] ESA (n.d-k). Sentinel-3 OLCI Technical Guide. https://sentinel.esa.int/web/sentinel/technical-guides/sentinel-3-olci. [Online; accessed 2019.03.01].

[ESA, nd l] ESA (n.d-l). Sentinel-3 SLSTR Technical Guide. https://sentinel.esa.int/web/sentinel/technical-guides/sentinel-3-slstr. [Online; accessed 2019.03.01].

[ESA, nd m] ESA (n.d-m). SNAP. http://step.esa.int/main/toolboxes/snap/. [Online; accessed 2019.03.01].

[ESA, nd n] ESA (n.d-n). Total Suspended Matter Concentration. https://sentinel.esa.int/web/sentinel/technical-guides/sentinel-3-olci/level-2/total-suspended-matter-concentration. [Online; accessed 2019.03.01].

[Franceschetti and Lanari, 1999] Franceschetti, G. and Lanari, R. (1999). *Synthetic aperture radar processing*. CRC Press, Boca Raton.

[Gade and Barale, 2008] Gade, M. and Barale, V. (2008). Multi-sensor remote sensing of coastal discharge plumes: A mediterranean test site. In *Remote Sensing of the European Seas*, pages 475–486. Springer.

[Gu and Zhang, 2011] Gu, Y. and Zhang, W. (2011). Qr code recognition based on image processing. In *International Conference on Information Science and Technology*, pages 733–736. IEEE.

[Havforskningsinstituttet, 2011] Havforskningsinstituttet (2011). Strømforhold. http://www.imr.no/temasider/havomrader_og_okosystem/lofoten_vesteralen/stromforhold/nb-no. [Online; accessed 2019.03.01].

[Henderson, 1998] Henderson, F. (1998). *Principles and applications of imaging radar*. J. Wiley, New York.

[Hoepffner and Sathyendranath, 1993] Hoepffner, N. and Sathyendranath, S. (1993). Determination of the major groups of phytoplankton pigments from the absorption spectra of total particulate matter. *Journal of Geophysical*

Research: Oceans, 98(C12):22789–22803.

[Huisman et al., 2006] Huisman, J., Thi, N. N. P., Karl, D. M., and Sommeijer, B. (2006). Reduced mixing generates oscillations and chaos in the oceanic deep chlorophyll maximum. *Nature*, 439(7074):322.

[Imawaki et al., 2013] Imawaki, S., Bower, A. S., Beal, L., and Qiu, B. (2013). Western boundary currents. In *International Geophysics*, volume 103, pages 305–338. Elsevier.

[Joseph, 2014] Joseph, A. (2014). Chapter 1 - oceanic currents and their implications. In Joseph, A., editor, *Measuring Ocean Currents*, pages 1 – 49. Elsevier, Boston.

[Kämpf and Chapman, 2016] Kämpf, J. and Chapman, P. (2016). Upwelling systems of the world.

[Lasker, 1981] Lasker, R. (1981). The role of a stable ocean in larval fish survival and subsequent recruitment. *Marine fish larvae: morphology, ecology and relation to fisheries*, pages 81–87.

[Lin et al., 2002] Lin, I.-I., Wen, L.-S., Liu, K.-K., Tsai, W.-T., and Liu, A. K. (2002). Evidence and quantification of the correlation between radar backscatter and ocean colour supported by simultaneously acquired in situ sea truth. *Geophysical Research Letters*, 29(10):102–1.

[Lovecchio et al., 2018] Lovecchio, E., Gruber, N., and Münnich, M. (2018). Mesoscale contribution to the long-range offshore transport of organic carbon from the canary upwelling system to the open north atlantic. *Biogeosciences*, 15(16):5061–5091.

[Maritorena et al., 2002] Maritorena, S., Siegel, D. A., and Peterson, A. R. (2002). Optimization of a semianalytical ocean color model for global-scale applications. *Applied optics*, 41(15):2705–2714.

[Martin, 2014] Martin, S. (2014). *An introduction to ocean remote sensing*. Cambridge University Press.

[MathWorks, nd a] MathWorks (n.d-a). corr2. https://se.mathworks.com/help/images/ref/corr2.html. [Online; accessed 2019.03.01].

[MathWorks, nd b] MathWorks (n.d-b). Linear Regression. https://se.mathworks.com/help/matlab/data_analysis/linear-regression.html. [Online; accessed 2019.03.01].

[MathWorks, nd c] MathWorks (n.d-c). Understanding Support Vector Machine Regression. https://se.mathworks.com/help/stats/understanding-support-vector-machine-regression.html. [Online; accessed 2019.03.01].

[Matthews, 2014] Matthews, J. (2014). *Encyclopedia of environmental change*. SAGE Publications, London Thousand Oaks, California.

[McClain, 2009] McClain, C. R. (2009). A decade of satellite ocean color observations. *Annual Review of Marine Science*, 1:19–42.

[Mobley, 1994] Mobley, C. D. (1994). *Light and water: radiative transfer in natural waters*. Academic press.

[Mobley, 1995] Mobley, C. D. (1995). The optical properties of water. *Handbook of optics*, 1:43–41.

[Mobley, 1998] Mobley, C. D. (1998). Hydrolight 4.0 users guide. Technical report, SEQUOIA SCIENTIFIC INC MERCER ISLAND WA.

[Morel and Antoine, 2011] Morel, A. and Antoine, D. (2011). ATBD 2.9 — PIGMENT INDEX RETRIEVAL IN CASE 1 WATERS. https://earth.esa.int/documents/700255/2042855/MERIS_ATBD_2.9_v4.3+-+2011.pdf. [Online; accessed 2019.03.01].

[Morel et al., 2002] Morel, A., Antoine, D., and Gentili, B. (2002). Bidirectional reflectance of oceanic waters: accounting for raman emission and varying particle scattering phase function. *Applied Optics*, 41(30):6289–6306.

[Morel and Gentili, 1996] Morel, A. and Gentili, B. (1996). Diffuse reflectance of oceanic waters. iii. implication of bidirectionality for the remote-sensing

problem. *Applied Optics*, 35(24):4850–4862.

[Morel et al., 2007] Morel, A., Gentili, B., Claustre, H., Babin, M., Bricaud, A., Ras, J., and Tieche, F. (2007). Optical properties of the "clearest" natural waters. *Limnology and oceanography*, 52(1):217–229.

[Morel and Prieur, 1977] Morel, A. and Prieur, L. (1977). Analysis of variations in ocean color. *Limnology and oceanography*, 22(4):709–722.

[Myhre, 2013] Myhre, F. (2013). Lofoten, vesterålen and senja. permanent ban on oil and gas drilling. fact sheet 2013.

[Naranjo, nd] Naranjo, L. (n.d-). Microbes in the murk. `https://earthdata.nasa.gov/user-resources/sensing-our-planet/microbes-in-the-murk`. [Online; accessed 2019.03.01].

[Naturvernforbundet, nd] Naturvernforbundet (n.d-). Derfor må olja bli liggende. `https://naturvernforbundet.no/lofoten-vesteralen-og-senja/category1467.html`. [Online; accessed 2019.03.01].

[NOAA, 2017] NOAA (2017). Ekman Spiral. `https://oceanservice.noaa.gov/education/kits/currents/media/supp_cur05e.html`. [Online; accessed 2019.03.01].

[NOAA, nd a] NOAA (n.d-a). What is a gyre? `https://oceanservice.noaa.gov/facts/gyre.html`. [Online; accessed 2019.03.01].

[NOAA, nd b] NOAA (n.d-b). What is upwelling? `https://oceanservice.noaa.gov/facts/upwelling.html`. [Online; accessed 2019.03.01].

[Park, 2017] Park, C. (2017). *A dictionary of environment and conservation*. Oxford University Press, Oxford.

[Randelhoff and Sundfjord, 2018] Randelhoff, A. and Sundfjord, A. (2018). Short commentary on marine productivity at arctic shelf breaks: upwelling, advection and vertical mixing. *Ocean Science*, 14(2):293.

[Regjeringen.no, 2002] Regjeringen.no (2002). Report No. 12 to the Storting (2001-2002). https://www.regjeringen.no/en/dokumenter/report-no.-12-to-the-storting-2001-2002/id195387/sec3. [Online; accessed 2019.03.01].

[Roesler et al., 1989] Roesler, C. S., Perry, M. J., and Carder, K. L. (1989). Modeling in situ phytoplankton absorption from total absorption spectra in productive inland marine waters. *Limnology and Oceanography*, 34(8):1510–1523.

[Scott and Hansen, 2016] Scott, M. and Hansen, K. (2016). Sea Ice. https://earthobservatory.nasa.gov/features/SeaIce. [Online; accessed 2019.03.01].

[Siegel et al., 2012] Siegel, D., Antoine, D., Behrenfeld, M., d'Andon, O., Fields, E., Franz, B., Goryl, P., Maritorena, S., McClain, C., Wang, M., et al. (2012). State of climate 2011-global ocean phytoplankton.

[Slagstad et al., 1999] Slagstad, D., Tande, K. S., and Wassman, P. (1999). Modelled carbon fluxes as validated by field dta on the north norwegian shelf during the productive period in 1994. *Sarsia*, 84(3-4):303–317.

[Song et al., 2012] Song, K., Li, L., Wang, Z., Liu, D., Zhang, B., Xu, J., Du, J., Li, L., Li, S., and Wang, Y. (2012). Retrieval of total suspended matter (tsm) and chlorophyll-a (chl-a) concentration from remote-sensing data for drinking water resources. *Environmental Monitoring and Assessment*, 184(3):1449–1470.

[Stahl and Sies, 2003] Stahl, W. and Sies, H. (2003). Antioxidant activity of carotenoids. *Molecular aspects of medicine*, 24(6):345–351.

[Tilstone et al., 2017] Tilstone, G., Mallor-Hoya, S., Gohin, F., Couto, A. B., Sá, C., Goela, P., Cristina, S., Airs, R., Icely, J., Zühlke, M., et al. (2017). Which ocean colour algorithm for meris in north west european waters? *Remote Sensing of Environment*, 189:132–151.

[Warren, 1976] Warren, B. A. (1976). Structure of deep western boundary

currents. In *Deep Sea Research and Oceanographic Abstracts*, volume 23, pages 129–142. Elsevier.

[Wright, 1921] Wright, S. (1921). Correlation and causation. *Journal of agricultural research*, 20(7):557–585.

[Wright et al., 2005] Wright, S., Jeffrey, S., and Mantoura, R. (2005). *Phytoplankton pigments in oceanography: guidelines to modern methods*. Unesco Pub.

[Zaneveld et al., 2006] Zaneveld, R., Barnard, A., and Lee, Z. (2006). Why are inherent optical properties needed in ocean-colour remote sensing. *Remote Sensing of Inherent Optical Properties: Fundamentals, Tests of Algorithms and Applications*, 5:3–11.